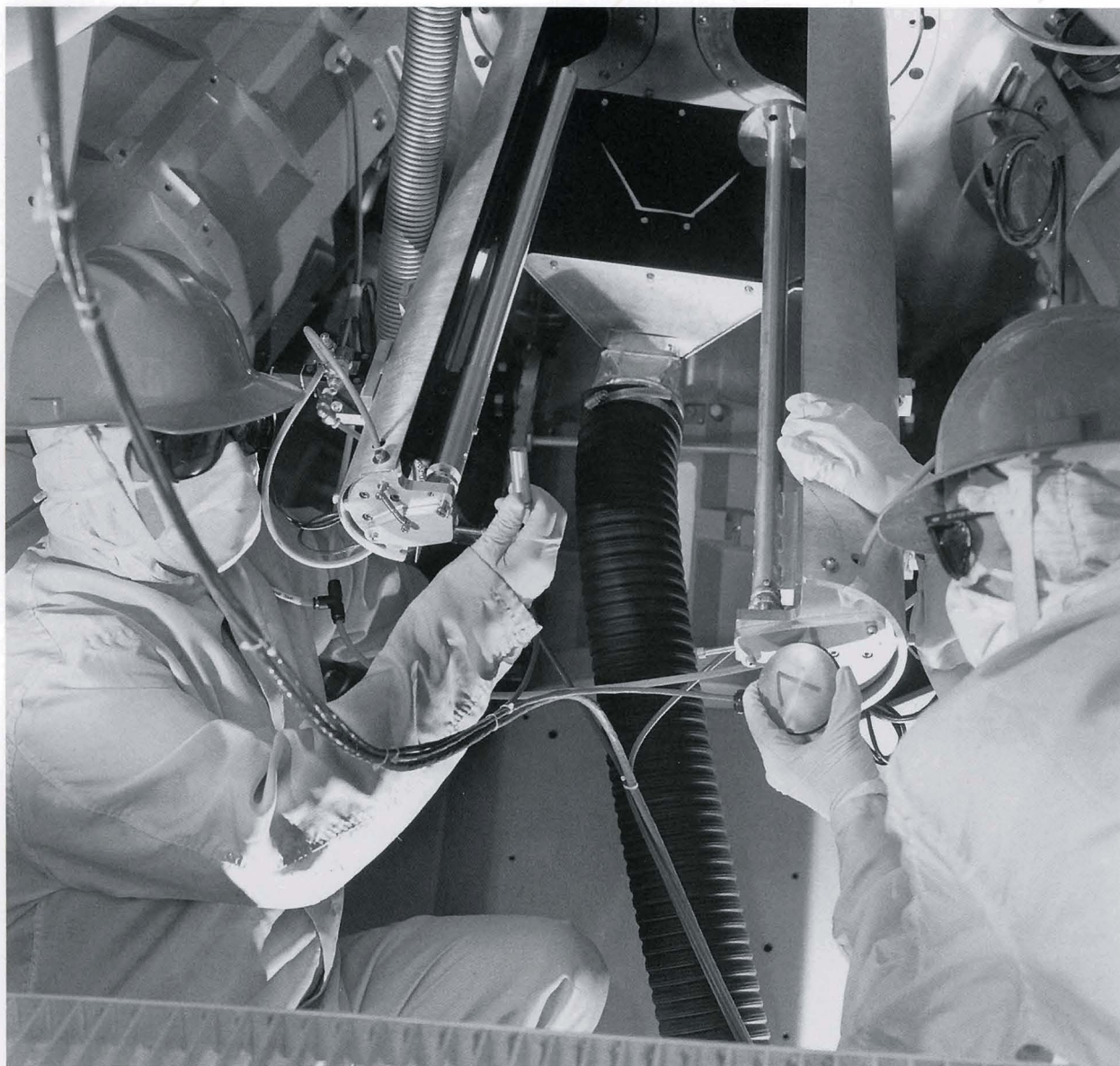# LLE Review

Quarterly Report

UR
LLE

About the Cover:

Kevin Kearney, research engineer (left), and Cherie Miskey, a physics undergraduate co-op student from the Rochester Institute of Technology (right), are preparing to load a cylinder of indium and a disk of copper, respectively, into the OMEGA target chamber through the ports in the top center. These samples are held on a rapid extractor mechanism, which withdraws them after a shot and drops them down the black tube (center) to a diagnostic room below, where their activation is measured to determine the neutron yield. Experiments producing record high neutron yields are reported in this issue.

LLE Review

UR
LLE

Quarterly Report

Contents

In Brief

This volume of the LLE Review, covering the period July–September 1995, includes a description of the first target experiments performed on the upgraded OMEGA laser system. These experiments, carried out to activate and test several diagnostics systems, have demonstrated successful functioning of the overall experimental system and have produced high neutron yields and high core temperatures. Other articles in this volume describe the diagnosis of core conditions using krypton line spectroscopy, a mix model for *LILAC* that can be applied to study the deceleration instability at the pusher-core interface, a simulated-annealing algorithm for improved phase-plate design, a simple method for characterizing the thickness and uniformity of transparent laser-fusion targets, and femtosecond pump-probe experiments on semi-conducting YBCO.

Highlights of the research presented in this issue are as follows:

- A series of initial target implosion experiments has been carried out with the upgraded OMEGA laser system. Record neutron yields of 10^{14} (corresponding to 1% of scientific breakeven) have been achieved, and high fuel electron and ion temperatures (4 and 13 keV, respectively) have been diagnosed.

- Improved calculations of krypton Stark profiles have been used to refine the diagnostic technique of doping the fuel with small amounts of krypton. Using different doping levels, krypton lines can be used to measure the electron and ion temperatures and the density-radius product of the compressed core.

- A new mix model has been added to the one-dimensional hydrocode *LILAC*. The model describes the evolution of the mixed region near the unstable fuel-pusher interface and is fully incorporated into the hydrodynamics simulation. Calculations using the model support the feasibility of diagnosing mix using thin x-ray-emitting additive layers placed in the pusher near the unstable interface.

- A new simulated-annealing algorithm has been used to design phase plates that generate the desired far-field profile while minimizing wide-angle scattering outside this profile. The flexibility of this algorithm should enable a wide range of phase plates to be designed for a variety of applications.

- A new technique is presented for the characterization of transparent laser-fusion targets. When irradiated with narrow-bandwidth, spatially incoherent light and viewed in a microscope, these shells display self-interference patterns that provide for a rapid assessment of wall thickness and uniformity.

- Femtosecond pump-probe experiments have been carried out to study the electronic structure of semiconducting YBCO. The bandwidth of the O-$2p$ band has been measured to be approximately 1.9 eV.

R. Stephen Craxton
Editor

Initial Target Experiments on the Upgraded OMEGA Laser System

A major program to demonstrate the feasibility of direct-drive laser fusion is underway at LLE. The overall goal of this program is to develop an understanding of target physics at the 30-kJ level that will allow the performance of direct-drive capsules designed for use with the National Ignition Facility (NIF) at the 1- to 2-MJ level to be predicted with confidence. The majority of the experiments that will contribute to this goal will be performed with the 60 UV (351-nm) beams of the recently upgraded, 30-kJ OMEGA laser system. The key physics issues that will be examined, both experimentally and theoretically, include irradiation uniformity, laser energy coupling and transport, laser-plasma interaction physics, hydrodynamic stability, and hot-spot and main-fuel-layer physics.

In this article we summarize initial target experiments performed with the upgraded OMEGA laser system.[1] Targets consisted mainly of glass microballoons (GMB's) having high initial aspect ratios ($R/\Delta R$, where R is the target radius and ΔR is the shell thickness) of ~150 to 300, filled with either pure deuterium or an equimolar mixture of deuterium and tritium at pressures ranging from 5 to 20 atm. These low-mass shells were accelerated to high implosion velocities. The compressed fuel was predicted to have a high electron temperature (up to 6 keV) and a density in the range of 0.2 to 2 g/cm^3. Diagnosis of target performance during the acceleration phase of the implosion was obtained from time- and space-resolved measurements of the x-ray emission from the laser-heated glass shells. Overall target performance was diagnosed by nuclear and particle instrumentation, from which estimates of the total thermonuclear yield and the fuel ion temperature were obtained. Neutron yields have been measured to be as high as 10^{14} (DT) and 1.1×10^{12} (DD), and ion temperatures up to 13 keV have been inferred from a neutron time-of-flight detector. High fuel electron temperatures of 3 to 4 keV have been inferred from spectroscopic measurements.

The main objective of these initial experiments was the activation of several key diagnostic systems. An x-ray framing camera and a Kirkpatrick-Baez (KB) microscope were used to image the x-ray emission during the implosions. Copper and indium neutron activation counters were used to determine DT and DD neutron yields, and scintillator-photomultipliers were used to measure the neutron time-of-flight. Finally, a crystal spectrometer was fielded to measure the electron temperature from the continuum slope of the x-ray spectrum and from krypton K-shell spectroscopy.

X-Ray Imaging

1. X-Ray Framing Camera

A series of experimental shots were devoted to the initial activation of one of the x-ray framing cameras. The camera is based on the high-speed gating of a 0.25-mm-thick microchannel plate with a channel-pore aspect ratio (length:diameter) of 40:1. The design and testing of the prototype for this camera are described in Ref. 2. The temporal resolution of the camera over a range of operating parameters was measured off-line using a short-pulse (300-fs) frequency-quintupled glass laser system. For the GMB's in this experimental series the camera was operated with an expected temporal resolution (gating time) of 35 to 40 ps.

Figure 64.1 shows a series of images recorded from shot 5067, sensitive to x rays in the spectral range above 3 keV. The target was a 20-atm DD-filled glass microballoon with an initial wall thickness of 2.3 μm and a diameter of 845 μm. The magnification was 6× and the calculated spatial resolution was ~10 μm in the target plane. The time delay between strips is 250 ps, and the delay between images on a given strip is 50 ps. The fogging around the images in the third and fourth strips is caused by high-energy x rays produced during the implosion and transmitted through the 50-μm Ta pinhole substrate. The vignetting seen in the four corner images is caused by a circular aperture in the pinhole mount. The x-ray emission comes primarily from overdense glass plasma with an electron temperature $\gtrsim$800 eV. During much of the implosion, before the glass has expanded significantly beyond its initial thickness, the location of the peak x-ray emission thus provides a good indication of the shell's location.
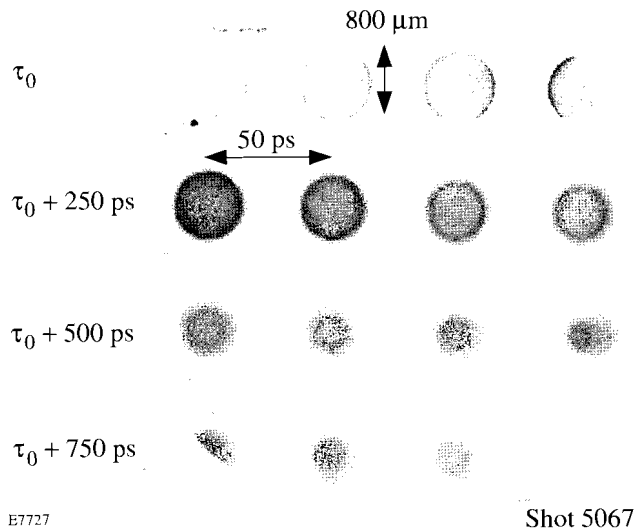
Figure 64.1
Framing-camera images of OMEGA shot 5067. The target was a glass microballoon with an initial wall thickness of 2.3 μm and a diameter of 845 μm. The time delay between strips is 250 ps, and the delay between images on a given strip is 50 ps, time increasing from left to right. The magnification is 6× and the calculated spatial resolution is ~10 μm.

Figure 64.2
Radius of the peak x-ray emission contour for the target of Fig. 64.1 as a function of time. The solid circles are azimuthal averages obtained from the framing-camera images of Fig. 64.1, and the open circles are predictions of the one-dimensional code LILAC.

To obtain a more quantitative understanding of the framing-camera images, the azimuthally averaged radius of the peak emission contour for each frame of Fig. 64.1 has been plotted in Fig. 64.2 as a function of time. Predictions based on the one-dimensional code *LILAC* are also plotted. *LILAC* uses a straight-line radiation transport algorithm to replicate the images, with spatial smearing based on the resolution of the pinhole. The temporal response of the diagnostic is modeled as being Gaussian in shape, with a 40-ps FWHM. Since no absolute timing fiducial is currently available for the camera, the zero time reference between the two data sets was taken as being the one that gave the best fit between the two. The time τ_0 of the first frame of Fig. 64.1 is then −200 ps, where $\tau = 0$ corresponds to the peak of the laser pulse. As can be seen, the predictions for the hydrodynamic motion of the shell are in good agreement with the experiment throughout the acceleration phase of the implosion ($\tau \leq 200$ ps). However, during the subsequent coast phase of the implosion and at the onset of stagnation, the experiment deviates from the *LILAC* prediction. Emission from the glass comes from smaller radii than predicted, with the radius of peak emission continuing to decrease linearly with time until its stagnation at ~350 ps. This departure from one-dimensional predictions may be due to the present level of laser-beam uniformity, in which case better results can be expected when beam smoothing is employed on the system. The successful deployment of this first x-ray

framing camera and the data obtained from it will allow improvements in target drive to be assessed when beam-smoothing techniques are implemented.

2. Kirkpatrick-Baez Microscope

A Kirkpatrick-Baez (KB) microscope—one of a set of new microscopes that incorporate improvements over the design used previously at LLE[3]—has been used to obtain time-integrated x-ray images of the initial target implosions. The reflective optics are Ir coated, extending their useful band up to 8 keV, while the resolution at the center of the field of view is ~5 μm.[4] The KB microscopes thereby provide high-resolution, relatively hard x-ray images of target emission. They have been designed with precision pointing and focusing and are being fully calibrated in the x-ray laboratory at LLE. Eventually, the microscopes will be used for space-resolved continuum spectroscopy of implosions by incorporating a diffraction grating,[5] and for framed monochromatic imaging by attaching a crystal monochromator and a framing camera assembly.[4] The monochromator/framing camera attachment is being built by the laser fusion group at the Los Alamos National Laboratory.[6]

For the initial implosion experiments on OMEGA, a single KB microscope was deployed on the target chamber with a

simple arrangement of thin metallic filters. X-ray film (Kodak DEF) was used to record the images. Four images were obtained per shot through various filters. Since the targets used in these experiments were principally glass microballoons filled with either DD or DT, and since the glass contained a significant amount of a high-Z element (1%–2% RbO_2 molar), the shell emitted copious levels of relatively hard x rays (>4 keV). It was therefore necessary to filter the flux from the targets to limit the film exposure. Figure 64.3 shows the calculated response of the KB microscope versus energy for the Ir-coated mirrors and for a filtration of 203.2 μm of Be in combination with 101.6 μm of Al. The effective energy band is from 5 to 8 keV.
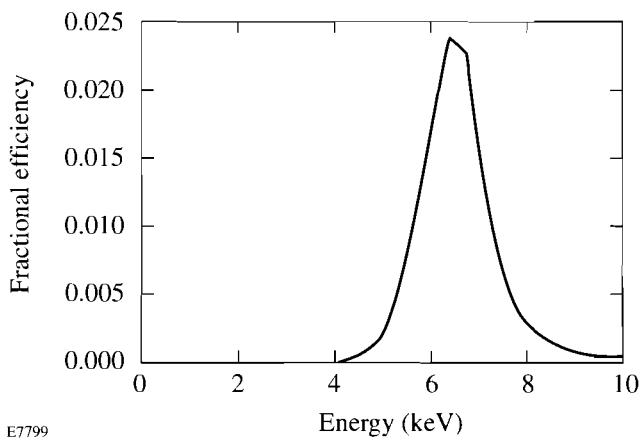
Figure 64.3
Calculated response of the KB microscope versus energy for 0.70° Ir-coated mirrors with a filtration of 203.2 μm of Be in combination with 101.6 μm of Al.

Figure 64.4 shows a comparison of pinhole camera and KB microscope images obtained on shot 5039. The target was a DT-filled glass microballoon overcoated with a 2-μm layer of CH. The increased resolution evident in the KB microscope image illustrates the benefit of the higher resolution and increased sensitivity of the KB microscope. The x-ray pinhole camera and the KB microscope were positioned within 10° of each other on the target chamber, minimizing differences due to view direction. They were similarly filtered so as to be sensitive to x rays of >5-keV energy. The pinhole size was 10 μm and the magnification was 4.0. The microscope was operated at a magnification of 12.9. Both images were recorded on Kodak DEF film. One benefit of the increased sensitivity of the microscope is the ability to operate at higher magnifications, thereby reducing film grain noise as a contribution to image blurring. Clearly the increased spatial resolution allows for the imaging of finer details in the stagnation core.

For purposes of comparison with the previously described framing-camera results, Fig. 64.5(a) shows an image from shot 5067. The stagnation core can again be seen in this image. In this shot, as with many others not shown here, the right-hand side of the shell is much brighter than the left-hand side. A significant part of this effect is due to a systematic focus offset of the beams illuminating the left side of the target, a problem that has since been corrected. Using an intensity-converted horizontal lineout through the image [shown in Fig. 64.5(b)], the diameter of the stagnated shell can be estimated to be 192 μm, based on the locations of peak emission on either side of the center. (The intensity conversions were accomplished using the semi-empirical formulas of Henke *et al.*[7] and assuming an energy of 6 keV for the optical densities measured
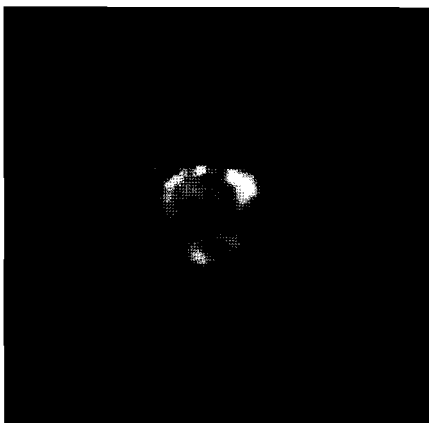
(a) Pinhole camera image (b) KB microscope image
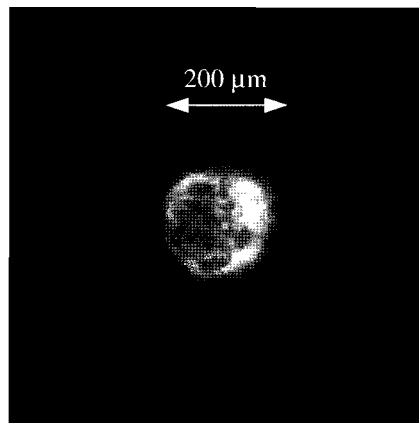

Figure 64.4
(a) Pinhole camera image and (b) KB microscope image of a 20-atm DT-filled glass microballoon of 840-μm diameter and 2-μm wall thickness, coated with 2 μm of CH (shot 5039). The two images have the same spatial scale and are viewed from within 10° of the same direction. The increased spatial resolution of the KB microscope is evident.
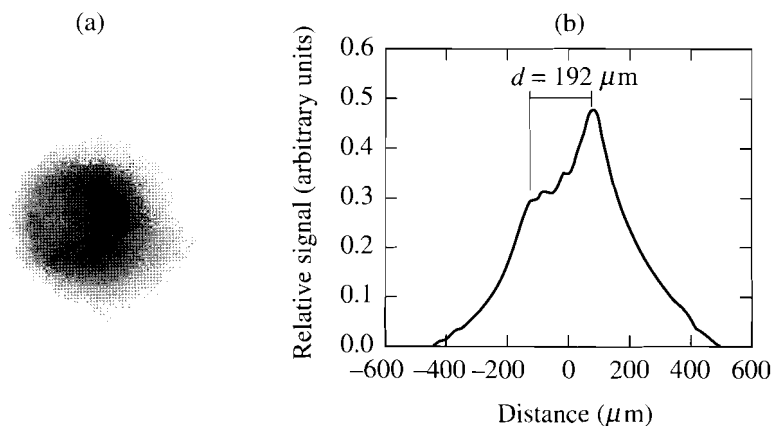
(a)

(b)

Figure 64.5

(a) KB microscope image of OMEGA shot 5067. The reflective optics are Ir coated, extending their useful band up to 8 keV, while the resolution at the center of the field of view is ~5 μm. (b) An intensity-converted horizontal lineout of the image in (a). The diameter of the stagnated shell is estimated to be ~192 μm.

E7800

in the DEF-recorded image.) *LILAC* predictions (Fig. 64.6) indicate a somewhat larger stagnated shell diameter of 275 μm. This disagreement is consistent with what was seen with the framing-camera data above.
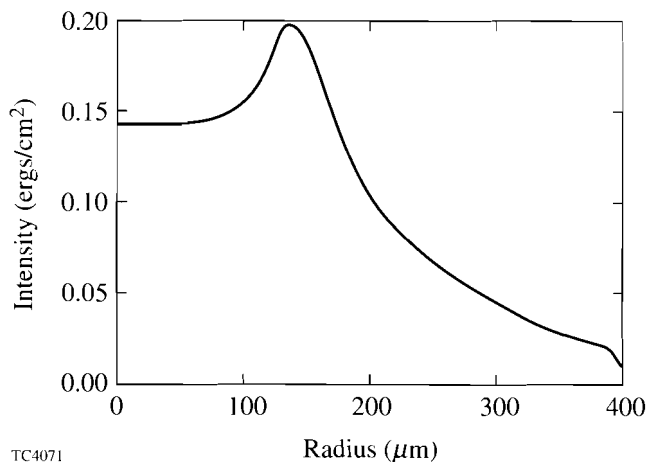
TC4071

Figure 64.6

LILAC simulation of Fig. 64.5(b). The diameter of the stagnated shell, based on the location of peak emission, is predicted to be ~275 μm.

Fusion Experiments

A set of diagnostics that provided measurements of the neutron yield and the fuel ion temperature was used for these initial experiments. The neutron yield was measured by activation methods and scintillator-photomultiplier systems. Ion temperatures were measured using current-mode, quenched-scintillator/fast-photomultiplier detectors, with signals recorded by wide-bandwidth transient digitizers. Several detectors for both yield and ion temperature were used for each experiment.

The activation systems include copper and sodium activation for the detection of 14.1-MeV neutrons produced by DT fuel mixtures, and indium activation for the measurement of 2.45-MeV neutrons produced by pure deuterium fuel. The activation systems have been calibrated by the associated particle technique in a collaborative effort with the State University of New York at Geneseo. Two of the activation samples are inserted near the target (copper sample at 40 cm, indium sample at 25 cm) by a pneumatically operated rapid extractor. This system automatically transports the sample to the counting area, allowing rapid measurement while reducing the radiation exposure of personnel. On high-yield DT fuel target shots, the copper activation sample is placed 6.6 m from the target chamber in a holder near the other diagnostics (see Fig. 64.7). The sodium activation system uses self-activation/ self-detection of sodium in a sodium-iodide gamma-ray detector crystal, which is located 6.6 m from the target chamber.[8]

A scintillator-photomultiplier system is also used to measure yield. This instrument consists of several large scintillators mounted at 6.6 m from the target and used as neutron time-of-flight spectrometers. These "yield" scintillators have active volumes of 2,500 and 44,000 cm^3. The primary purpose of these devices is to allow the measurement of low primary and secondary yields. In the present high-yield experiments, the gain of the photomultipliers was reduced to prevent saturation. The data-acquisition subsystem consists of both transient recorders and, optionally, gated charge integrators. The charge integrators are gated to record individually the 2.45-MeV and the 14.1-MeV neutron signals for each detector. The scintillator yield measurements are calibrated *in situ* by comparison with the activation systems for both 2.45-MeV and 14.1-MeV neutrons.

In, Si activation
Cu activation
6.6 m
Target bay floor
Cu activation (2)
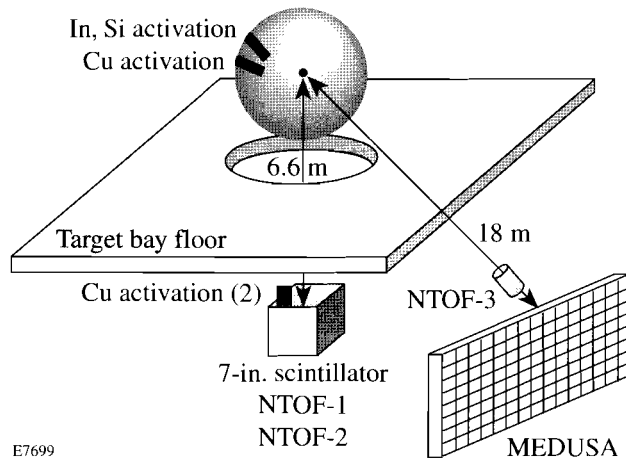7-in. scintillator
NTOF-1
NTOF-2
E7699
NTOF-3
18 m
MEDUSA

Figure 64.7
Schematic of the target chamber and the location of some of the neutron diagnostic systems.

Time-of-flight spectroscopy, using a GHz-bandwidth scintillator-photomultiplier-digitizer, currently provides ion-temperature measurements with low-temperature thresholds of 3.5 keV (for 14.1-MeV neutrons) and 0.2 keV (for 2.45-MeV neutrons). These detectors, along with the other scintillation detectors, are housed 6.6 m beneath the target chamber in a bunker with 20-cm-thick concrete walls and a 6-cm-thick lead faceplate to reduce the effects of prompt n-γ radiation (see Fig. 64.7). An additional fast time-of-flight detector is being installed in the neutron diagnostic room at a distance of 18 m from the target chamber; this will provide the higher resolution required for low-temperature DT implosion experiments.

A series of experimental shots were designed to provide a wide range of DT and DD yields to aid in the calibration of the activation counters and scintillators. Table 64.I presents typical neutron data from five target shots. The system response

(including the scintillator, photomultiplier, coaxial cable, and recording digitizer) for neutron time-of-flight measurements was determined by applying a short (100-ps) light pulse to the detector package. This system response was deconvolved from the raw experimental signal (an example of which is shown in Fig. 64.8) to obtain the neutron-averaged ion temperatures quoted in Table 64.I. The one-dimensional *LILAC* predictions for yield, neutron-averaged ion temperature, and convergence ratio are also included in Table 64.I. The five shots corresponded to a wide range of targets. Shot 5241, which gave the highest ion temperature, used a thin (2.7-μm) bare glass shell, while the other shots included plastic shells (shots 5212 and 5221) and plastic-coated glass shells (shots 5049 and 5276).

After the calibration series of shots, emphasis was placed on maximizing the yield in both DT and DD implosion experiments. The design of these experiments focused mainly on
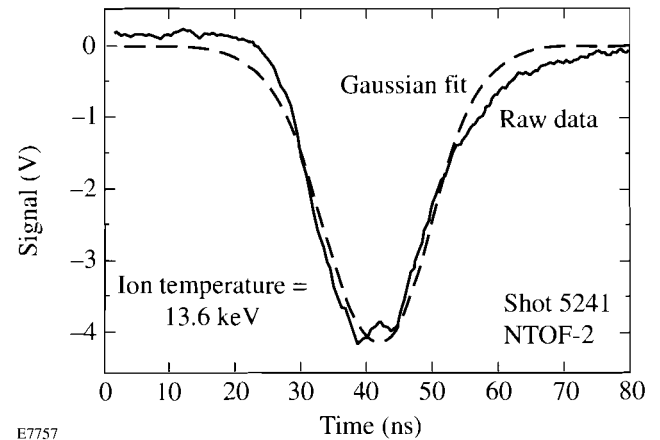
Figure 64.8
Signal obtained from a scintillator-photomultiplier neutron time-of-flight detector placed at 6.6 m from the target. The Gaussian fit to the raw data corresponds to an ion temperature of 13.6 keV.

Table 64.I: Summary of neutron yields and ion temperatures.

Shot Number	Fuel	Neutron Yield		Ion Temperature (keV)		Calculated Convergence Ratio
		Measured	Calculated	Measured	Calculated	
5049	DT	1.0×10^{14}	2.0×10^{14}	—	15.0	4.4
5212	DD	5.9×10^{10}	1.7×10^{11}	4.7	2.3	19.3
5221	DD	4.8×10^{10}	1.6×10^{11}	6.1	2.4	19.0
5241	DD	5.7×10^{11}	9.3×10^{11}	13.6	17.0	5.2
5276	DT	4.9×10^{13}	1.7×10^{14}	7.8	9.3	8.6

reducing the calculated convergence ratio of the pellet during the implosion. The calculated convergence ratio is defined as the ratio of the initial fuel-pusher interface radius to the calculated radius of this same interface at stagnation. It is well established on the basis of stability considerations that one is able to obtain an increasing fraction of the one-dimensionally calculated neutron yield as the calculated convergence ratio is decreased.[9,10] With the limited set of targets available, several options were investigated to reduce the calculated convergence ratio of the implosions while maximizing the one-dimensional yield. A solution was found in overcoating the bare glass microballoons with several microns of parylene and then targeting OMEGA at tighter-than-normal focusing.

Results for the DT neutron yield as a function of UV energy on target are shown in Fig. 64.9. The maximum yield (1.0×10^{14}) is the highest recorded to date from any laser system. It must again be noted that precision energy balance, power balance, and beam smoothing have not yet been implemented on OMEGA. Consistent with the discussion of the x-ray images above, the symmetry of the implosions may well have suffered from high initial levels of on-target irradiation nonuniformity. For the shot producing 10^{14} neutrons, the calculated convergence ratio was 4.4 and the yield was a fraction 0.52 of the one-dimensional yield. The fusion energy released from this shot was equal to 1% of the laser energy delivered to the target (1% of scientific breakeven).

Figure 64.9
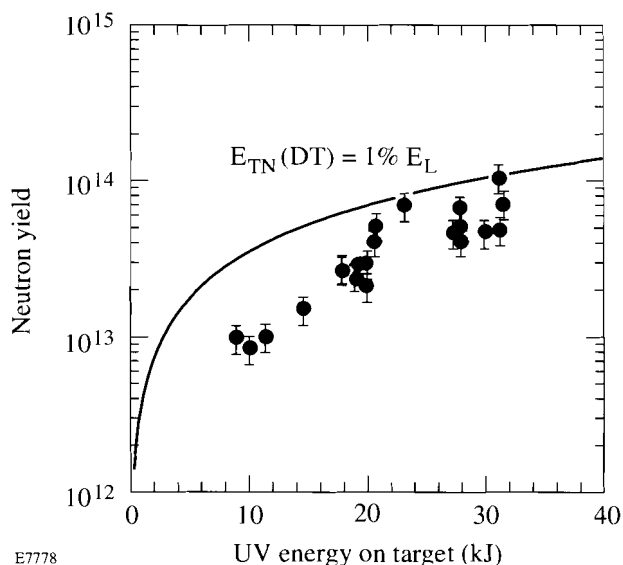Performance summary of initial high-yield implosion experiments. The solid curve indicates the neutron yield corresponding to a fusion energy release equal to 1% of the UV energy on target (1% of scientific breakeven).

X-Ray Spectroscopy

It was predicted that high electron temperatures up to 5 keV could be achieved on OMEGA by using relatively thin shell targets. These temperatures would occur at modest compressed densities (~1 to 5 g/cm^3), and the ion temperatures would peak at above 10 keV at the center of the compressed core. New diagnostic techniques were thus developed for measuring these temperatures, using K-shell line and continuum spectroscopy of krypton-doped targets.[11,12] (See also the next article in this issue.) A series of krypton-doped, deuterium-filled targets were shot on OMEGA to test these predictions. A strong K-shell Kr spectrum was indeed observed, and high electron temperatures were determined, in close agreement with code predictions. These targets were similar to those of Table 64.I for which high ion temperatures were measured.

The krypton lines observed in these shots have the highest energies, 13 to 16 keV, that have been observed in laser-fusion experiments. Previously, only the Kr^{+34} resonance line (at 13.1 keV) had been observed, using a Von-Hamos focusing spectrometer on the 24-beam OMEGA system operating in short-pulse mode (100 ps, 6 TW).[13]

Results from the present experiments are shown from two Kr-doped target shots for which the experimental parameters are listed in Table 64.II. In the first shot, a Si(111) diffracting crystal was used, tuned to detect the spectral range of 8 to 13 keV, while in the second shot a LiF(200) crystal was used, tuned to the range of 12 to 20 keV.

Figure 64.10 shows a comparison between the measured and simulated spectra from shot 4952. In Fig. 64.10(a), the raw experimental spectrum is shown in film density units. In Fig. 64.10(b), a time- and space-integrated *LILAC* simulation of the same spectrum is shown. This simulation was carried out using a non-LTE radiation transport postprocessor that includes a time-dependent multispecies ionization and level-population model based on a simple screened-hydrogenic description of the principal atomic states. Figure 64.11 shows a similar comparison between experiment and simulation for shot 5110. In both cases the simulated spectrum is plotted on a linear scale, in line with the fact that film density and exposure are approximately linear for the photon energy range detected (see below). The He-α line in Fig. 64.11 has a film density higher than 5 and saturates the film. Instrumental broadening of the lines has been included in the simulation. In comparing the measured and simulated spectra, it should be noted that *LILAC* does not calculate the satellite lines on the low-energy side of the He-α and He-β lines, nor the lines above

E7778

$E_{TN}(DT) = 1\% \; E_L$

Table 64.II: Experimental parameters of two CH target shots analyzed using krypton line and continuum spectroscopy.

Shot No.	Target diameter (μm)	Target thickness (μm)	DD pressure (atm)	Krypton pressure (atm)	Laser energy (kJ)
4952	870	10.0	10	0.03	23.6
5110	874	12.4	10	0.03	29.5
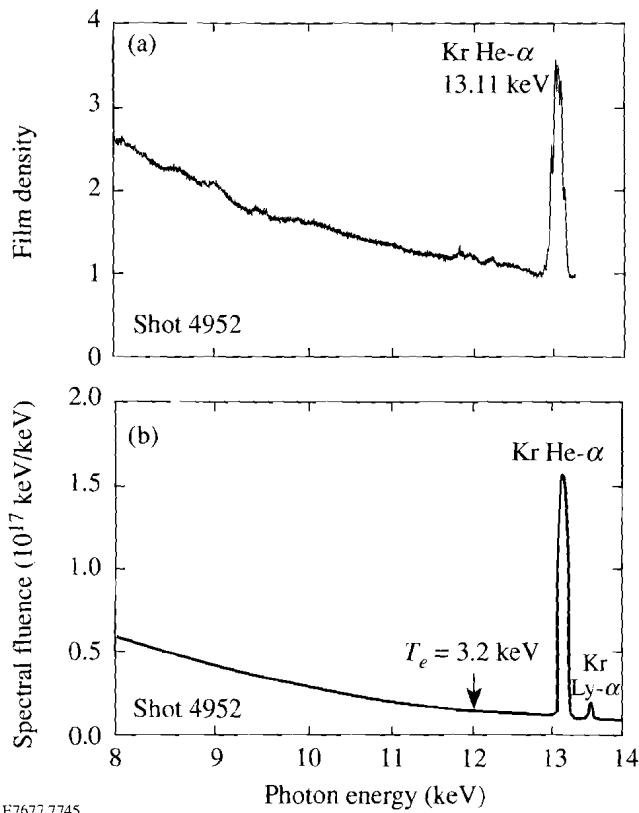
Figure 64.10
(a) Experimental spectrum from Kr-doped, DD-filled target shot 4952.
(b) *LILAC* simulation of the same spectrum. The continuum slope around
12 keV in (b) implies T_e = 3.2 keV. Instrumental broadening of the calculated lines has been included. The simulation does not include the satellite
lines on the low-energy side of the He-α line.

Figure 64.11
(a) Experimental spectrum from Kr-doped, DD-filled target shot 5110. The
He-α line has a film density >5 and saturates the film. (b) *LILAC* simulation
of the same spectrum. The simulation does not include the satellite lines on
the low-energy side of the He-β line or the lines above 16 keV. Instrumental
broadening of the calculated lines has been included.

16 keV. Also, accounting for film and crystal calibration increases the experimental high-energy continuum and brings it into closer agreement with the simulated one.

To analyze the spectra quantitatively, the responses of the film (Kodak DEF) and the crystals (LiF and Si) have to be known. Henke[14] published a model for the response of DEF film and normalized it to experimental values below 10 keV. Using this model and updated x-ray absorption coefficients in the film constituents, we calculated the film response for photon energies below and above 10 keV. Figure 64.12 shows the results in the 1- to 30-keV range, for various film density values between D = 0.5 and D = 3 (in increments of 0.5), assuming that the film density was measured with a numerical
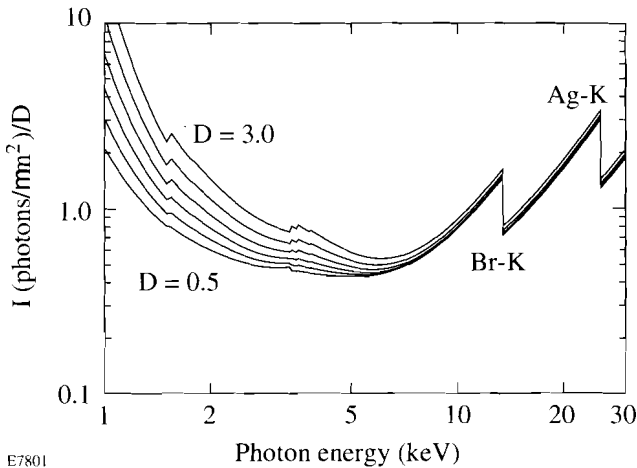
Figure 64.12
Calculated DEF film response for various film-density values between $D = 0.5$ and $D = 3$ (in increments of 0.5), assuming that the film density was measured with a numerical aperture of 0.25. Jumps in response due to the K edges of Br and Ag are marked. Henke's model was used, with updated coefficients for x-ray absorption in the film constituents.

aperture of 0.25. Jumps in film response due to the K edges of Br and Ag are marked. Figure 64.12 shows that for film densities below $D \sim 2$ and photon energies above ~6 keV, the film density is proportional to exposure. This is the reason for plotting the spectral fluence in Figs. 64.10 and 64.11 on a linear scale.

For the Si(111) crystal, published diffraction data[15] were used. For the LiF(200) crystal, published calibration data[16] were used as well, and they agree with previous data for LiF(200) crystals used at LLE.[17] It should be emphasized that for the purpose of temperature determination only the changes with photon energy of the film and crystal responses are required. Using the film exposure $I(\text{keV/cm}^2)$ and the integrated crystal reflectivity R, the spectral fluence per unit solid angle of the target can be determined. For example, the resulting continuum fluence at a photon energy $E(\text{keV})$ is given by $S(\text{keV/keV}) = I(E)L^2 \tan\theta_B/(RE \cos\alpha)$, where L is the target-film distance (along the ray), θ_B is the Bragg angle, and α is the angle of incidence on the film.

Using the film and crystal calibrations as described above, the spectral data were converted to spectral fluence in absolute units. The continuum slopes in the ranges 8 to 13 keV for Fig. 64.10 (shot 4952) and 16.5 to 20.5 keV for Fig. 64.11 (shot 5110) were used to estimate the electron temperature by fitting exponential curves. Figure 64.13 shows the result for shot

4952 where fitting to the high-energy part of the continuum yields a temperature of 3.1 keV. For shot 5110, the measured temperature was 4.0 keV. The simulated spectra show, in agreement with the experiment, that higher-energy portions of the continuum yield higher temperatures. This is because these portions are preferentially emitted at the higher-temperature regions (and times). The experimental result for shot 4952 agrees with the simulated temperature of 3.2 keV, obtained from the slope of the simulated spectrum in the same spectral range. The absolute magnitude of the continuum is lower than that of the simulated spectrum by only about a factor of 1.5; comparison of the absolute magnitude of spectral lines is complicated by such factors as detailed atomic physics modeling and the spatial distribution of the emitting source.
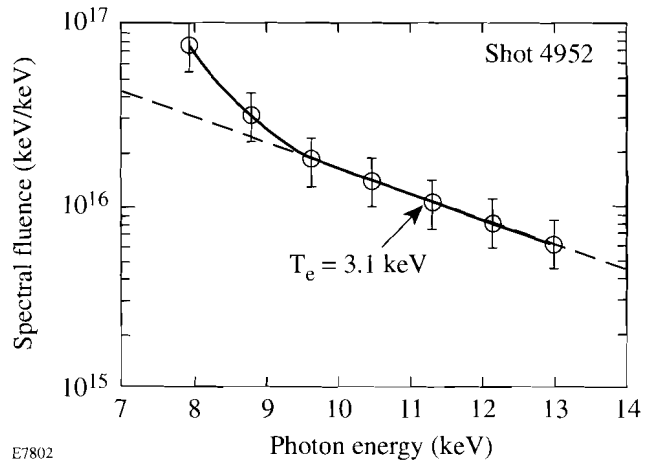
Figure 64.13
Experimental continuum spectrum of Fig. 64.10(a) after absolute calibration. The slope in the 10- to 13-keV range indicates an electron temperature of $T_e = 3.1$ keV.

LILAC results show that the space-averaged temperatures around peak compression in these shots were 3 to 4 keV and the maximum temperatures were 5 to 6 keV. The ion temperatures in such thin-shell implosions are predicted to be significantly higher than the electron temperatures, consistent with the experimental results reported in Table 64.I.

An additional method for estimating the electron temperature involves the measured intensity ratio of the Lyman-α line of Kr^{+35} to the helium-β line of Kr^{+34}. As described in Ref. 11, this ratio is highly sensitive to the temperature below ~8 keV and changes very little with density. Also, the spectral lines chosen can have a relatively low opacity (unlike that of the He-α line); this is true for the krypton fill pressure and compression in these experiments. However, it was shown[18]

that a high opacity of the He-α line can indirectly increase the Lyman-α to helium-β ratio for the same temperature; this is because the He-α opacity facilitates ionization of the helium-like state through $n = 2$ excited Kr^{+34} ions. Figure 64.14 shows curves of the calculated intensity ratio[12] of these two lines, with and without a correction for the opacity of the He-α line. The curve used here for the temperature determination corresponds to the opacity ($\tau = 15$) for shot 5110, estimated on the basis of *LILAC*-predicted profiles. A complication arises because the wavelength of the K edge of Br (in the film grains) practically coincides with that of the Lyman-α line of Kr^{+35}, giving rise to a jump in the film response at that wavelength. The corresponding jump in the measured spectrum should be smaller than what is indicated in Fig. 64.12 because of the finite spectral resolution of the spectrometer (which blends the intensity around the jump). To account approximately for this effect, the continuum at energies above the K edge was extrapolated toward lower energies and the resulting jump in the continuum was subtracted from the measured peak at 13.5 keV. The resulting estimated temperature (see Fig. 64.14) is 4.1 keV.
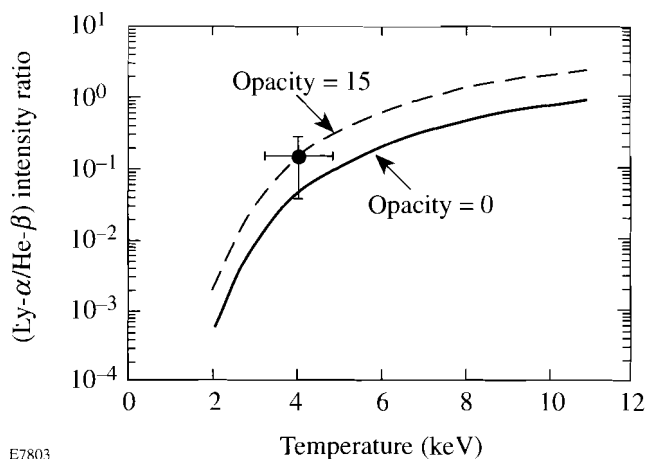
Figure 64.14
Electron-temperature determination by the measured intensity ratio of the Lyman-α to helium-β lines. The curves of calculated intensity ratio are taken from Ref. 12. This ratio depends weakly on the density, but it does depend significantly on the opacity of the He-α line. The curve used here for the temperature determination corresponds to the estimated opacity ($\tau = 15$) for shot 5110.

In the future, the ion temperature in similar experiments will be measured through the Doppler broadening of Kr lines, using a recently completed focusing x-ray spectrograph of high spectral resolution. Finally, the measurements will be extended to include L-shell Kr lines. It is shown in the following article that the simultaneous measurement of K- and L-shell lines can be used to determine the fuel ρR and to study core-shell mixing.

Summary

Initial target experiments have been performed with the upgraded OMEGA laser, using glass and CH microballoons filled with either pure deuterium or DT. During these experiments several key diagnostic systems have been activated including an x-ray framing camera, a Kirkpatrick-Baez (KB) microscope, copper and indium neutron activation counters, scintillator-photomultipliers, and a crystal spectrometer. The framing camera has been used to diagnose the target implosion dynamics, which agree well with predictions up to the stagnation phase. Deviations from predictions, also seen using the KB microscope, are consistent with the present lack of beam smoothing on the laser. Neutron yields up to 10^{14} (1% of scientific breakeven)—the highest recorded to date from any laser system—have been obtained from DT targets and fuel ion temperatures up to 13 keV have been measured. Spectroscopic diagnostics based on the continuum slope and krypton line ratios have demonstrated electron temperatures from 3 to 4.1 keV. Taken as a whole, these results demonstrate a successful integration of laser operations and target diagnostics into the OMEGA experimental system.

ACKNOWLEDGMENT

REFERENCES

1. Laboratory for Laser Energetics LLE Review **63**, NTIS document No. DOE/SF/19460-91, 1995 (unpublished), p. 99.

2. D. K. Bradley, P. M. Bell, O. L. Landen, J. D. Kilkenny, and J. Oertel, Rev. Sci. Instrum. **66**, 716 (1995).

3. Laboratory for Laser Energetics LLE Review **46**, NTIS document No. DOE/DP/40200-156, 1991 (unpublished), p. 91.

4. F. J. Marshall and Q. Su, Rev. Sci. Instrum. **66**, 725 (1995).

5. F. J. Marshall, J. A. Delettrez, R. Epstein, and B. Yaakobi, Phys. Rev. E **49**, 4381 (1994).

6. J. A. Oertel, T. Archuleta, L. Clark, S. Evans, A. Hauer, F. J. Marshall, C. G. Peterson, T. Sedillo, C. Thorn, and R. G. Watt, in *Ultrahigh- and High-Speed Photography, Videography, and Photonics '95*, edited by D. R. Snyder and G. A. Kyrala (SPIE, Bellingham, WA, 1995), Vol. 2549, p. 82.

7. B. L. Henke, E. M. Gullikson, and J. C. Davis, At. Data Nucl. Data Tables **54**, 181 (1993).

8. R. A. Lerche, Lawrence Livermore National Laboratory Laser Program Annual Report 1978, UCRL-50021-78 (1979), p. 6-53.

9. Laboratory for Laser Energetics LLE Review **28**, NTIS document No. DOE/DP/40200-26, 1986 (unpublished), p. 159.

10. Laboratory for Laser Energetics LLE Review **40**, NTIS document No. DOE/DP/40200-102, 1989 (unpublished), p. 171.

11. Laboratory for Laser Energetics LLE Review **61**, NTIS document No. DOE/SF/19460-58, 1994 (unpublished), p. 1.

12. B. Yaakobi, R. Epstein, C. F. Hooper, D. A. Haynes, and Q. Su, submitted for publication to the Journal of X-Ray Science and Technology.

13. B. Yaakobi and A. J. Burek, IEEE J. Quantum Electron. **QE-19**, 1841 (1983).

14. B. L. Henke et al., J. Opt. Soc. Am. B **3**, 1540 (1986).

15. G. Brogren and E. Lindén, Ark. Fys. **22**, 535 (1962).

16. D. B. Brown and M. Fatemi, J. Appl. Phys. **45**, 1544 (1974).

17. A. J. Burek and B. Yaakobi, Final Report to the National Bureau of Standards contract NB81NAHA2032 (1983), Appendix A.

18. C. J. Keane et al., Phys. Fluids B **5**, 3328 (1993).

Diagnosis of High-Temperature Implosions Using Low- and High-Opacity Krypton Lines

High-temperature laser target implosions can be achieved by using relatively thin-shell targets. Electron temperatures of up to 5 keV at modest compressed densities ($\sim$1 to 5 g/cm^3) are predicted for such experiments and have been diagnosed in an initial series of implosion experiments on the upgraded OMEGA laser (see the previous article). The corresponding ion temperatures are predicted to be higher, peaking above 10 keV at the target center. The possibility of using krypton doping for diagnosing the core temperature of imploding targets was discussed in an earlier issue of the LLE Review.[1] In that work, a simplified analysis for the case of optically thick lines was performed, using approximate Stark profiles. In the present work, the use of detailed Kr Stark profile calculations by C. F. Hooper et al. from the University of Florida improves and extends the earlier analysis. The use of krypton doping is a powerful technique for diagnosing target implosions, as the implosion dynamics are to lowest order independent of doping and different levels of doping can be used to permit the measurement of different quantities. For example, low doping levels allow low-opacity lines to be used to measure the ion temperature via Doppler broadening, while higher doping levels allow the density-radius product (ρR) of the compressed fuel to be measured from high-opacity lines. In high-density implosions, low-opacity lines can be used to diagnose the density through Stark broadening, and higher-opacity lines can be used to estimate the extent of mixing.[1]

Calculations have been carried out using the *LILAC* code for a CH shell of 1-mm diameter and 10-μm thickness, filled with a 10-atm pressure of DT.[1] The laser energy was 30 kJ in a Gaussian pulse of 650-ps width. Results have shown that the core electron temperature and density are fairly uniform, at $\sim$5 keV and $\sim$4.5 g/cm^3, respectively. On the other hand, the ion temperature ranges from $\sim$6 keV to $\sim$12 keV and is centrally peaked. Code calculations have shown that the core temperatures are hardly changed by the addition of 0.01 atm of krypton. By adding 0.1 atm of krypton, the peak electron temperature drops a little to about 4 keV. The predicted spectra have been calculated by the *LILAC* code and a non-LTE post-processor, which includes transitions between actual atomic

configurations, using Doppler and Stark profiles. The calculated line intensities even for the 0.01-atm case are very substantial (of the order of 10^{17} keV/keV), and the contrast of line to continuum is better than a factor of 4 for the He-β line. Furthermore, the shape of the spectrum above $\sim$10 keV at peak compression differs little from the time-integrated spectrum because most of the emission originates from peak compression. Thus, a time-integrated measurement in this spectral range yields the conditions at peak compression with reasonable reliability.[1]

Diagnosis of Density Using Low-Opacity Lines

A recently developed multielectron line-profile formalism and code (MERL)[2,3] has been used to calculate Stark-broadened emission line profiles for the Kr K-shell lines. The analysis in this article relies in particular on the helium-β transition (3^1P–1^1S), and the profiles shown here pertain to this line. Broadening due to perturbing ions is treated in the quasi-static ion approximation, and the dynamic effect of electrons is calculated using a second-order relaxation theory. Ion- and electron-radiator interactions are computed in the dipole approximation. Necessary atomic physics data (energy-level structure and reduced dipole matrix elements) were calculated using Cowan's[4] multiconfiguration atomic structure code, using the Hartree-Plus-Statistical-Exchange method for approximating the potential energy function due to the electrons, and including relativistic corrections.

Figure 64.15 shows examples of calculations carried out by the group at the University of Florida. The Stark profile of the helium-β line of Kr^{+34}, of 0.8033-Å wavelength, is calculated for two densities: (a) 1×10^{24} cm^{-3} and (b) 5×10^{24} cm^{-3}. It is assumed that the krypton constitutes a small fraction mixed into the fuel and that most of the perturbers are fuel ions. The effect of Doppler broadening is also calculated, at an assumed ion temperature of 10 keV. The shape of the Stark profile is significantly affected by relativistic effects in the atomic physics due to the relatively high nuclear charge Z of krypton. There are two dipole-allowed transitions from the $1s3l$ upper-level manifold to the ground state. The unperturbed singlet-singlet
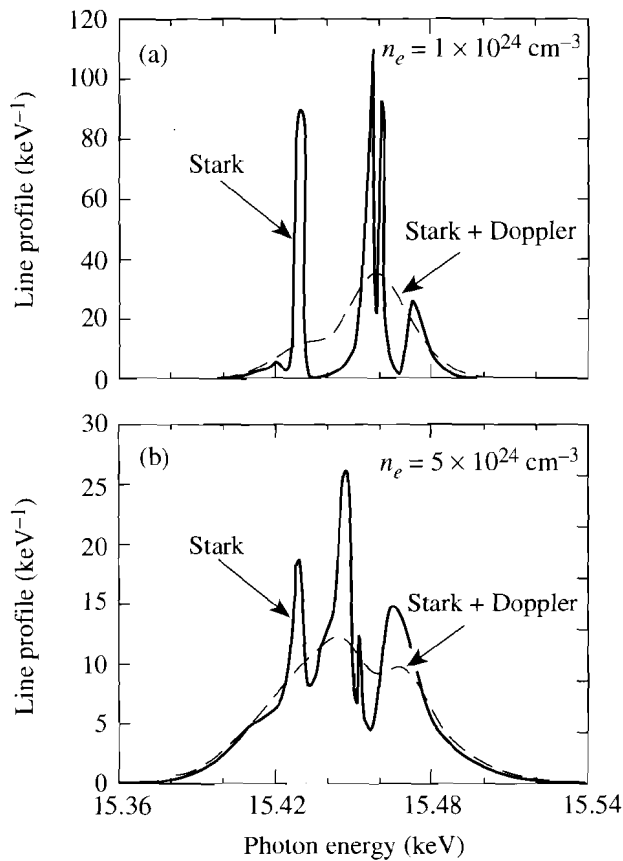
Figure 64.15

Calculated Stark profile of the He-β line of Kr^{+34} (solid line) and the combined Stark and Doppler profile corresponding to an ion temperature of 10 keV (dashed line). Electron densities n_e of (a) 1×10^{24} cm^{-3} and (b) 5×10^{24} cm^{-3} were assumed.

transition is located at 15,451 eV, and the triplet-singlet transition is located at 15,426 eV. Additional peaks appear because of field mixing among the levels of the upper manifold.

Comparison of Figs. 64.15(a) and 64.15(b) clearly shows the effect of increasing density on the profile. The lower density, 1×10^{24} cm^{-3} (~4.5 g/cm^3), is at the upper end of the expected density range for the high-temperature target shots. The higher density, 5×10^{24} cm^{-3} (~22.5 g/cm^3), corresponds to future experiments where both high density and high temperature will be achieved. For the lower-density case the combined profile width is dominated by the Doppler broadening and can thus yield the ion temperature. To measure this width, a spectral resolution $\lambda/\Delta\lambda$ greater than ~1000 is required. This is not easily achievable with a flat crystal spectrometer, unless employed at a very large distance from

the target; however, a Rowland-circle focusing spectrograph can readily achieve this.[5] In going from the lower density (1×10^{24} cm^{-3}) to the higher density (5×10^{24} cm^{-3}) the line width more than doubles, reflecting the increasing effect of the Stark broadening. It should be noted, however, that this broadening is mostly the result of the increase in intensity of forbidden components. Only at much higher densities will the total width of the manifold be determined by the Stark width rather than by the separation of the components. For the density range covered by Fig. 64.15, density signatures are provided by the width as well as the shape of the compound profile, which in turn is determined by the change in intensity and spectral position of the various components. In particular, in going from the lower to the higher density, the peak intensity of the compound profile shifts to lower energies by about 10 eV (due to the so-called "level repulsion" in second-order perturbation theory). To measure this shift, a spectral resolution $\lambda/\Delta\lambda$ greater than ~2000 is required.

Diagnosis of ρR using High-Opacity Lines

Optically thick spectral lines can be used to deduce the ρR of the compressed core. The self-absorption of spectral lines (i.e., the absorption by the same transition as that of the emission line) affects both the emergent line intensity as well as its spectral shape. Self-absorption leads to broadening; for a spatially uniform temperature the spectral profile will tend to be flat-topped, whereas for a radially falling temperature the line profile may have a central minimum. In the past, the broadening due to self-absorption of the Lyman-α line of argon was employed to estimate the core ρR.[6] As explained in Ref. 6, the density has to be known (by fitting Stark profiles to an optically thin line) to deduce the ρR from an optically thick line. Alternatively, the width of several optically thick lines in the same line series must be measured.[7] These methods can be employed here as well. However, we pursue an alternative method, based on the intensity of the optically thick line rather than its profile, which does not require a prior knowledge of the density or the use of additional lines.

The intensity of an optically thick line emerging from the plasma volume is related to the escape factor parameter, which has been the subject of numerous publications.[8-11] The escape factor G is defined by

$$G(\tau_0) = \int_{-\infty}^{\infty} P(\delta E) \exp\left[-\tau_0 P(\delta E)/P(\delta E = 0)\right] d(\delta E), \quad (1)$$

where δE is the energy separation from the unperturbed posi-

E7599&7600

tion, $P(\delta E)$ is the line profile at δE in inverse energy units, and $\tau_0 = \tau(0)$ is the optical depth at $\delta E = 0$. The line opacity $\tau(\delta E)$ can be expressed as [see Eq. (8-14) in Ref. 12]

$$\tau(\delta E) = \left(\pi e^2 h / Mmc\right) P(\delta E) \ f \ \rho R \ \varepsilon Q_n, \qquad (2)$$

where M is the krypton ionic mass, m is the electron mass, e is the electron charge, h is Planck's constant, c is the speed of light, f is the absorption oscillator strength of the line, ρR is the total areal density (mostly that of the fuel), ε is the fraction of krypton in the fuel (by mass), and Q_n is the fraction of krypton ions in the absorbing level (i.e., the lower level of the transition). The spectral position $\delta E = 0$, which is somewhat arbitrary, is taken to be 15,451 eV, the unperturbed position of the strongest line.

The escape factor $G(\tau_0)$ in spherical geometry, as given by Eq. (1), corresponds to a point source at the center of the sphere, with τ_0 the opacity integrated over the radius. For a source uniformly distributed over the sphere, Mancini et al.[11] have shown that $G(\tau_0)$ for Holtsmarkian profiles and large opacities is about twice as large as for the point-source case. This indicates that knowing the temperature profile (or the spatial distribution of emitting and absorbing ions) is not critical when using the calculated escape factor for diagnostics. Thus, a two-temperature spatial profile (a hot spot surrounded by a cool absorbing layer) and a uniform temperature profile give an escape factor that differs by only a factor of 2 for any $\tau_0 \gg 1$. To determine which geometry agrees better with the experiment we can examine two experimental signatures: (a) for a uniform source, the core image size at high photon energy will be about the same as that at low photon energy, whereas for a hot-spot source the former will be much smaller than the latter, and (b) for a uniform source the observed line profile will be flat-topped, whereas for a hot-spot source a self-reversal (or minimum) will be observed at the position of the profile peaks. Equation (1) applies to a two-temperature spatial profile but assumes that the line profile is the same in both the emission and absorption regions. This implies a uniform density since the density-dependent Stark broadening dominates the emergent profile for high opacities (see below). As an example, if the absorption line profile is half as wide as the emission profile (indicating a lower density by about a factor of 2.8), the escape factor can be shown to be larger by about 30%.

To obtain the escape factor $G(\tau_0)$ from Eq. (1) for our case, we use profiles such as those in Fig. 64.15. Figure 64.16 shows the escape factor as a function of the opacity at line center (15,451 eV), with and without the Doppler profile contribution. The curves are calculated for an ion temperature of 10 keV. The escape factor G depends on the temperature only through the Doppler contribution. Figure 64.16 shows that we

Figure 64.16

Calculated escape factor of the He-β line of Kr^{+34} for the two electron densities used in Fig. 64.15, as a function of the opacity at the line center (15,451 eV), without the Doppler contribution (solid curves) and with the Doppler contribution (dashed curves). In (a) and (c) the opacity τ_0 at 15,451 eV relates to the total Stark + Doppler profile, while in (b) and (d) the opacity $\tau_{0,S}$ at 15,451 eV relates to the Stark profile only.

can almost eliminate this dependence by plotting G as a function of $\tau_{0,S}$, the opacity at line center due to the Stark profile only. When changing from τ_0 to $\tau_{0,S}$, the curves of total profile shift to opacity values that are larger (since $\tau_{0,S} > \tau_0$) by the ratio $\tau_{0,S}/\tau_0$. The two curves thus plotted are almost coincident. The reason for this is simple: The Doppler profile decays much faster, with increasing separation from line center, than the Stark profile. Thus, the far wings are relatively unaffected by Doppler broadening. However, the escape factor for high opacity values depends only on the far wings [see Eq. (1)]. Therefore, the escape factor for high opacities will be relatively independent of the temperature. Since the profile on the far wings is essentially identical to the Stark profile, the escape factor will depend only on the Stark opacity $\tau_{0,S}$ at line center.

A similar situation will arise if we include ion-dynamic effects in the calculation of the Stark profiles. Effects on the Stark profile of the motion of perturbing ions (which are otherwise assumed stationary) will depend also on the ion temperature and will affect mostly the line center rather than its wings. Thus, the opacity $\tau_{0,S}$ relates to the Stark profile without either the Doppler effect or the ion-dynamic effects.

Comparison of the profiles in Fig. 64.16 shows also the relative insensitivity of the escape factor to the density. As mentioned earlier, for a Holtsmarkian profile and high opacities $G(\tau_0)$ depends only on τ_0 and not on the density (or the line width). For easier comparison, Fig. 64.17 shows the escape-factor curves from Figs. 64.16(b) and 64.16(d), calculated without the Doppler contribution, for the two densities 1×10^{24} cm^{-3} and 5×10^{24} cm^{-3}. As seen, the two profiles overlap to within a factor of ~1.4. Similar agreement is obtained in comparing curves that do include the Doppler broadening. We can thus use Fig. 64.16 to find the quantity $\tau_{0,S}$ from a measured value of the escape factor, without a precise knowledge of the temperature or the density. The question before us now is what does the opacity $\tau_{0,S}$ depend on, i.e., what diagnostic information can be inferred from knowing $\tau_{0,S}$?

From Fig. 64.16, the escape factor for high opacity in the density range (1–5) $\times 10^{24}$ cm^{-3} can be approximated by the relation

$$G\left(\tau_{0,S}\right) \sim 1.3/\left(\tau_{0,S}\right)^{0.9} . \tag{3}$$

E7601
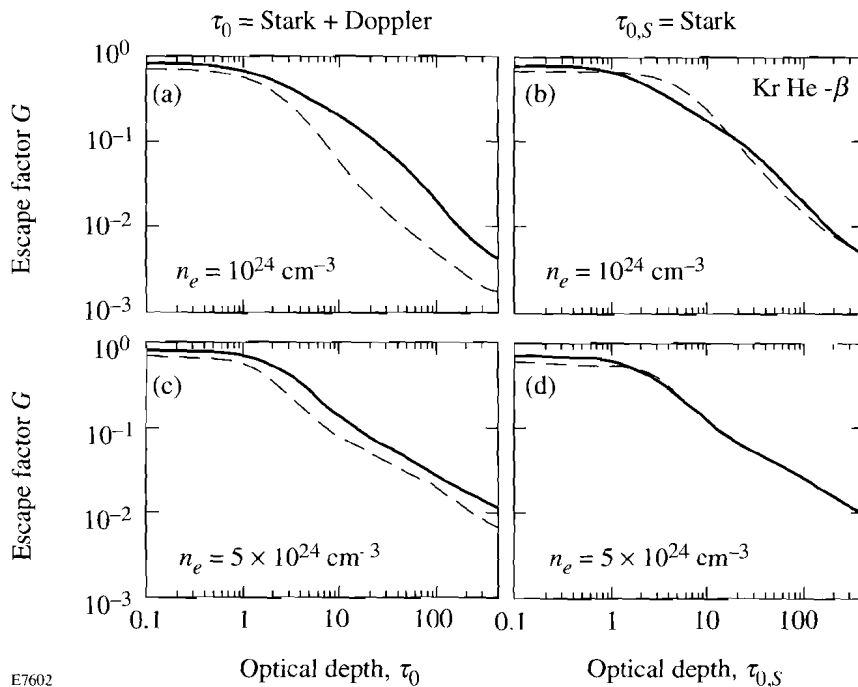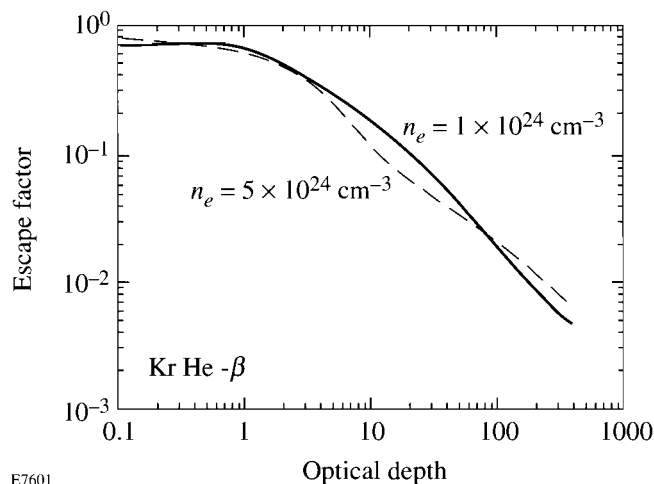
Figure 64.17
Calculated escape factor of the He-β line of Kr^{+34} for two electron densities, as a function of the opacity at line center (15,451 eV), without the Doppler contribution.

Only at much higher densities, where level mixing of the $n = 3$ manifold due to the plasma electric field becomes substantial, will this relation tend to that for the Holtsmarkian profile mentioned above. For that case it was shown earlier[1] that the density dependence of $\tau_{0,S}$ drops out but the determination of $\tau_{0,S}$ (through the measurement of the escape factor) can then yield information on possible mixing. For the density range discussed here, Eq. (3) does lead to a dependence of $\tau_{0,S}$ on the density (or on the ρR), thus providing a diagnostic for ρR. A method for measuring the escape factor was described in Ref. 1.

The diagnostic method for the fuel ρR consists of measuring the escape factor as outlined in Ref. 1, and then deducing $\tau_{0,S}$ from curves like those in Fig. 64.16. It follows from the definition of τ_0 (Eq. 2) that if we substitute $\tau_{0,S}$ for τ_0, the profile $P(\delta E = 0)$ appearing in Eq. (2) should refer to the pure Stark profile $P_S(\delta E = 0)$. This profile can be read off the calculated Stark profiles such as those in Fig. 64.15 and is obviously a function of the density. In the range (1–5) $\times 10^{24}$ cm^{-3}, $P_S(\delta E = 0)$ as a function of the density ρ can be approximated as

$$P_S\left(\delta E = 0\right) \sim 0.4/\rho^{0.88} . \tag{4}$$

In any practical case, the complete profile curves can be used rather than this approximate expression. Further, in an imploding spherical target the following relationship holds:

$$\rho R = \left(3M_F/4\pi\right)^{1/3} \rho^{2/3}, \tag{5}$$

in terms of the total fill mass M_F (fuel and krypton). Combining Eqs. (2), (4), and (5) we can write

$$\rho R = 0.02 A^{3.125} \left(3M_F/4\pi\right)^{1.375} G^{3.437}, \tag{6}$$

where $A = \left(\pi e^2 h/Mmc\right) f \varepsilon Q_n$ [from Eq. (2)]. The quantity Q_n has been shown[1] to be very close to unity over a wide temperature range. This relation is the basis for determining the fuel ρR from a measurement of the escape factor G. As mentioned above, actual calculated curves can be used rather than the approximations given in Eqs. (3) and (4).

Finally, we estimate the expected sensitivity of the method for measuring the fuel ρR. To find G from the intensity ratio of the helium-β and Balmer-α lines,[1] with a precision of $\pm 20\%$, the intensity of each of the lines (in relative units) has to be measured with a precision of $\pm 10\%$. A method for the relative calibration of the two instruments measuring the two different wavelengths was described in Ref. 1. From Eq. (3), an error of $\pm 20\%$ in G will result in an error of $\pm 22\%$ in $\tau_{0.5}$. Finally, from Eq. (6), the precision in determining the compressed fuel ρR will be better than a factor of 2.

Summary

In summary, the use of krypton doping for diagnosing high-temperature, medium-density implosions has been discussed for two cases: low-opacity lines (achieved with low doping) and high-opacity lines. Using detailed Kr Stark profile calculations, it is found that the profiles of low-opacity lines in the expected density range are dominated by Doppler broadening; they can thus provide a measurement of the ion temperature if spectrometers of spectral resolution $\Delta\lambda/\lambda \geq 1000$ are used. For high-opacity lines, obtained with a higher krypton fill pressure, the measurement of the escape factor can yield the ρR of the compressed fuel. At higher densities, Stark broadening of low-opacity lines becomes important and can provide a measurement of the density, whereas lines of higher opacity can be used to estimate possible mixing.[1] These higher densities will arise in future experiments where high temperatures and high densities will be simultaneously achieved.

REFERENCES

1. Laboratory for Laser Energetics LLE Review **61**, NTIS document No. DOE/SF/19460-58, 1994 (unpublished), p. 1.

2. L. A. Woltz and C. F. Hooper, Jr., Phys. Rev. A **38**, 4766 (1988).

3. R. C. Mancini *et al.*, Comput. Phys. Commun. **63**, 314 (1991).

4. R. D. Cowan, *The Theory of Atomic Structure and Spectra* (University of California Press, Berkeley, CA, 1981).

5. J. C. Kieffer *et al.*, Appl. Opt. **28**, 4333 (1989); B. Yaakobi, T. Boehly, and P. Audebert, Rev. Sci. Instrum. **61**, 1915 (1990).

6. B. Yaakobi, S. Skupsky, R. L. McCrory, C. F. Hooper, H. Deckman, P. Bourke, and J. M. Soures, Phys. Rev. Lett. **44**, 1072 (1980).

7. N. D. Delameter *et al.*, Phys. Rev. A **31**, 2460 (1985).

8. F. E. Irons, J. Quant. Spectrosc. Radiat. Transfer **22**, 1 (1979).

9. J. P. Apruzese, *ibid.* **34**, 447 (1985).

10. C. Chenais-Popovics *et al.*, *ibid.* **36**, 355 (1986).

11. R. C. Mancini, R. F. Joyce, and C. F. Hooper, Jr., J. Phys. B: At. Mol. Phys. **20**, 2975 (1987).

12. H. R. Griem, *Plasma Spectroscopy* (McGraw-Hill, New York, 1964).

Simulations of Diagnostic Emission due to Fuel-Pusher Mixing in Laser-Driven Implosions

It is important to develop diagnostics of the Rayleigh-Taylor instability that occurs during the deceleration phase of inertial-confinement-fusion capsule implosions because this instability is a crucial factor limiting the capsule performance.[1] To simulate the effects of this instability and to assess possible diagnostic techniques, a mix model has been added to the one-dimensional (1-D) hydrocode *LILAC*.[2] This model includes the effects of turbulent mixing on the hydrodynamic motion as well as on the temperature and material-concentration profiles within the plasma. In the work described here, this model is used to simulate time-resolved images of implosions of a gas-filled capsule that is representative of the kind proposed for near-term experiments on the 30-kJ, 60-beam OMEGA laser. In particular, the use of emission from thin chlorine-doped layers in the pusher is considered as a means to track the growth of the mixed region near the fuel-pusher interface. It is shown how the onset of mix-induced emission varies over a series of polymer-shell targets that are identical, except that the additive layer is displaced by different amounts from the fuel-pusher interface in each target. It is also shown that the introduction of an additive layer sufficiently thick to produce adequate diagnostic emission has a minor effect on the implosion performance, compared with the effects of mix itself.

The Rayleigh-Taylor instability is the tendency of adjacent fluid layers to interpenetrate one another when the less dense of the two layers supports the denser layer under a gravitational or inertial force.[3] Under these circumstances, perturbations in their interface grow into buoyant bubbles of the lighter fluid that rise past sinking spikes of the heavier fluid.[4] As the depth of penetration becomes comparable to the lateral scale length of the bubble-spike structure, the interpenetration becomes more turbulent[4] and the state of the two fluids approaches that of a mixture.

This instability appears twice during a capsule implosion. The first occurrence, the acceleration-phase instability, starts at the very beginning of the implosion at the ablation front where the shell is being accelerated inward by the hot and relatively light plasma ablating from the capsule surface. This instability can be seeded by both initial surface imperfections in the shell and nonuniform laser irradiation. The second occurrence, the deceleration-phase instability, begins as the rising pressure in the fuel core decelerates the imploding shell. At this time, the inward radial acceleration reverses, and the instability moves to the inner side of the density peak in the pusher to the fuel-pusher interface, where the hot central fuel mass supports the cooler and denser pusher. Here, the unstable growth of the fuel-pusher interface is seeded by the accumulated distortion that feeds through from the ablation region. As pusher material mixes with the fuel, cooling by dilution causes the nuclear reaction rates to drop. In addition, the dispersal of the fuel into the pusher reduces the areal density of the fuel mass (the fuel-averaged density-radius product, ρR), which is a key measure of how close to ignition the fuel has come. If the pusher contains a substance other than hydrogen, radiative losses will cool the fuel further. If this enhanced radiation loss can be observed either spectroscopically or with imaging, then it can be interpreted as evidence that mix has occurred.

Such a diagnostic represents a logical extension of the technique of using plastic-coated glass targets[5] and multilayer targets[6] in thermal transport experiments to measure the advance of the thermal front in the ablation region. Calculations of the growth of the mix region near the ablation front showed that mixing due to the acceleration-phase instability significantly augments thermal conduction in transporting the laser-driven heat front to the glass substrate layer, which accounted for emission from the glass appearing sooner than expected from simulations based on thermal transport alone.[6]

In adapting this technique to the deceleration-phase instability of the fuel-pusher interface, we consider a series of targets where a thin additive layer is placed at various distances Δr from the inner surface of the pusher (see Fig. 64.18). The characteristic emission from the additive is delayed until the mixed region has grown through the underlying pure-CH polymer to include the additive layer. By measuring the delay
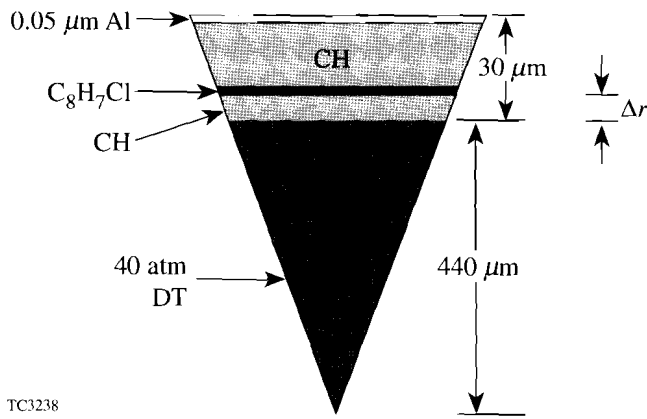
Figure 64.18
Section of the representative spherical capsule that will serve as the example in the calculations to follow. The C_8H_7Cl additive layer is 2-μm thick. It is to be imploded with a square 13.5-TW pulse of 2.3-ns duration.

a diffusive process that transports constituent concentrations and thermal energy within the boundaries of the mix region. These boundaries are the bubble and spike fronts obtained from perturbation mode amplitudes calculated from the 1-D hydrodynamics using a multimode Rayleigh-Taylor model similar to that of Haan.[9] The diffusion coefficient is the product of a velocity derived from the expansion of the mix region and a scale length λ_{mix} characteristic of the mixing motion. At this point in the development of the 1-D mix model, this scale length is a free parameter, but work is now in progress to allow its value to be derived at each time from other physical parameters of the system being simulated. The inclusion of this 1-D mix model within *LILAC* allows for simulations that take into account the cooling effects of radiation and dilution and the associated reduction in the diagnostic emission and the neutron yield. These simulations also allow the hydrodynamics to respond to the moderated density and pressure profiles, as well as to the effects of the modified radiative properties of the mixed fluid.

of the additive emission as a function of the initial position of the additive layer, the trajectory of the bubble surface, the outer boundary of the mixed region, can be inferred.

This technique is also a refinement of a method used in experiments on the Nova laser at the Lawrence Livermore National Laboratory where iodine was added to polymer shells to increase the emissivity of the pusher.[7] In other experiments,[8] chlorine was used as a pusher additive and argon as a fuel additive. The overall degree of mixing was inferred from the intensity of chlorine emission, relative to the intensity of the argon emission, and an average temperature of the mixed additive was obtained from the line ratios of the spectra of the additives. The use of thin additive layers and time-resolved measurements allows the growth of the mix region to be followed in time by associating the arrival of the outer mix-region boundary at the additive-layer radius with the onset of the characteristic additive emission. The idealizations of a distinct mix-region boundary at the bubble front and an abrupt onset of the diagnostic emission are only approximations, but they are useful for understanding the results of the simulations and for anticipating the results of actual experiments.

Mix Modeling in One Dimension

In our spherically symmetric, purely 1-D simulation, the multidimensional bubble-spike structure and the subsequent turbulent structure are not described explicitly, leaving instead a fluid that is completely mixed at the atomic level. The mix model used within the 1-D hydrocode *LILAC* is formulated as

An important consequence of this 1-D approximation is that the interpenetrating fluid elements share the same spherically averaged temperature profile. It is reasonable to expect that thermal conduction equilibrates temperatures rapidly over the short scale lengths of the interpenetrating fluid bubbles, spikes, fingers, and eddies, which will tend to evolve the temperature of the mixing region toward a spherically symmetric temperature profile common to all the constituents. To the extent that this is true, the temperature in the neighborhood of a particular ion of additive material will depend more on its radial coordinate than on information lost by disregarding the nonspherical fluid structure.

A difficulty with the 1-D mix model can occur when the mixed region is optically thick. In reality, or in a multidimensional description, this region could have optically thin spots that would allow radiation to escape that otherwise would not escape. Even a relatively subtle effect of this kind would limit the usefulness of a 1-D model for simulating quantitative line intensities, except when line-absorption effects are negligible or otherwise well understood. Also, emission that is particularly temperature sensitive could be misrepresented if spherical averaging were to smooth out some hot spots. However, the use of a local transport model in 1-D does preserve important elements of realism by evolving and distributing the constituent concentrations in a physically plausible way. This is an improvement over global approximations such as forcing flat concentration profiles throughout the mix region[8] or postulat-

ing analytical forms to interpolate the temperature, density, and concentration profiles between the boundaries of the mixed region. Modeling the mix of thermal energy along with the plasma constituents gives an effective enhancement of thermal transport consistent with the mix model. Also, by incorporating the mix model into the hydrodynamics, the mix-affected plasma profiles and pressure gradient remain consistent with the main hydrodynamic process that is the formation of the compressed core.

Time-Dependent Pusher Emission

The capsule chosen to illustrate the model is shown schematically in Fig. 64.18. It is a 30-μm-thick CH polymer shell (the pusher), 940 μm in diameter, filled with 40 atm of DT. It is driven by a simple, flat-top, 13.5-TW pulse, 2.3 ns in duration. A 2-μm-thick layer of C_8H_7Cl is added to this basic design at a distance Δr from the initial pusher/fuel interface.

For illustrative purposes it is useful to talk of the onset of chlorine emission from this additive layer as a signal of the arrival of the bubble surface at the additive layer. This simplified interpretation is based on the assumption that the additive is heated to an emitting temperature immediately upon contact with the bubble front. However, the mix model used in the simulations makes no such assumption. It takes into account the delay required for the additive and the hot fuel to be transported into a common volume where a sufficient amount of additive can be brought to an emitting temperature so as to produce diagnosable radiation. Another simplification is to describe the mix region as having distinct boundaries. The mix model does employ such boundaries to delineate the mix region, but the actual modifications of the material content, temperature, and density profiles due to mix are obtained from a transport model.

Accepting for now this view that additive emission signals the arrival of the bubble front at the additive layer, Fig. 64.19 illustrates how the onset times of the additive emission can be used to track the trajectory of the bubble surface in a series of shots using capsules that are identical, except that the initial position Δr of the additive layer is varied. This figure shows the trajectories of the DT/CH interface and Lagrangian markers at various Δr's, together with the bounds of the predicted mixing region for two different surface finishes, for the illustrative capsule. The bounds of the mixing region correspond to the bubble and spike trajectories and are obtained as described above from the multimode Rayleigh-Taylor perturbation model adapted from the work of Haan.[9] Superimposed over the layer interface trajectories, they illustrate how the mixed region
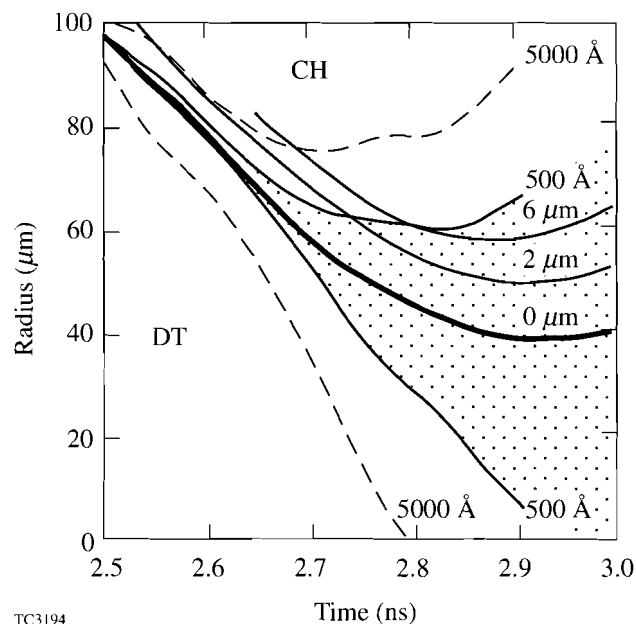
Figure 64.19
Calculated trajectories of the DT/CH interface (heavy line) and Lagrangian markers in the CH at initial distances Δr of 2 μm and 6 μm from this interface. The curves labeled 500 Å and 5000 Å indicate the bounds of the predicted regions of DT-CH mixing for these initial rms surface finishes. The mix region includes both hot core material and relatively cool pusher material. Diagnostic emission from an additive layer in the pusher can occur when it is heated by contact with hot fuel in the mix region.

grows to include both hot core material and additive at times that depend on the initial perturbation and on the initial location of the additive layer. In the calculations for Fig. 64.19, the mix diffusion step has been omitted from the hydrodynamics. The feedback of mix on the hydrodynamics has potentially important effects on the amount of additive emission, but its effect on the trajectories shown here is small.

The heavy curve labeled 0 μm is the trajectory of the decelerating fuel-pusher interface. The zero of the time axis is the time of the start of the laser pulse. The curves labeled 2 μm and 6 μm are trajectories that would have been taken by additive layers if they had been displaced initially by these distances from the inner surface of the shell. The pair of curves labeled 500 Å are the mix-front trajectories calculated assuming an initial rms perturbation amplitude equal to this value whose modal decomposition is of the form $l^{-5/4}$, where l is the spherical mode index. The dashed curve shows the much larger mixed region resulting from a 5000-Å surface perturbation. This rms perturbation amplitude should be comparable to an equivalent surface roughness, but a quantitative relationship

between surface roughness and the perturbation amplitude is not established at this time. Consequently, these results should be regarded as purely illustrative and not indicative of the performance of a capsule made to any given specification. Also, the relationship of this surface perturbation to an equivalent irradiation nonuniformity has not been determined.

The amplitudes of the fuel-pusher perturbation modes are set at the beginning of the shell deceleration to values obtained from the corresponding ablation-region mode amplitudes by applying the attenuation factor $\exp\left(-l\,\Delta r_s/r_a\right)$, mode by mode, where r_a is the radius of the ablation surface and Δr_s is the separation between the ablation surface and the fuel-pusher interface. This is the prescription suggested by Haan[9] for initializing mode amplitudes at a surface whose unstable perturbations are seeded by the instability that has grown at another surface. The form of this coupling factor corresponds to the decaying exponential dependence of the amplitude of a surface-wave eigenfunction on the distance from the perturbed surface. This correspondence is well motivated, but approximate, and requires further study.

For the purposes of illustration, then, the crossing of the trajectory of the bubble front with the trajectory of the additive layer can be taken to give the time when the additive material enters the mixed region. Presumably, the amount of hot fuel in the mixed region at this time has raised the temperature to a level sufficient for the additive to emit. Figure 64.20, which gives the functional dependence of this estimated emission onset time on the additive layer displacement Δr for a series of capsules with identical initial perturbations, shows that this onset time is delayed with more deeply inset additive layers and with smaller initial perturbations, as might be expected. Each curve was obtained from the bubble-front trajectory resulting from the corresponding initial surface perturbation. The points are the times at which this trajectory contacts an additive layer at the indicated initial displacement. Emission-onset timing data from an actual series of shots can be plotted in the same way. This data might not be so complete, however, because the onset time can be expected to become less distinct for additive layers inset by more than a few microns.

While Fig. 64.20 gives useful qualitative information, a mix transport model, such as the one described here, is required to provide more quantitative information. In particular, it can address the important questions of whether one obtains a coincidence of elevated temperature and additive concentration over a large enough volume to produce a signal that is distinct against the background of the polymer emission. This
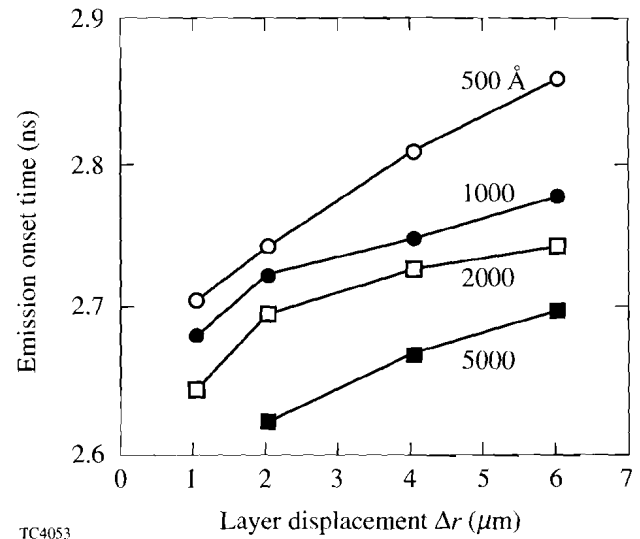

Figure 64.20
Time of onset of emission from the additive layer shown as a function of the initial additive layer displacement Δr from the inside surface of the polymer shell, for various initial surface perturbations.

article concentrates on the detection of additive emission by imaging. It is found that distinct time-dependent additive emission is obtained in the cases simulated here, although not for as full a range of additive layer displacements as is shown in Figs. 64.19 and 64.20.

Mix as a Diffusive Process

Once the growth and extent of the mix region have been obtained, a diffusive transport model is used to simulate the redistribution of the plasma constituents and thermal energy within this region. A natural way to regard mix in 1-D is that each zone in the numerical mesh exchanges a small amount of material with its closest neighbors at each time step. The finite-difference equation that describes this has the form of a diffusion equation. The diffusion coefficient is chosen to be the product of a mix velocity, taken from the velocities of the mix-region boundaries relative to the fluid velocities, and a mixing length. In all but one of the simulations described below, the mixing length is a free parameter. Results are obtained either for a fixed value chosen in advance or for a range of values to show how the outcome of the simulations can vary over the plausible limits of the model. "Flux limitation" is employed as well. The diffusive mass flux is forced to be less than a given multiple F of the free-streaming mass flux given by the product of the mass density and the mix velocity. This feature prevents unphysically large mass fluxes in the presence of large density gradients. The flux-limit parameter F is familiar from other

applications of diffusive transport[10] and is the second free parameter of this model. It is set equal to 2.0 in the calculations presented in this article. Once these two parameters are set, the concentration profiles of the mixed constituents and the mix-transported thermal energy density are then calculated in detail, according to local conditions, rather than from simpler unphysical and/or acausal assumptions such as instantaneous homogeneity within the mix region.

This model resembles the "k-ε" model in its use of diffusive transport to model turbulent transport,[11] but important differences exist. In the model used here, the momentum and kinetic energy of each fluid zone are conserved exactly, but there is no accounting for energy contained in the turbulent motion, in contrast to the k-ε model. Another difference is that this model contains a multimode instability calculation done in parallel with the mix transport, while the k-ε model includes no mode-spectral information. The mix-region model presented here offers the advantage of including the Haan multimode perturbation model with its phenomenology of the nonlinear growth of saturated modes. The spatial-spectral information kept by the multimode model is potentially important in the development of the mix-transport model beyond the version used to obtain the results shown below. For example, preliminary results have been obtained using a mixing scale length that is set equal to the rms perturbation wavelength averaged over the mode spectrum. This utilizes the spatial wavelength information in the perturbation mode spectrum, which is certainly a better strategy than using a fixed length chosen in advance. This derived scale length changes in time as the mode amplitudes themselves change and also as the transverse wavelengths of the individual modes decrease due to the mix region converging with the implosion.

An illustration of the direct effect of mix in 1-D simulations is provided by Fig. 64.21, which shows the spread of the concentration profile of the chlorine additive in the representative capsule shown in Fig. 64.18 for two values of Δr. In both cases the surface mass perturbation is set to 2000 Å with an $l^{-5/4}$ modal decomposition. Figure 64.21(a) shows the case where the initial additive layer is the innermost 2 μm of the pusher, and Fig. 64.21(b) shows the case where the additive layer is inset by 2 μm. The mixing length λ_{mix} is chosen to be 100 μm. In each case the sequence of concentration profiles includes the deceleration phase up to just beyond peak compression. In both cases the additive layers remain substantially undisturbed until after 2.4 ns. The additive layer at the fuel-pusher interface shows a slight preliminary dispersal. The main difference between the two cases occurs just after 2.5 ns, where the additive layer at the fuel-pusher interface begins to disperse about 100 ps before the inset additive layer. By 2.8 ns, the additive profiles have become nearly identical. The difference between the profiles between 2.5 and 2.7 ns suggests that the displacement of the additive layer by 2 μm can result in an effect that can be seen with a temporal resolution around the 100-ps level.

Effects of Mix on Capsule Performance

Simulating the emission from pusher additives requires mix modeling within hydrodynamic simulations to determine to what degree a given amount of additive perturbs the experiment, either by changing the hydrodynamic stability of the implosion or by quenching the diagnostic emission by dilution or by radiative cooling. The perturbative effect of a 2-μm additive layer at the inside surface of the shell can be evaluated from the results shown in Fig. 64.22 for implosions performed using a range of mixing scale lengths λ_{mix}. These simulations

TC3856

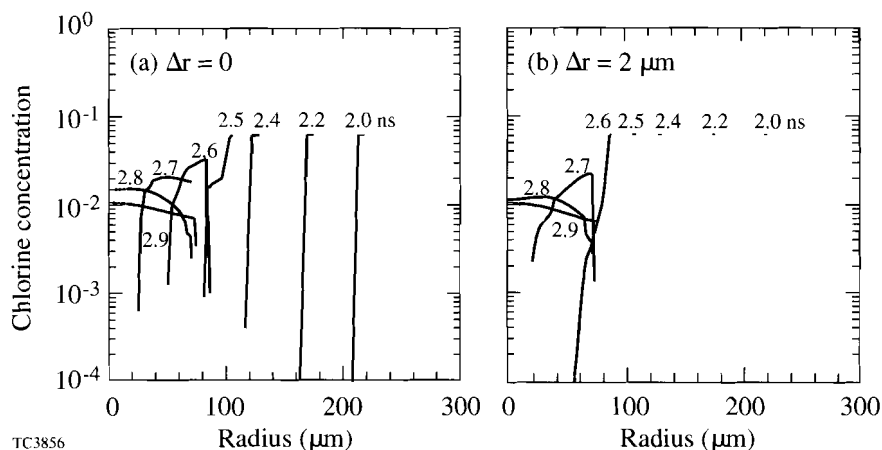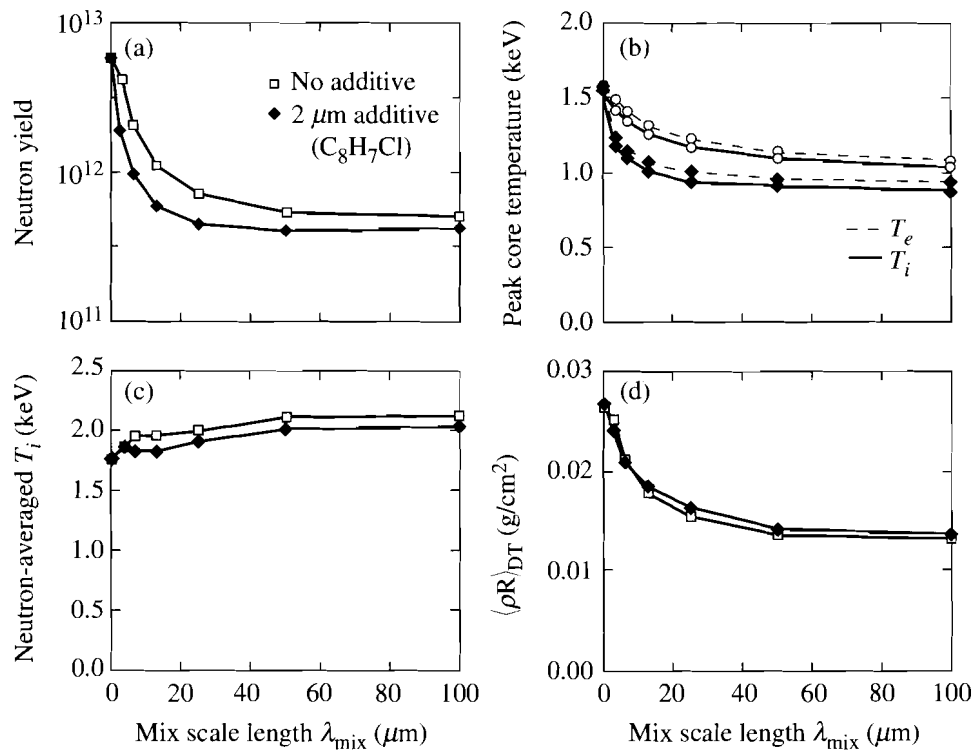Figure 64.21
Sequences of chlorine concentration profiles for (a) $\Delta r = 0$ and (b) $\Delta r = 2$ μm. In each case the chlorine spreads as time increases, but the spreading is delayed, as expected, in the second case. These simulations were performed for an initial perturbation of 2000 Å and with $\lambda_{mix} = 100$ μm.

TC4054,4055,4056,4057

Figure 64.22

Effect of the diagnostic layer (2 μm of C_8H_7Cl) on (a) the neutron yield, (b) the peak electron and ion core temperatures, (c) the neutron-averaged ion temperature, and (d) the DT ρR. Results are plotted as a function of the mix scale-length parameter λ_{mix} for an initial surface perturbation of 2000 Å. The presence of the diagnostic layer is seen to have only a minor effect on the capsule behavior in comparison with the mix.

assume the same initial 2000-Å mass perturbation and $l^{-5/4}$ modal decomposition, which is severe enough to give a good indication of the worst-case effect of mix. The additive layer is placed at the fuel-pusher interface because this produces the maximum effect on the hydrodynamics. The mixing scale length is varied over the range from zero, which gives no mix at all, to 100 μm, where the net mixing rate is determined primarily by the flux limitation. In this case flux limitation restricts the speed of the mixing motion to no greater than 2.0 times the divergence speed of the bubble and spike surfaces, over and above the divergence of the 1-D fluid motion. Figure 64.22 shows that mix has a far greater impact on capsule performance than does the additive layer. Figure 64.22(a) shows that mix reduces the neutron yield substantially, corresponding to a small reduction in the ion temperature [which is shown in Fig. 64.22(b)]. The additional radiative cooling due to the additive is seen in Fig. 64.22(b) as a very slight additional reduction in temperature. Due to the strong dependence of the neutron-production rate on temperature, the effect of the addi-

tive on the total neutron yield is quantitatively significant, but it is clearly of secondary importance in comparison with the much greater effect of the much larger amount of pusher polymer that has been mixed in.

Figures 64.22(c) and 64.22(d) show the ion temperature and the peak value of $\langle \rho R \rangle_{DT}$, the radial integral of the DT mass density, both neutron averaged and thus relevant to nuclear diagnostics. The neutron-averaged ion temperature rises with mix due to the fact that quenching of neutron production within the mix region tends to shut off the yield from the cooler part of the core; this skews the neutron weighting of the temperature average toward the center of the capsule, which is hotter. The neutron-averaged ion temperature is not as sensitive to the presence of the additive as the neutron yield in Fig. 64.22(a). Note that $\langle \rho R \rangle_{DT}$ includes the DT mass only, wherever the mix might have taken it, and does not include the contribution of the pusher material. It is not the areal density of a distinct core. The neutron-averaged fuel areal density $\langle \rho R \rangle_{DT}$ de-

creases with increasing mix, but the additive has an almost negligible effect.

Figure 64.23 shows the neutron-production rates plotted as functions of time for a sequence of simulations with mixing lengths ranging from 0 to 100 μm. As above, this covers the range of mixing lengths from one that would give no mix at all to one that is large enough for the homogenizing effect of mix to be limited primarily by the flux limitation of the diffusion. A 2000-Å mass perturbation and $\Delta r = 0$ have been assumed in all cases. One striking aspect of the results shown in Fig. 64.23 is that the curves remain close to each other up to 2.6 ns where they abruptly diverge. Figure 64.21(a) shows that this is near the time when the entire inner 2 μm of pusher with the chlorine additive has just been drawn into the mix region, which is indicated by the tails on both ends of the concentration profile. By this time the mix region has expanded to include most of the fuel. This abrupt divergence of the neutron-production rates supports the interpretation that yield is effectively quenched by the arrival of pusher material, as was suggested above in explaining the results of Fig. 64.22.
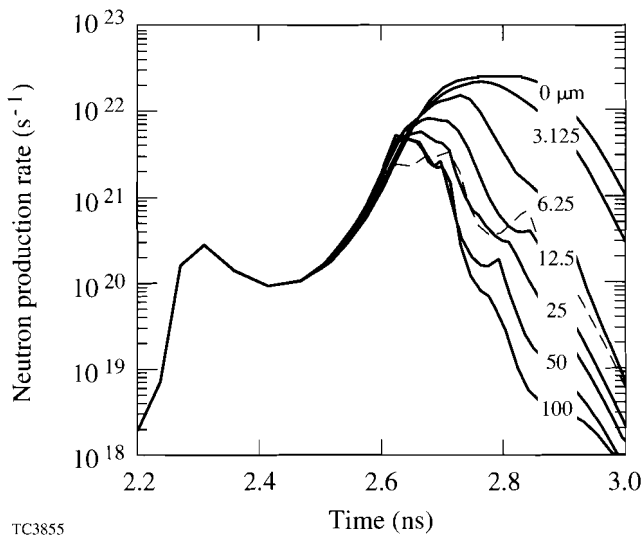

Figure 64.23
Neutron-production rate as a function of time for several values of the mix scale-length parameter λ_{mix}. The initial surface perturbation is 2000 Å. The dashed curve is obtained using a model where λ_{mix} is chosen to be equal to the time-dependent rms spherical wavelength of the perturbation mode spectrum.

The dashed curve in Fig. 64.23 is obtained using a time-dependent mixing length chosen to be equal to the rms spherical wavelength of the perturbation mode spectrum. This represents an attempt to reduce the number of $ad\ hoc$ parameters in

the model. This choice of mixing length also results in an abrupt onset of quenching. The total yield obtained is very close to that obtained from the larger mixing lengths that give very rapid mixing, but later in the deceleration phase the neutron-production rate drops more slowly to values obtained at these later times with much shorter mixing lengths. This reflects the shortening of the average perturbation wavelength due to the spherical convergence of the mixing region, which in this case is a stronger effect than the tendency of the perturbation spectrum to evolve toward longer wavelengths as the shorter-wavelength perturbation modes saturate and fall behind the longer-wavelength modes.

Effects of Mix on Images

Under conditions expected in the fuel-pusher mix, chlorine emission consists mostly of K-shell lines and bound-free continuum. Chlorine is distinctly more emissive than carbon under these conditions since carbon is then almost completely stripped and is seen mostly by its bound-free emission. Imaging implosions with emission in the 3- to 5-keV range isolates the chlorine continuum spectrally and enhances the contrast of emission from the hottest parts of the mixed region against the rest of the image. Chlorine is well suited as a pusher additive for the example described above because its K-shell lines occur just above the energies where the relatively cold pusher would attenuate emission from the center at times near peak compression. Avoidance of this attenuation is obviously important for observing mix with time-resolved spectroscopy.[12] The relative emission strength of chlorine over carbon allows small amounts of additive to be used. The detectability of the chlorine emission is limited by how well it competes with the continuum emission from the carbon, which is the main ingredient of the pusher and thus much more abundant. This is of particular concern when observing line emission from embedded additive layers since the additive lines must be observed against the background of continuum from all the carbon in the overlying layer of pure polymer.

Simulations of framing-camera images are obtained from integrating the equation of radiative transfer along straight-line photon paths through time-dependent emissivity and opacity profiles, taken from the 1-D hydrodynamic simulation, and into a model of a framing camera. The camera forms pinhole images on a photocathode. The images are transferred to a phosphor screen through a multichannel plate, which is triggered by a short electrical pulse propagating along a stripline over the plate. The model includes the camera geometry, the optics of finite pinholes, and a temporal response based on the calculated response of the multichannel plate to the electrical

pulse provided. The gating time is 45 ps, which represents a near-term development goal for this instrument. The intensity units in the plotted images are arbitrary since the camera model does not include information from an absolute calibration, but the relative intensities from frame to frame are consistent in these units. The spectral response of the camera includes that of the camera itself and foil filters of 25 μm of beryllium and 20 μm of titanium to center the net response within a window from about 3 to 5 keV.

Figure 64.24 shows a sequence of five framing-camera images, taken 50 ps apart, of the previously chosen polymer capsule with mix seeded by a 2000-Å exterior mass perturbation. The results from six simulations are superposed. Each curve represents the azimuthally averaged image intensity plotted as a function of radius. A mixing length of 100 μm is assumed. The value of the numeral labeling curves 0, 1, 2, and 4 is the initial displacement, in microns, of the additive layer outward from the inner surface of the pusher. The curve labeled
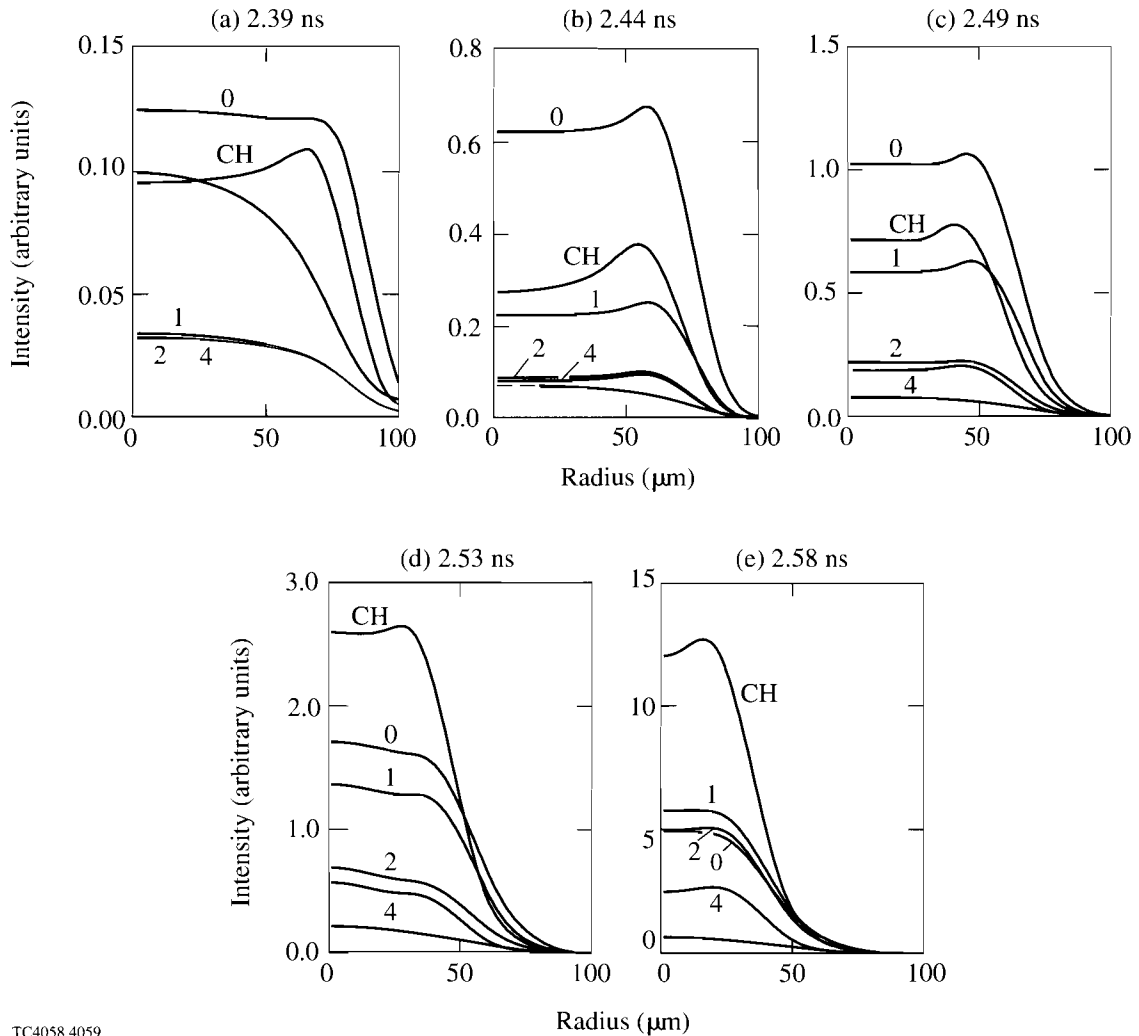
TC4058,4059

Figure 64.24
Simulated framing-camera images in the 3- to 5-keV range at times 45 ps apart ranging from (a) 2.39 ns to (e) 2.58 ns. The curves labeled 0 to 4 are for additive layer displacements of 0 to 4 μm, respectively; the curves labeled CH are for a pure CH pusher (no additive layer), and the dashed curves are for the case of no mix. Except for the dashed curves, the initial surface perturbation is 2000 Å and the mix scale-length parameter λ_{mix} is 100 μm. Note the different intensity scales.

"CH" corresponds to a calculation with no additive layer, and the dashed curve is obtained from a simulation of the case "0," where the additive layer is at the fuel-pusher interface and where no mix takes place.

At the time of the first frame [Fig. 64.24(a)], mixing has already begun. The effect of this is seen in the brightness of image 0 relative to the dashed line, its unmixed counterpart. A comparison of image 0 with image CH, obtained with no additive, shows that the additive results in a brighter image, as is expected, but without limb brightening, in contrast to the distinct limb brightening of the image CH. The intrinsic emissivities of both capsules are, in fact, peaked at their fuel-pusher interfaces, but at this early time there remains enough cool additive surrounding the fuel-pusher mix region of the additive-layer capsule to form an attenuating layer that rounds off the image by a limb-absorption effect. This limb darkening is particularly strong for images 1, 2, and 4, where the entire additive layer is cold and absorbing. The conditions at the fuel-pusher interfaces of these three cases are essentially identical to those of the CH case where there is no additive, and the differences between their images and that of the CH case are almost entirely due to this absorption. The nearly complete indistinguishability of the 1, 2, and 4 curves is evidence that the additive layer has no other effect on the implosion.

At later times curves 1, 2, and 4 brighten, in the expected order, as fuel-pusher mixing overtakes the additive layers successively further from the fuel-pusher interface. For example, from frame (d) to frame (e), curve 2 brightens to become comparable in intensity to curves 0 and 1. This systematic effect of the additive-layer displacement on the time dependence of the additive emission would be worth looking for in an actual experiment. These images tend to become more limb brightened as the additive becomes more emissive than absorbing, but there is a competing effect favoring central emission as well, as is seen in frame (d).

The five frames show that the fuel cores contract by a factor of about 2 for each calculation over the 200 ps shown. Nevertheless, there are subtle differences in their dynamics that are caused by mix. These effects, in combination with rapidly increasing intensities, add a potentially significant bias to the comparison of the overall intensities of any two images at any given instant. Comparing image intensities at points of equal core compression, for example, could give different results. Thus some caution is required in comparing relative intensities in Fig. 64.24. The CH images of the pure polymer capsule in particular appear surprisingly bright, relative to the images of

capsules with additive layers. The pure polymer capsule does, in fact, implode sooner than the additive-layer capsules and is found to reach peak compression about 30 ps earlier. Consequently, if the images were all compared at identical degrees of convergence, rather than at identical points in time, the intensity from the pure polymer capsule would be seen to be much more in line with those of the other images.

Relaxing the flux limitation by increasing the flux-limit parameter allows a greater concentration of chlorine to reach the spike front from the bubble front, and greater limb brightening is obtained. This is what would most likely result from a mix model that instantaneously homogenized all the material within the mix region, which is unphysical, at least from the point of view of the mix transport model used in this work.

Over the entire 200 ps spanned by these images, all the images brighten by nearly two orders of magnitude, except for the unmixed case, which lags far behind. This shows that mix can be expected to have a strong brightening effect on images of polymer-shell implosions, regardless of how they are modified by additive layers.

Conclusions

In conclusion, experiments are proposed to diagnose pusher/fuel mixing in imploding gas-filled capsules using additive layers of chlorinated plastic at various distances from the initial pusher/fuel interface. A mix model has been developed to simulate these experiments. The model includes the self-consistent modifications to the capsule hydrodynamics that result from a time-dependent diffusive treatment of the mix region. These experiments appear promising, based on the present analysis. The proposed diagnostic technique is, of course, compatible with other diagnostics suggested elsewhere, such as detailed line-shape and line-ratio analysis, with or without a fuel additive.

REFERENCES

1. J. Nuckolls, L. Wood, A. Thiessen, and G. Zimmerman, Nature **239**, 139 (1972).

2. Laboratory for Laser Energetics Report No. 16, 1973 (unpublished); Laboratory for Laser Energetics Report No. 36, 1976 (unpublished).

3. Lord Rayleigh, *Scientific Papers* (Cambridge University Press, Cambridge, England, 1900), Vol. II, pp. 200–207; G. I. Taylor, Proc. R. Soc. Lond. A **201**, 192 (1950).

4. F. H. Harlow and J. E. Welch, Phys. Fluids **9**, 842 (1966).

5. J. Delettrez, Can. J. Phys. **64**. 932 (1986) and references cited therein.

6. J. Delettrez, D. K. Bradley, and C. P. Verdon, Phys. Plasmas **1**, 2342 (1994).

7. B. A. Hammel *et al.*, ICF, LLNL Quarterly Report **1**, (1991), pp. 151–156.

8. T. R. Dittrich *et al.*, Phys. Rev. Lett. **73**, 2324 (1994).

9. S. W. Haan, Phys. Rev. A **39**, 5812 (1989).

10. R. C. Malone, R. L. McCrory, and R. L. Morse, Phys. Rev. Lett. **34**. 721 (1975).

11. S. Gauthier and M. Bonnet, Phys. Fluids A **2**, 1685 (1990).

12. R. Epstein, J. A. Delettrez, C. P. Verdon, D. Shvarts, and B. Yaakobi, Bull. Am. Phys. Soc. **39**, 1695 (1994).

Distributed-Phase-Plate Design Using Simulated Annealing Algorithms

Methods of designing phase plates to achieve control of the far-field irradiance distribution for laser-induced plasma experiments have been under study for more than a decade. One important goal of phase-plate design is to generate the desired far-field spatial profile while minimizing wide-angle scattering outside this profile. This article reports a new algorithm that accomplishes this goal.

Many phase-plate designs reported in the literature have used the phase-retrieval algorithm. These designs achieve a good match to the high-order super-Gaussian distribution that is presumed to approximate the ideal far-field spatial profile. However, the resulting phase plates exhibit wide-angle scattering losses due to steep surface slopes near surface vortices and line discontinuities.[1,2] An article in a previous issue of the LLE Review[3] described an improved phase-retrieval procedure that reduces the number of pole discontinuities and thus the energy loss due to scatter. The present article reports a simulated-annealing algorithm that has resulted in a complete elimination of this source of loss.

Using the classical method of phase retrieval, it is not possible to specify arbitrary constraints or to custom design a cost function for a particular application. To achieve lower scatter by using a strictly continuous phase-plate surface, we have investigated simulated annealing because it allows us to invoke specific constraints, to design with arbitrary cost functions, and, potentially, to find the globally optimum solution for a given set of constraints.[4,5] Using simulated annealing we can specify separately the target far-field profile and the cost function. For example, we can design for specific speckle statistics given the constraint of a specified far-field profile. The cost function may be made sufficiently complex to combine with various weights a number of different factors of importance to a given application.

Algorithm

Our implementation of simulated annealing consists of a number of steps. Starting from an initially aberration-free

pupil distribution, a smoothed random wavefront of weak magnitude is constructed and added to the pupil. The far-field irradiance is then calculated by diffraction propagation using fast Fourier transform algorithms, and its azimuthal average $f(r)$ is compared with the desired far-field super-Gaussian irradiance envelope

$$I(r) = e^{-2(r/r_0)^M},\qquad(1)$$

where M is the super-Gaussian order, r is the transverse radius in the far field, and r_0 is the characteristic radius of the far-field distribution. A simple cost function S is evaluated from $f(r)$ and $I(r)$ as

$$S = \int_0^\infty [f(r) - I(r)]^2 \, 2\pi r \, dr.\qquad(2)$$

Cost functions calculated in rectangular coordinates tend to over-constrain the design by reducing the speckle. Use of the azimuthal-average profile as in Eq. (2) provides noise averaging of the quasi-speckle pattern in the far field. Various perturbations of the phase plate are then tried, with the cost function reevaluated each time. If the cost function is lower, the perturbation is accepted and the modified phase plate becomes the basis of further trials. If the cost function is higher than that of the previous cycle, the trial perturbation will be accepted if a random number X, which is uniformly distributed between 0 and 1, is less than the simulated annealing probability p, defined as

$$p = e^{-\Delta S/T},\qquad(3)$$

where ΔS is the change in the cost function due to the perturbation and T is a parameter known as the simulated annealing temperature, the analog of the temperature of an annealing oven. Since the initial, aberration-free pupil matches the target profile quite poorly, the initial cost function is high and ΔS is

quite high also; i.e., relatively small perturbations of the phase plate result in relatively large changes in S. The temperature T is lowered over a number of iterations and serves to control the "cooling" rate of the process. A premise of the theory of simulated annealing is that if the process is cooled sufficiently slowly, local minima will be overcome, resulting in convergence to the global optimum.[4,5]

In our illustrative calculations, the diameter of the pupil was 14 cm, and the desired far-field distribution was a super-Gaussian of eighth order and 700-μm diameter. For a laser wavelength of 0.3511 μm there are about 150 speckles across this diameter. The far-field distribution was sampled using an array of 1024×1024 points. Although the beamlines of the OMEGA laser are 28 cm in diameter, the smaller 14-cm diameter was used to reduce computation time.

To find a continuous-surface phase plate that best achieves the desired far-field irradiance envelope, the trial perturbation to the phase plate consists of smoothed random surfaces guaranteeing that the sum of the accepted perturbations will also be strictly continuous. Each cycle of the simulated annealing process requires a unique surface perturbation. Smoothed random surface perturbations are constructed by taking a two-dimensional field of real random numbers and smoothing and scaling this distribution to obtain the desired variance and autocorrelation width. These surface perturbations are made unique by choosing a different random seed for each cycle. We have used an autocorrelation diameter of 0.8 cm, giving about 17.5 autocorrelation diameters over the 14-cm pupil width and a wavefront error of standard deviation 0.03 waves. Once the perturbation wavefront is formed, it is applied to the complex amplitude distribution in the pupil, the far-field distribution is calculated, and the change in cost function is computed.

Simulated annealing is well known to require extensive computational time. The difficulty of designing phase plates may be characterized by the size of a square computer array (represented as $N \times N$) needed to represent the phase plate. The number of distinct optical modes scales approximately as N^2, and the time per calculation step also scales as N^2. The largest array reported in the literature that has been used for phase-plate design was 128×128.[6] For the calculations described in this article, it was necessary to use arrays of 1024×1024, leading to an increase in calculation time of nearly four orders of magnitude when compared with studies with the array size 128×128.

The literature contains various prescriptions for cooling schedules to achieve optimum or near-optimum performance in a minimum time.[7–9] In most cases the cooling schedules are, at least in part, determined heuristically by numerical experiments for the particular type of problem of interest to the respective authors. To determine the feasibility of the simulated-annealing technique for our application, which includes a very large number of optical modes, we started with a purely cooling or quenching phase (distinct from simulated annealing) in which the temperature T was set to zero; i.e., no reversal steps were allowed. Starting from an unaberrated pupil, we found the process converged in about 2,000 cycles. The minimized cost function resulting from this calculation (S_1) established a benchmark with which to compare the subsequent simulated annealing procedure. We then set the temperature T so that the cost function rose to approximately four to five times S_1 and then cooled exponentially with a time constant of 1,500 cycles for the next 8,000 cycles. This second phase of the procedure is true simulated annealing since reversal steps are allowed, according to the temperature and current cost function. At the end of the simulated annealing phase, the cost function was reduced from its value S_1 at the end of the quenching phase by about a factor of 3. This calculation took about 120 h of CPU time on the Cray YMP-2 at LLE.

Figures 64.25 and 64.26, respectively, show the azimuthally averaged far-field profile for phase plates designed by phase retrieval and simulated annealing. Both designs were done for the same super-Gaussian profile with $M = 8$. Although the simulated annealing design was restricted to a continuous phase-plate surface, it achieved a much better fit to the desired super-Gaussian shape. The phase-retrieval design was well converged in about ten cycles, while the simulated-annealing design required 10,000 cycles. It is possible that other cooling schedules would give faster convergence and lower asymptotic cost functions.

The continuous-surface design has the advantage that it is free of steep surface slopes and discontinuities, resulting in low wide-angle scattering—an advantage not built into the cost function. The effect of wide-angle scattering is seen in Fig. 64.25 by the very slow decay at large radii, in contrast to Fig. 64.26, which shows rapid decay toward zero irradiance at large radii. In practice, the phase-retrieval design would produce more wide-angle scattering than shown in Fig. 64.25. This is because this design leads to steep surface slopes in the vicinity of surface vortices and 2π line discontinuities, which result in about 5%–10% wide-angle scattering. The effect of
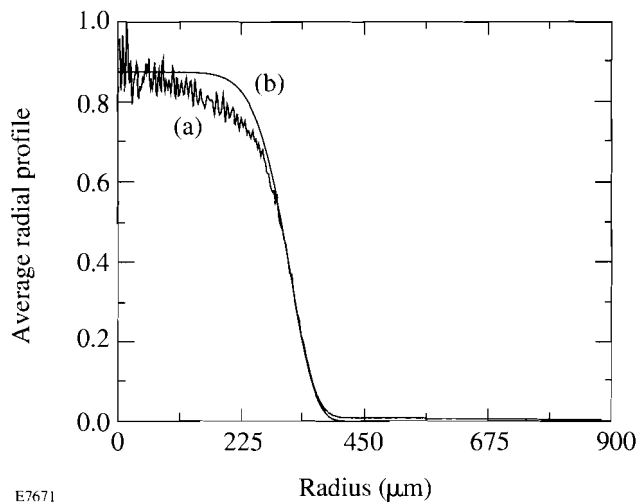
E7671

Figure 64.25
Azimuthal average of the far-field irradiance [curve (a)] due to a phase plate designed by the phase-retrieval algorithm, using the parameters defined in the text. The smooth line [curve (b)] is the ideal eighth-order super-Gaussian profile. The azimuthal average provides considerable smoothing of the data, particularly at the larger values of radius. The phase-retrieval solution shows shoulder droop and a rather slow decay to zero at large radius because of wide-angle scattering from steep surface slopes.
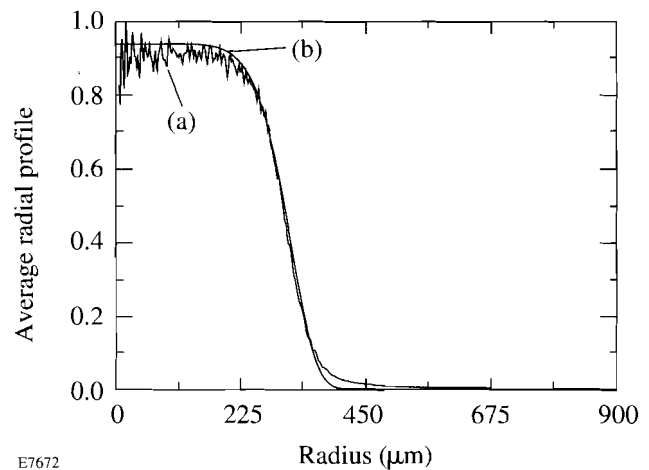

E7672

Figure 64.26
Azimuthal average of the far-field irradiance [curve (a)] due to a phase plate designed by the simulated-annealing algorithm. The conditions are the same as for Fig. 64.25, with curve (b) again the ideal profile. The shoulder of curve (a) is considerably more square than for phase retrieval, and the decay to zero is more rapid, indicating little wide-angle scattering because there are no steep surface slopes.

the line discontinuities does not appear in the calculation because the width of the discontinuities is effectively zero, but some finite width will inevitably be present in the manufactured phase plate.

Scans in two orthogonal directions of the target-plane irradiation profile from phase plates generated using the simulated-annealing algorithm are shown in Fig. 64.27. Unlike Figs. 64.25 and 64.26, no azimuthal averaging has taken place. The large (100% rms) modulations seen are characteristic of far-field phase-plate profiles. The small amount of energy loss outside a diameter of 800 μm is evident.

Overlapping Laser Beams

Flat-foil Rayleigh-Taylor instability experiments require a large number of overlapping laser beams to supply the desired irradiance and uniformity. In particular, the lower-order modes of the irradiance pattern must be minimized to allow for uniform foil acceleration and a careful study of the instabilities associated with high-order modes. There are two primary approaches to obtaining a uniform focal plane envelope from a hexagonal set of six beams from the OMEGA system. The first approach involves using the current OMEGA phase plates, which produce weak super-Gaussian profiles, and offsetting the beams in the target plane by an amount chosen to optimize
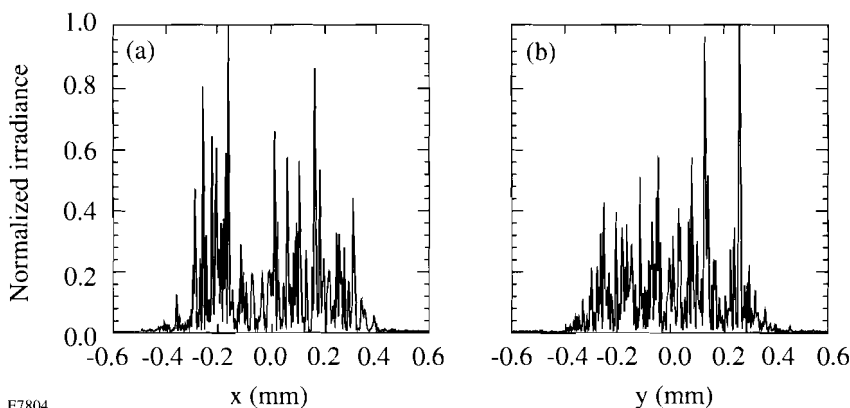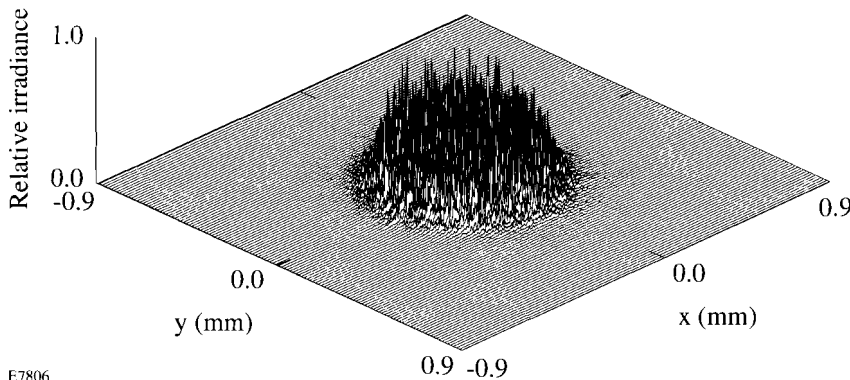

E7804

Figure 64.27
Target-plane irradiance profiles resulting from the simulated-annealing algorithm, (a) vertical and (b) horizontal, showing the high modulation speckle that is characteristic of phase converting a laser beam to over 100 times its intrinsic diffraction limit.

the flatness of the envelope. This method represents a compromise between unwanted modulation, energy loss, and envelope uniformity. The second method involves phase converting the laser beams to produce super-Gaussian beam profiles. This method is preferred because it leads to greater energy efficiency and a larger spatial region of uniform irradiation.
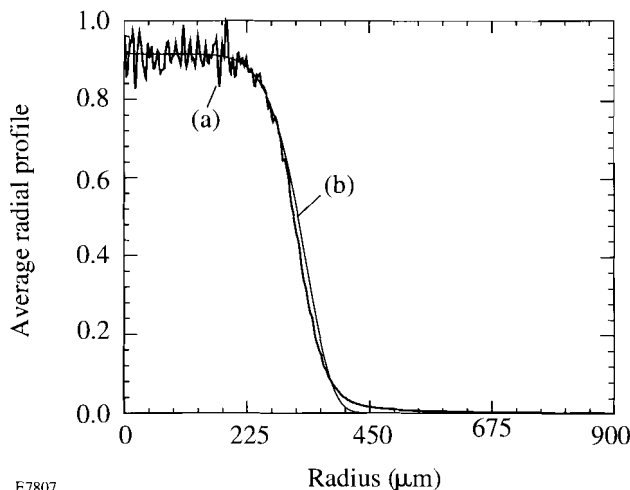
The two-dimensional irradiance pattern for six overlapping laser beams, each phase converted with a super-Gaussian phase plate designed by the simulated-annealing algorithm, is shown in Fig. 64.28. In this case the six beams have the same pointing, resulting in a smaller irradiated region than that produced by offsetting the beams radially from the center of the target. This plot shows the time-instantaneous speckle modulation, which is reduced from 100% to 40% due to the uncorrelated (intensity) addition of the six laser beams. The irradiated region is also seen to be circular, as desired. The encircled energy within an 800-μm spot is 97% for this design.

The azimuthally averaged profile of this irradiance distribution is shown as curve (a) in Fig. 64.29. Curve (b) is an eighth-order super-Gaussian profile, which is nearly the same as each individual beam envelope but a little wider because the beams irradiate the target at an angle of incidence of ~20°. Figure 64.30 shows vertical and horizontal cross sections of the six-beam irradiance on target, without azimuthal averaging. Comparing with Fig. 64.27, the modulation of the speckle is reduced from 100% to 40% due to the $\sqrt{6}$ statistical dependence. A certain amount of energy is lost in the wings of the irradiance distribution. Given that the most useful portion of the irradiance distribution is the flat portion in the center, there is a premium on producing the flattest individual profiles possible. These profiles should remain flat under many realizations of the laser-beam phase error. The needs of stability experiments thus provide an impetus for continued phase-plate design at LLE.

E7806

Figure 64.28
Target-plane irradiance pattern for six beams overlapped and focused onto a flat target, each beam phase converted with a super-Gaussian phase plate. The six beams form a hexagonal subset of the 60 OMEGA beams. For flat target irradiation, the speckle modulation is decreased by the square root of the number of overlapped laser beams.

E7807

Figure 64.29
Azimuthally averaged profile of the two-dimensional irradiation pattern of Fig. 64.28. It is found that 97% of the energy is contained within an 800-μm-diameter circle. The 500-μm-diameter flat region can be extended by pointing the six beams away from the center of the target.
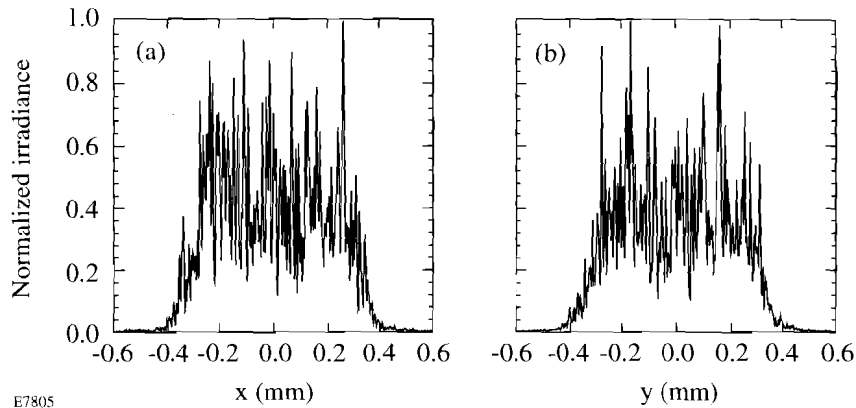
Figure 64.30
Target-plane irradiance profiles, (a) vertical and (b) horizontal, showing a reduction in speckle modulation compared with Fig. 64.27. This is characteristic of overlapping phase-converted laser beams. The contrast of the modulation is reduced from 100% to 40%, which is the expected $\sqrt{6}$ improvement in the time-instantaneous uniformity.

E7805

Summary

A simulated annealing algorithm has been developed to design distributed phase plates that produce super-Gaussian irradiance profiles. This approach uses a strictly continuous surface relief that minimizes wide-angle scattering. Phase plates produced using this algorithm perform better than those produced using the previous phase-retrieval algorithm, which suffer from steep surface slopes and line discontinuities. The new algorithm also allows great flexibility in defining the cost function and constraints to meet the requirements of the target experiments to be performed.

Super-Gaussian phase plates can be fabricated and used to conduct experiments involving multiple overlapping beams. This is important for studies of the Rayleigh-Taylor instability on flat targets. In addition to enhancing the energy efficiency, the simulated-annealing technique offers the capability of controlling the power spectrum of the individual beams used to irradiate targets.

Future work will involve reducing the computation time for the algorithm, decreasing the sensitivity of the phase-plate performance to the laser-beam phase errors, and gaining greater control of the power spectrum placed on target.

ACKNOWLEDGMENT

REFERENCES

1. S. N. Dixit et al., Opt. Lett. 19, 417 (1994).

2. Y. Lin, T. J. Kessler, and G. N. Lawrence, Opt. Lett. 20, 764 (1995).

3. Laboratory for Laser Energetics LLE Review 63, NTIS document No. DOE/SF/19460-91, 1995 (unpublished), p. 126.

4. S. Kirkpatrick, C. D. Gelatt, Jr., and M. P. Vecchi, Science 220, 671 (1983).

5. S. Kirkpatrick, J. Stat. Phys. 34, 975 (1984).

6. S. Yin, M. Lu, C. Chen, F. T. S. Yu, T. D. Hudson, and D. K. McMillen, Opt. Lett. 20, 1409 (1995).

7. H. Szu and R. Hartley, Phys. Lett. A 122, 157 (1987).

8. N. Yoshikawa and T. Yatagai, Appl. Opt. 33, 863 (1994).

9. K. Ergenzinger, K. H. Hoffman, and P. Salamon, J. Appl. Phys. 77, 5501 (1995).

# Self-Interference Patterns and Their Application to Target Characterization

The uniformity requirements of direct-drive targets are stringent. The requirements on both sphericity and wall thickness uniformity are of the order of less than 1%. In the past, dual-beam interference microscopy has been used at LLE to characterize the wall thickness and uniformity of transparent targets.[1] With this technique, an interference pattern is formed between one beam that passes through the target and a second beam, split off from the first, that passes around the target. By comparison with computer-generated templates, these interference patterns can yield the wall thickness and its uniformity to a high degree of accuracy.[2]

This article describes an alternative interferometric technique that is simpler to use and that provides a rapid characterization of both the wall thickness and the uniformity of single-shell targets. These are typically polystyrene (CH) shells, which are selected prior to being coated with layers of various materials and/or filled with D_2, DT, or some other desired gas. These shells have the remarkable property that, when irradiated with a spatially incoherent, narrow-bandwidth light source and viewed using only a compound microscope, they display self-interference patterns (SIP's) such as the one shown in Fig. 64.31. These patterns are distinct concentric fringes when the target is uniform, but faint, distorted, or discontinuous fringes form when the target is nonuniform. Previously, SIP's have not been used because they are clearly observed only in targets of very high quality, with uniformity typically better than 1%.

This technique is currently being used for the preliminary selection of polystyrene shells typically of 800- to 1000-μm diameter and 5- to 12-μm wall thickness. The fringe locations have been modeled using ray tracing and agree well with actual measurements of well-characterized shells. Shells can be selected with the wall thickness known to ± 0.5 μm and with uniformity better than 0.05 μm.

Origin of the Self-Interference Pattern

SIP formation results from multiple reflections of rays within the shell walls. The three relevant beam paths are
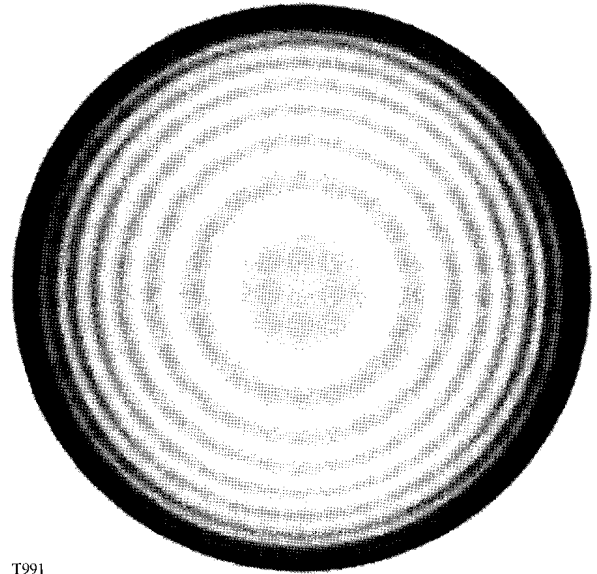
T991

Figure 64.31
A compound-microscope image of a self-interference pattern produced by a symmetric capsule when illuminated with narrow-bandwidth light. The polystyrene (CH) capsule has an 850-μm diameter and a 7-μm thickness.

illustrated in Fig. 64.32. Beam 1 passes straight through the shell, beam 2 undergoes two reflections on the input side, and beam 3 undergoes two reflections on the output side. For a perfect shell, the emerging wavefronts of beams 2 and 3 are virtually identical, so they combine coherently and interfere with the wavefront of beam 1 to form the SIP. For an imperfect shell, in which the input and output thicknesses are different, a single SIP is not formed, but one observes a combination of two SIP's, one corresponding to the input side, (beams 1 and 2 interfering) and the other to the output side (beams 1 and 3).

In Fig. 64.32, all rays are shown backprojected (with dashed lines) to the point on the object plane ($z = 0$) from which they appear to come. Exact ray-tracing calculations show that a ray incident at a height r_i appears to come from a height r_a in the object plane where the difference between r_i and r_a is negligi-
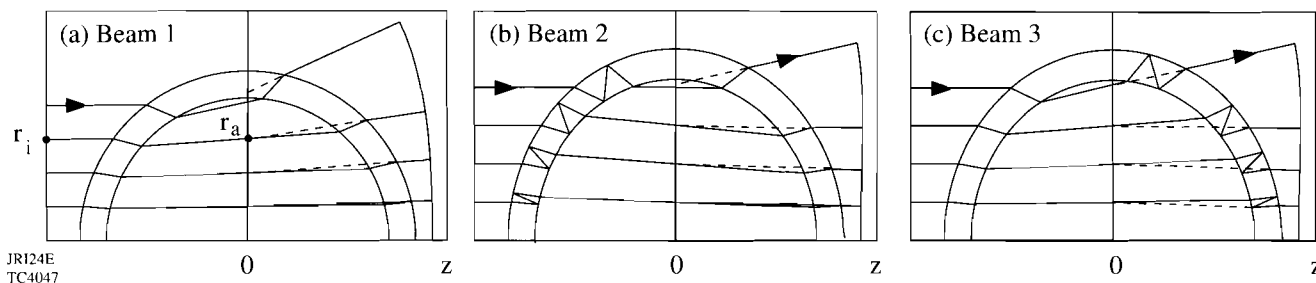
Figure 64.32

Ray paths through the target of (a) beam 1, (b) beam 2, and (c) beam 3. In each case the rays enter from the left, the emerging wavefront is drawn on the right, and the emerging rays are backprojected (dashed lines) to their apparent origin in the object plane ($z = 0$). For a perfect target, wavefronts 2 and 3 are virtually identical, add coherently, and form the self-interference pattern (SIP) through combination with wavefront 1.

bly small (typically less than 0.1 μm except very close to the edge of the target) for each of the three beam paths. This is true only for the object plane $z = 0$. Since the source is spatially incoherent, two rays can interfere only if they originate from the same incident ray. Thus, the only object plane that permits the SIP formation is the midplane $z = 0$. In this sense the fringes can be described as being localized in this plane. In contrast, if the illumination was spatially coherent as in the dual-beam interferometry technique described in Ref. 2, interference fringes could be obtained for any object plane.

For a spherically symmetric target, the locations of the interference fringes may be calculated by plotting the optical path difference OPD_2–OPD_1 between beams 2 and 1 as a function of apparent radius r_a in the object plane (see Fig. 64.33). [OPD_i is defined as the optical path difference (in

centimeters) between a ray of beam i ($i = 1$–3) and a reference ray passing through vacuum, but in Fig. 64.33 it is plotted in waves.] In this example, six bright fringes will be seen with optical path differences ranging from 29 to 24 waves, and the loci of greatest intensity in an interferogram can be simply constructed by drawing circles at the corresponding radii. For targets with nonuniformities in the (x,y) plane, i.e., targets that are not rotationally symmetric about the z axis, interferograms can be formed by tracing a grid of rays through the target and drawing a contour plot of the optical path difference with the contour levels chosen to be integer numbers of waves.[3]

In place of Fig. 64.33, the "universal curves" of Fig. 64.34 can be used to predict the behavior of all perfectly uniform targets of interest. In this figure, the optical path differences OPD_1 and OPD_2, and the difference OPD_2–OPD_1, are all
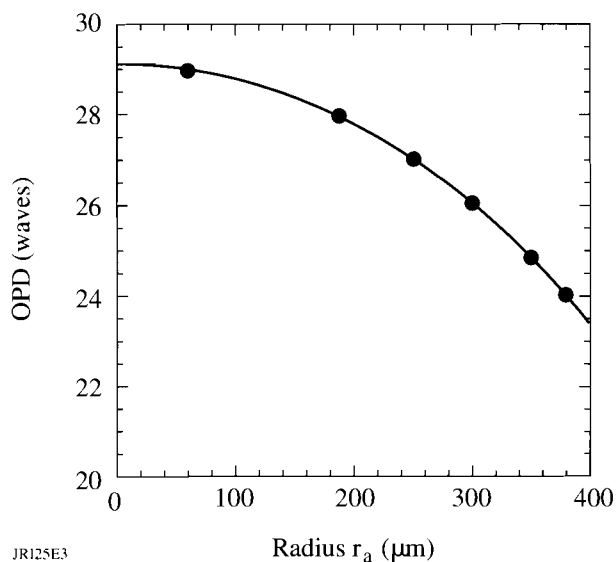
Figure 64.33

The optical path difference (OPD_2–OPD_1) between beam 2 and beam 1 for a representative CH target with an 850-μm outer diameter, a 5-μm thickness, and a refractive index at 546 nm of 1.59. The abscissa is the apparent radius r_a in the object plane (see Fig. 64.32), which is almost identical to the incident radius r_i. The solid points correspond to integer values of optical path difference and thus give the radii of the centers of the bright fringes.
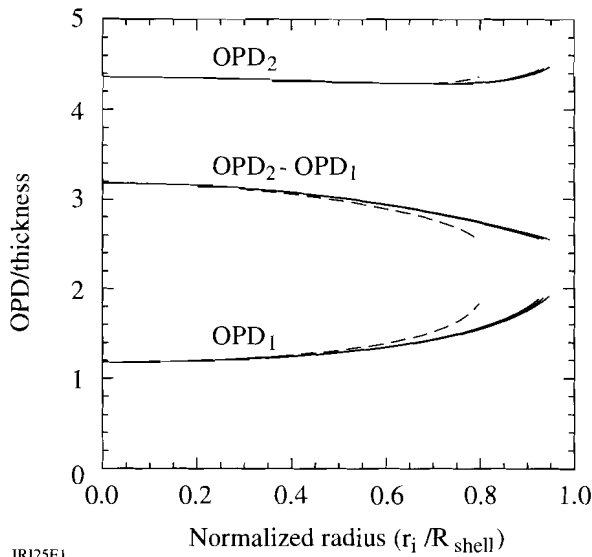
Figure 64.34
Universal curves governing the formation of the self-interference pattern. By plotting the OPD divided by the shell thickness t on the vertical axis and the normalized radius (r_i/R_{shell}) on the horizontal axis, the three quantities OPD_1/t, OPD_2/t, and $OPD_2 - OPD_1/t$ are virtually independent of shell diameter and thickness. The curves shown here are for four shells with outer diameters ranging from 250 to 1500 μm and thicknesses ranging from 2 to 20 μm. The dashed curves correspond to a 250-μm diameter and a 20-μm thickness.

JR125E1
TC4049

plotted against the normalized radius r_i/R_{shell}, where R_{shell} is the average of the inner and outer shell radii. (Similar results are obtained by normalizing to either the inner or the outer radius.) Graphs are superposed for CH targets with outer diameter d = 250 to 1500 μm and thickness t = 2 to 20 μm; specifically, the four extreme combinations are included. All curves are virtually identical except for the low-aspect-ratio combination (d = 250 μm, t = 20 μm), which is not of current interest for experiments on OMEGA.

The values of OPD for rays passing through the center of a perfect target with respect to parallel rays passing external to the target are given by

$$OPD_1 = 2t(n-1), \tag{1}$$

$$OPD_2 = OPD_3 = 4tn - 2t, \tag{2}$$

$$OPD_2 - OPD_1 = 2tn. \tag{3}$$

For example, for n = 1.59 and a wavelength λ = 546 nm, as used throughout this article, the difference in $(OPD_2 - OPD_1)/t$ between the center and the edge is $\Delta(OPD_2 - OPD_1)/t = 0.62$. (The edge is understood to correspond to 95% of the inner-shell radius, i.e., approaching the last ray that will be transmitted through the target.) Thus, if N bright fringes are counted, $\Delta(OPD_2 - OPD_1) \approx N\lambda$ and

$$t \approx N\lambda/0.62 = 0.88 \, N \; \mu m. \tag{4}$$

The accuracy of Eq. (4) is limited by the accuracy with which $\Delta(OPD_2 - OPD_1)$ can be estimated by counting fringes. The method will work as long as the time difference between interfering rays $[(OPD_2 - OPD_1)/c$, where c is the speed of light] is less than the coherence time of the source. For the low-pressure mercury vapor source[4] used in the work reported here, this criterion is satisfied for wall thicknesses $t \leq 15 \, \mu$m.

Ray trajectories have been calculated using both exact ray tracing and a paraxial approximation that includes third-order spherical aberration. The paraxial approximation does not accurately predict the wavefront near the edge of the target, where higher-order spherical aberration is present. However, the error incurred is approximately equal in each of wavefronts 1, 2, and 3. Thus, $\Delta(OPD_2 - OPD_1)$ and $\Delta(OPD_3 - OPD_1)$ are nearly identical for the paraxial and exact ray-tracing treatments, and results obtained by the two methods agree closely.

One notable property of the SIP is its sensitivity to t. For n = 1.59, the quantity detected is $OPD_2 - OPD_1 = 3.2t$ [from Eq. (3)] compared with $OPD_1 = 1.2t$ [from Eq. (1)] as would apply to conventional two-beam interferometry. This method is thus roughly three times more sensitive to changes in target thickness.

Another property of the SIP is that for very small differences between t_L and t_R, the thicknesses on the left and right of the target in Fig. 64.32, respectively, a single interferogram is not formed. For a half-wave difference in the OPD along the

axis, enough to destroy the SIP, the necessary thickness difference is given by

$$2t_L n - 2t_R n = 0.5 \ \lambda$$

or

$$t_L - t_R = 0.086 \ \mu m, \tag{5}$$

corresponding to a 1.2% peak-to-valley thickness variation for a typical 7-μm shell. Targets displaying a distinct SIP have a much better uniformity than this.

Some examples of calculated SIP's are given in Figs. 64.35–64.37. Figure 64.35 shows interferograms of three targets with various wall thicknesses, from which Eq. (4) can be verified. Figure 64.35(b) matches the experimental interferogram of Fig. 64.31 very well. Figure 64.36 shows interferograms of three targets with slightly different wall thicknesses t, to show the sensitivity of the SIP to t as alluded to above. The OPD through the center changes by 0.29 waves for each 0.05-μm change in thickness. Each change is clearly distinguishable, especially if the location of the first or second clear fringe is measured. Finally, Fig. 64.37 shows a combination of two SIP's with a 1% nonuniformity. The nonuniformity is directed along the z direction [Fig. 64.37(a)], at 45° to the y and z directions [Fig. 64.37(b)], and along the y direction [Fig. 64.37(c)]. In each case the heavy and light lines indicate

the two SIP's; in each of Fig. 64.37(a) and Fig. 64.37(b) a distinct SIP would not be seen in practice, so that the nonconcentricity would be easily detected. In Fig. 64.37(c), where the defect is aligned perpendicular to the viewing direction, an up-down shift can be observed in the calculated fringe pattern but would probably not be readily observed in practice. In Fig. 64.37(c) the two SIP's add coherently as the two thicknesses t_L and t_R are equal.

Actual target imperfections rarely match the simplified imperfections shown in Fig. 64.37. An example of an imperfect target is shown in Fig. 64.38. The fringes on the bottom are not too different from those of Fig. 64.31, but extra fringes are observed near the top where, clearly, the target contains a region of excessive thickness. There also appears to be some moiré beating in this area between the two SIP's, one of which is stronger because the microscope is focused closer to its plane of localization.

It does not require a large deviation from spherical symmetry for the two SIP's to not combine coherently. When the apparent positions r_a in the object plane of the two rays associated with beam 2 and beam 3 (see Fig. 64.32) differ by the spatial coherence length of the light source imaged onto this plane, coherence is lost. An alternative and more general approach is to consider every incident ray, including rays other

JRI25E
TC4050
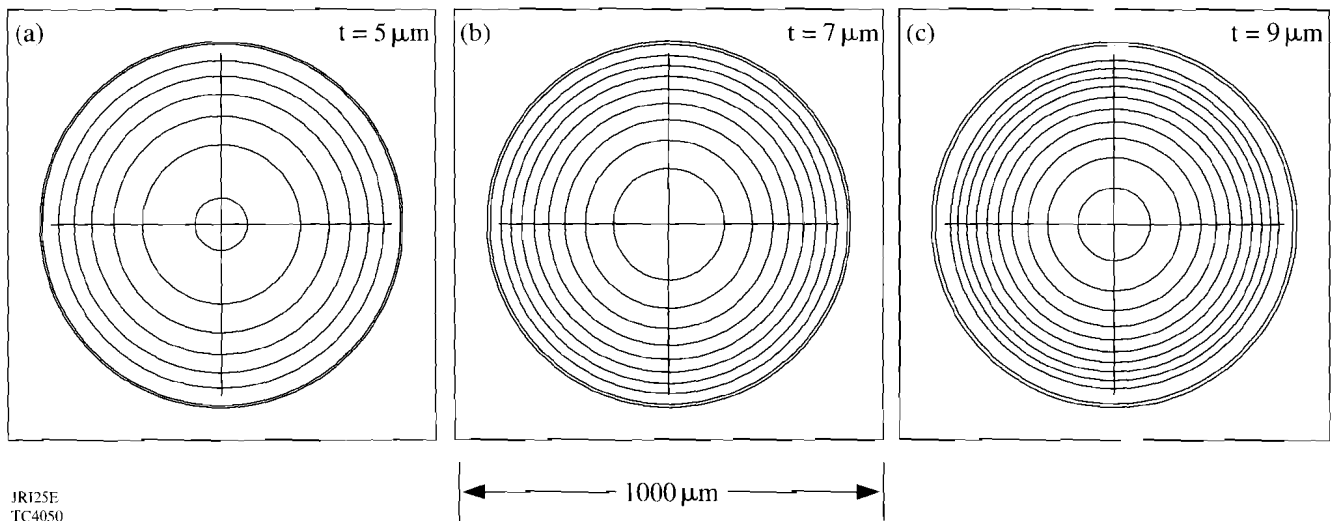
Figure 64.35

Calculated SIP's for three perfectly symmetric polystyrene targets, all with an outer diameter of 850 μm, but with thicknesses t ranging from 5 to 9 μm. The outer circles indicate the edge of the target and the other circles are interference fringes. The SIP for $t = 5$ μm corresponds to Fig. 64.33 and that for $t = 7$ μm corresponds to Fig. 64.31. The target thickness in microns can be estimated by multiplying the number of bright fringes by 0.88.
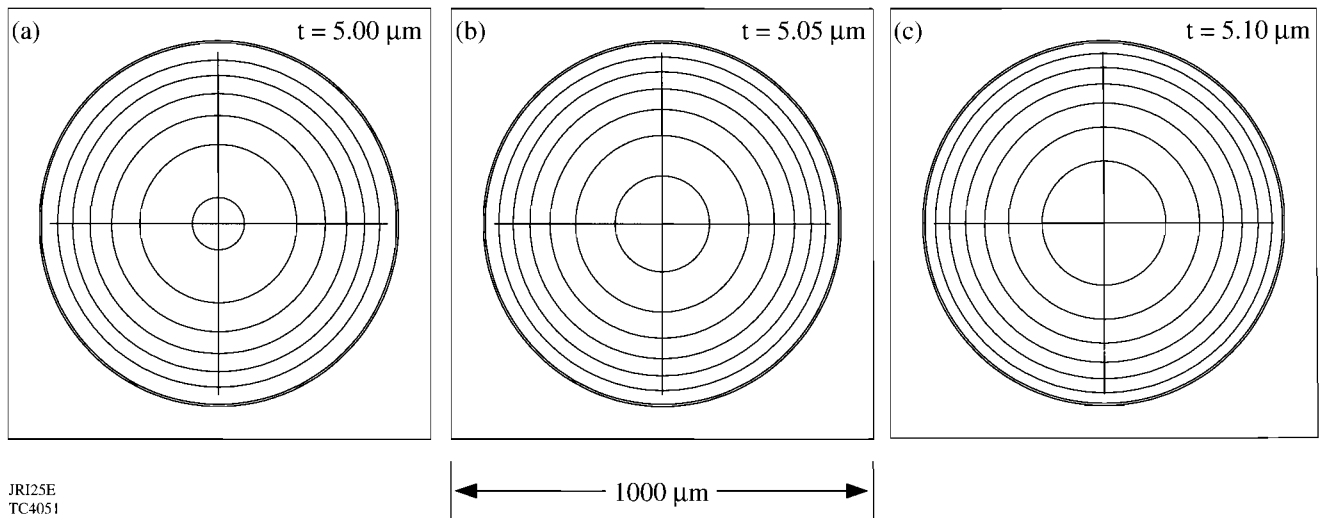
Figure 64.36

Calculated SIP's for three polystyrene targets with slightly different wall thicknesses. Thickness differences as small as 0.05 μm can be detected if attention is paid to the location of the inner fringes.
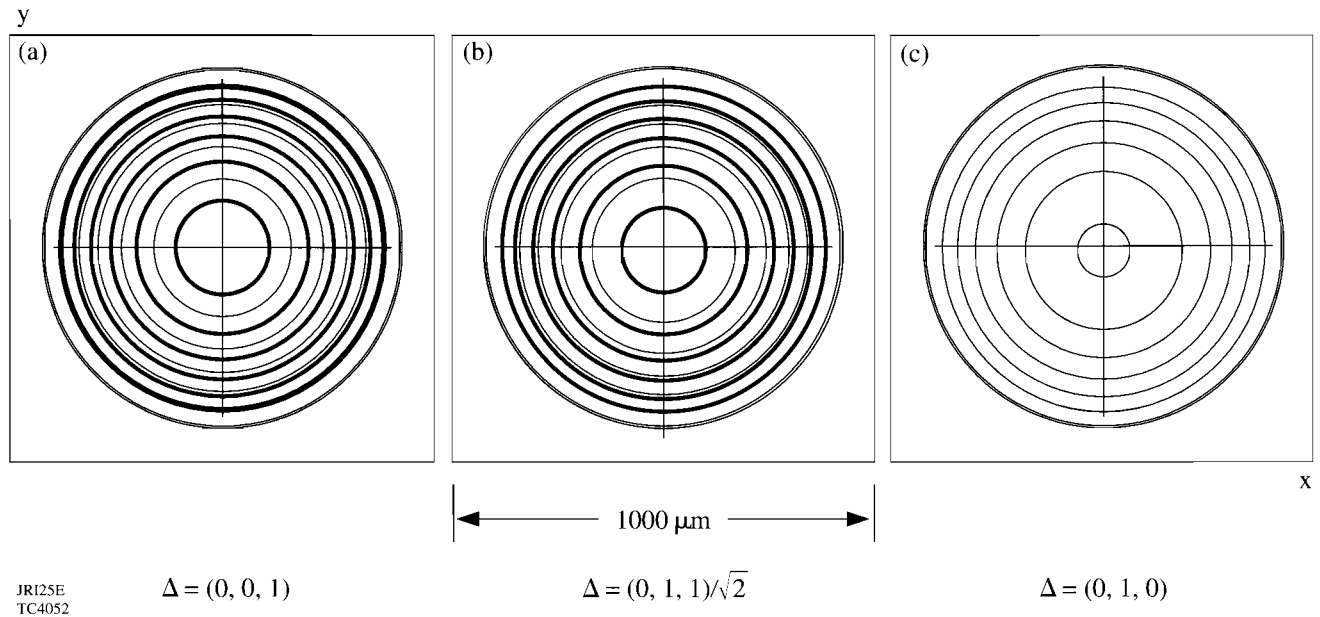
Figure 64.37

Calculated SIP's formed by interference between beams 1 and 2 (light lines) and between beams 1 and 3 (heavy lines) for a polystyrene target with a 1% thickness nonuniformity for three different orientations of the nonuniformity given by the unit vectors Δ. (The inner surface is spherical but shifted 0.05 μm in the direction of Δ.) In case (a) the two SIP's are out of phase by a half-wave in the center, so that no distinct interference pattern would be seen in practice. Thus, the existence of a distinct SIP indicates a target with better than 0.05-μm thickness uniformity.

than the parallel set shown in Fig. 64.32, as independent due to the spatially incoherent nature of the source. For each incident ray there are three emerging rays, corresponding to beam paths 1–3. Projecting their trajectories back, there will be a position where rays 1 and 2 cross for an ideal target, and a point of closest approach for a nonideal target. There will be a separate point of closest approach for rays 1 and 3. Constructive interference will occur if the backprojected rays pass sufficiently close to each other. For an ideal target, rays with different angles of incidence will cross in rotated midplanes but may still be close enough to each other in the object plane to interfere. Viewed alternatively, each angle of incidence will result in an interference pattern that appears to be formed within the target with a certain localization depth along the propagation direction; the patterns for different angles then add in intensity. This property of the system makes it unnecessary to illuminate the targets with collimated light and enhances the brightness of the images. It suffices to use a narrow-bandwidth extended source such as a low-pressure mercury-vapor lamp.

From Fig. 64.32, it is evident that the SIP is largely independent of the gas inside the target, whatever its pressure. This is because the interfering rays have a small angle and lateral
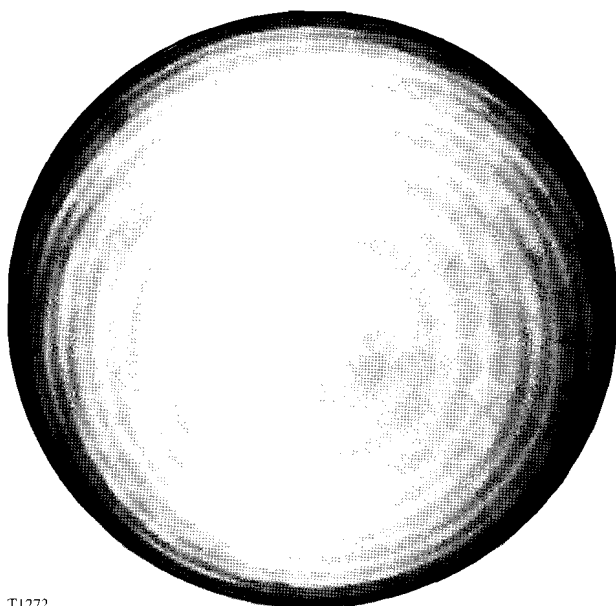
T1272

Figure 64.38
Example of an interference pattern formed from a poor-quality shell. Two SIP's are produced, as in Fig. 64.37, but they are not concentric.

displacement relative to each other; thus, they traverse almost the same optical path through the gas. This allows the target's wall thickness to be measured, after it is pressurized with fusion fuel, without accurate knowledge of the fill pressure. This is not possible with dual-beam interferometry since the optical path through the target is relative to an equivalent path in air. In this case, the difference between the refractive index of the fill gas and that of the surrounding air must be accounted for and subtracted from the total optical path length through the target to determine its wall thickness.

Fringe Visibility

Uniform shells possess a relatively high fringe visibility with respect to nonuniform shells since the reflected wave-fronts (beams 2 and 3) superpose both in space and phase, thereby interfering constructively to modify the amplitude of the transmitted wavefront (beam 1). Assume electric-field amplitude transmission coefficients T_1 and T_2 and a reflection coefficient R, respectively, at each interface. (T_1 and T_2 apply to rays passing from air to shell and from shell to air, respectively. Similar coefficients R_1 and R_2 could be defined, but they are equal in magnitude.) In practice, T_1, T_2, and R will depend on the angle of incidence at each interface, but the assumption of single values for T_1, T_2, and R will be good near the target center. For $n = 1.59$, $R = (n-1)/(n+1) = 0.228$. Then the amplitudes of transmitted waves 1–3 are given respectively by

$$A_1 = A_0 T_1^2 T_2^2,$$

$$A_2 = A_0 T_1^2 T_2^2 R^2, \tag{6}$$

$$A_3 = A_0 T_1^2 T_2^2 R^2.$$

For a perfectly symmetric shell, waves 2 and 3 interfere constructively to produce a wave with amplitude

$$A_2 + A_3 = 2A_0 T_1^2 T_2^2 R^2. \tag{7}$$

Interference between these two waves and the purely transmitted wave 1 gives amplitudes

$$A_1 \pm (A_2 + A_3) = A_0 T_1^2 T_2^2 (1 \pm 2R^2) \tag{8}$$

with ± indicating constructive (destructive) interference. The

fringe visibility is then

$$V \cong \frac{I_{max} - I_{min}}{I_{max} + I_{min}} \quad = \quad \frac{\left(1 + 2R^2\right)^2 - \left(1 - 2R^2\right)^2}{\left(1 + 2R^2\right)^2 + \left(1 - 2R^2\right)^2} \quad (9)$$

$$= \frac{4R^2}{1 + 4R^4} , \quad (10)$$

where I_{max} and I_{min} denote maximum and minimum intensities. Without waves 2 and 3 combining, Eq. (8) would be replaced by

$$A_1 \pm A_2 = A_0 T_1^2 T_2^2 \left(1 \pm R^2\right) \quad (11)$$

for interference between waves 1 and 2, with

$$V' = \frac{2R^2}{1 + R^4} . \quad (12)$$

Thus, the visibility is greater by about a factor of 2 when waves 2 and 3 constructively interfere. For example, for $n = 1.59$, $R = (n - 1)/(n + 1) = 0.228$, $V = 0.206$, and $V' = 0.104$.

Experimental Verification

The wall thicknesses of several glass shells were measured using dual-beam interferometry with an uncertainty of ±0.05 μm. Their outside diameters were also determined using a calibrated compound microscope to within ±3 μm. The refractive index of the glass shells was measured by fracturing shells from the same glass batch, immersing them in index-matching fluid, and varying the fluid temperature until the glass shards could not be differentiated from the fluid.[5] This method utilizes the temperature dependence of the refractive index of the index-matching fluid and results in a very sensitive refractive-index measurement with an uncertainty as low as ±0.0002. The shells were then imaged with the same compound microscope used to measure their outside diameter, but with a 10-nm-bandwidth interference filter centered on a 546-nm wavelength placed between its diffuser and condenser; this time the diameters of the SIP fringes were measured.

A comparison between the measured SIP fringe diameters and the calculated ones for a specific shell of thickness 2.89±0.05 μm is given in Table 64.III. Calculated fringe diameters are given for 2.89 μm and 2.93 μm. The latter thickness, well within the uncertainty of the thickness measurement, gives the better agreement between the measured and calculated SIP fringe diameters.

The SIP fringe diameters (when normalized to the shell diameter) are much less sensitive to small errors in the outside diameter than in the wall thickness because the universal curves of Fig. 64.34 depend primarily on the ratio r_i/R_{shell}. As noted above, the SIP is more sensitive to wall thickness variations than the dual-beam interferogram of the same target. In particular, the positions of the SIP innermost fringes provide information not so readily available from dual-beam interferometry because of the problem of establishing the piston, i.e., the absolute value of the optical path through the target center.

Table 64.III: A comparison between the calculated and measured SIP fringe diameters for a glass ($n = 1.4648 \pm 0.003$) shell with a 255 ± 3-μm outside diameter illuminated with 546-nm light with a 10-nm bandwidth. The measured wall thickness of 2.89 ± 0.05 μm was obtained using a Mach-Zehnder interference microscope. The SIP fringe diameters were measured with a calibrated eyepiece reticule while viewing the shell through a compound microscope. A wall thickness of 2.93 μm gave the best agreement between the calculated and measured SIP fringe diameters and is within the uncertainty of the wall thickness measurement. (The outermost predicted fringe was not observed in the measured SIP.)

Calculated fringe diameters (μm)		Measured fringe diameters (μm)
$t = 2.89$ μm	$t = 2.93$ μm	
94	110	112±5
160	168	167±3
202	210	206±3
238	242	

Conclusions

The SIP fringe technique is now routinely used to preselect targets based on their wall thickness and nonconcentricity prior to high-precision interferometric characterization. This technique requires only a compound microscope with a narrow-bandwidth interference filter or a stereo microscope and a diffuse mercury-vapor illumination source. The wall thickness is determined to within ± 0.5 μm by counting the number of fringes in the SIP, independent of the outside diameter, and the thickness uniformity is verified to an accuracy better than 0.05 μm. In addition, the wall thickness of gas-filled targets can be determined to the same accuracy without knowledge of the type of gas or its pressure.

REFERENCES

1. G. M. Halpern *et al.*, J. Appl. Phys. **48**, 1223 (1977).

2. R. Q. Gram, M. D. Wittman, C. Immesoete, H. Kim, R. S. Craxton, N. Sampat, S. Swales, G. Pien, J. M. Soures, and H. Kong, J. Vac. Sci. Technol. A **8**, 3319 (1990).

3. M. K. Prasad, K. G. Estabrook, J. A. Harte, R. S. Craxton, R. A. Bosch, Gar. E. Busch, and J. S. Kollin, Phys. Fluids B **4**, 1569 (1992).

4. Green Monochromatic Lamp, Edmund Scientific Co., 101 E. Gloucester Pike, Barrington, NJ 08007-1380.

5. R. P. Cargille Laboratories, Inc., Cargille Scientific, Inc., Cedar Grove, NJ 07009.

Femtosecond Study of the Electronic Structure in Semiconducting Y-Ba-Cu-O

We have carried out femtosecond pump-probe studies of the electronic structure of semiconducting $YBa_2Cu_3O_x$ (YBCO). By separating photoinduced bleaching and free-carrier absorption, we have measured the charge-transfer gap. The recovery after the photoexcitation follows a stretched exponential law with a temperature-independent dispersion factor and a temperature-dependent decay time. At probe energies below 1.9 eV, a drastic decrease in bleaching is observed as a consequence of induced free-carrier absorption within the O-$2p$ band, which leads us to the conclusion that the bandwidth of the O-$2p$ band is approximately 1.9 eV.

Femtosecond spectroscopy has been a powerful tool in probing the properties of high-temperature superconductors (HTS), including the quasiparticle dynamics,[1-3] coherent phonons,[4,5] the electron-phonon coupling constant,[6-8] and the position of the Fermi level.[9-13] In the normal state of oxygen-rich YBCO with $x > 6.8$, the Fermi smearing model has been widely applied in describing the transient optical response, especially the sign change of the differential reflectivity when the probe is tuned across the Fermi level.[9-13] However, there is no general agreement over the dependence of the signal sign on doping, pump intensity, and temperature.

Recent femtosecond studies on insulating cuprates have observed both photobleaching and induced absorption.[14] The initial subpicosecond decay of the bleaching was assigned to two-magnon emission; however, the origin of the induced absorption below 1.6 eV was not fully understood. It is well accepted that semiconducting YBCO ($x < 6.3$) is a Mott-Hubbard insulator with a charge-transfer (CT) gap between the Cu-$3d$ upper Hubbard band (UHB) and the O-$2p$ band. Several corresponding band diagrams have been proposed based on Raman,[15] photoconductivity,[16] and photoluminescence[17] studies. Moreover, transient photoconductivity investigation has shown a long lifetime (>10 ns) for photoexcited carriers in insulating YBCO.[18]

In the present study, we explore the mechanisms of the nonequilibrium optical response in oxygen-poor semiconducting YBCO. We observe a stretched exponential recovery of the bleaching signals. We find that photoinduced, free-carrier absorption occurs at probe energies smaller than the bandwidth of the O-$2p$ band. The interplay of free-carrier absorption and bleaching results in a significant enhancement of the recovery rate of the signal near the band edge. By investigating the relative contributions of the induced absorption and bleaching, we estimate that the bandwidth of the O-$2p$ band is approximately 1.9 eV.

Experiments

Our experiments were performed on 200-nm-thick epitaxial semiconducting YBCO films, which were deposited on MgO substrates using RF magnetron sputtering. Oxygen depletion was achieved by in-situ annealing of as-deposited films in 100 mTorr of Ar. Cryogenic testing of their electronic transport showed a behavior typical for a variable-length hopping.[19] The optical density was obtained using a Perkin-Elmer Lambda-9 spectrometer. The femtosecond response was investigated between room temperature and 12 K using a conventional pump-probe technique. Laser pulses of 120 fs in duration were generated by a colliding-pulse, mode-locked laser and further amplified by a copper vapor laser at an 8.5-kHz repetition rate. While the pump energy was fixed at 2 eV, variable probe energies were obtained from a white-light continuum. Pump and probe beams were cross polarized and focused on the 30-μm sample surface. With the pump energy of 10 nJ per pulse, the injected carrier density is estimated to be $\sim 10^{20}$ cm^{-3}. Lock-in and differential detection techniques were used to enhance the signal-to-noise ratio. Time-resolved transient changes in both reflection and transmission were measured simultaneously so that both the transient absorption ($\Delta\alpha$) and the unperturbed absorption coefficient (α_0) could be obtained by a numerical fitting that included Fabry-Perot interferences.[20] The low-temperature measurements were

performed in a continuous-He-flow optical cryostat using 2-eV pump and probe pulses.

Results and Discussion

Figure 64.39 shows the room-temperature linear absorption spectrum of an oxygen-depleted YBCO ($x \sim 6.0$) film. Two main absorption features near 1.78 and 2.8 eV are clearly resolved. These two peaks are related to the CT transition between the filled Cu-3d UHB and the empty O-2p band (in the hole picture).[15,16] In addition, a broad bandtail is observed below the fundamental absorption peak near 1.78 eV. Low-temperature photoconductivity studies have indicated that the lowest interband transition occurs at 1.5 eV.[17] Therefore, it can be concluded that all the probe energies (>1.65 eV) used in the present study are greater than the CT gap, and thus bleaching is expected as a result of band filling. Also shown in Fig. 64.39 are the values of α_0 (solid dots) obtained from the numerical fitting of the pump-probe data. The good agreement between α_0 from pump-probe experiments and the linear absorption curve demonstrates the effectiveness of the fitting program and gives additional confidence in our experimental results.
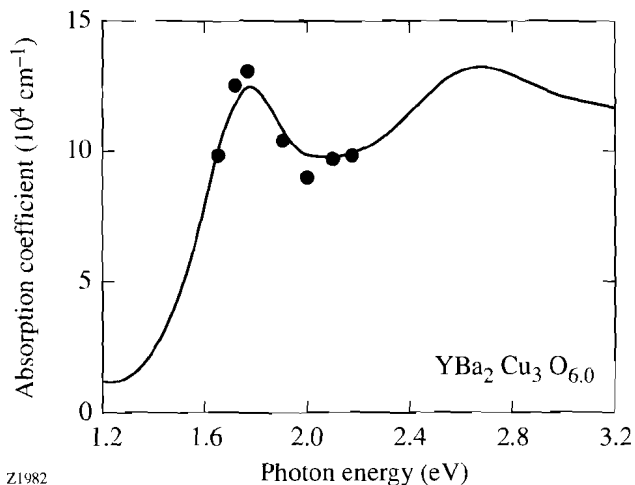

Figure 64.39

Absorption spectrum of semiconducting YBCO at room temperature. The solid dots are the values of linear absorption obtained from the pump-probe data.

Figure 64.40 displays the normalized transient absorption at probe energies from 1.65 eV (750 nm) to 2.1 eV (570 nm). As expected, bleaching ($\Delta\alpha < 0$) is observed at all wavelengths immediately after the excitation. The pulse-width-limited rise of the bleaching is due to the efficient redistribution of

photoexcited carriers by carrier-carrier (CC) scattering. As in the case of conventional semiconductors, such as GaAs,[21] CC scattering occurs on a sub-100-fs time scale when the injected density is higher than 10^{19} cm^{-3}. The redistributed carriers occupy the previously empty states and, hence, block the possible transitions across the CT gap.
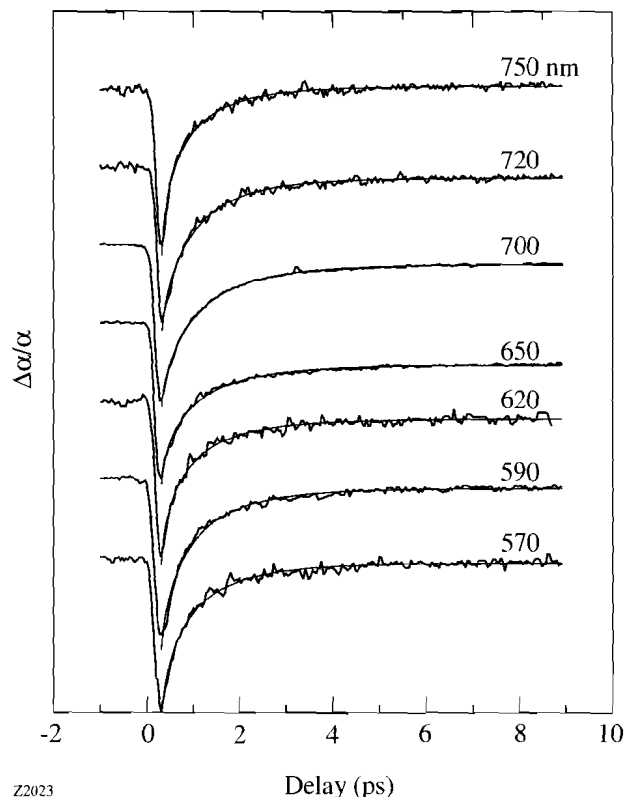
Figure 64.40

Time-resolved differential absorption ($\Delta\alpha/\alpha$) of semiconducting YBCO at several probe wavelengths. The data are normalized and shifted vertically for clarity. The smooth lines are the fits using a stretched exponential.

The excess energy of the excited carriers is then transferred to the lattice. Since the carrier lifetime (~10 ns) is much longer than our 10-ps sampling window, one would expect carrier accumulation near the band edge prior to recombination. As a consequence, for photon energies near the band edge, the recovery of bleaching should become a slow process. In some cases, the bleaching could even increase with time as the carriers slowly cool down to near room temperature. We observe instead that the recovery is slowest around 1.9 eV (650 nm), rather than near the band edge (1.65 eV or 750 nm). Close to the band edge, the bleaching disappears in a few picoseconds, and the signal becomes positive after 5 ps

(Fig. 64.40), indicating induced absorption. The appearance of induced absorption at 1.65 eV suggests that the excited carriers can be further excited.

The relaxation measured by the recovery of the bleaching follows a stretched exponential and not a simple exponential. The smooth solid lines in Fig. 64.40 are fitted by a normalized stretched exponential plus a constant term, i.e., $-\Delta\alpha/\alpha = \exp\left[-(t/\tau)^\beta\right] + C_1$. While the first term models the relaxation of hot carriers, C_1 represents the excess heat that escapes by the much slower process of heat diffusion (bolometric process). The fitting provides constant values for $\tau \approx 0.6$ ps and $\beta \approx 0.7$ over the whole spectral range at room temperature. The stretched-exponential decay indicates the coexistence of multiple processes that cannot be represented by a unique time constant.[22,23]

In Fig. 64.41, the transient absorption spectra from Fig. 64.40 are plotted for different time delays. It takes 300 fs to reach the maximum bleaching, consistent with the pulse-width-limited rise time and fast CC scattering. Spectrally, the maximum bleaching is at 1.9 eV, an energy at which there is no peak in the linear absorption. There is also no observable spectral shift of the 1.9-eV peak with time over a 10-ps window. The decay in Fig. 64.41 shows that the slowest recovery occurs near 1.9 eV instead of at the band edge. In fact, at the band edge (1.65 eV) there is even a small increase in
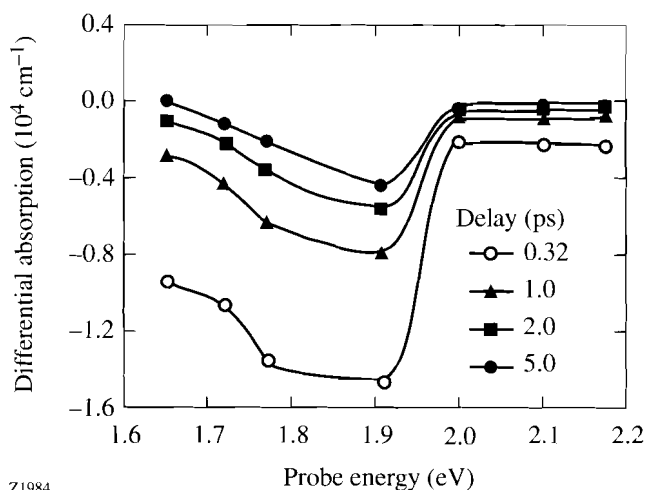
Figure 64.41
Differential absorption spectra at several delay times after the maximum bleaching.

absorption after 5 ps, which indicates that, in this case, induced absorption overcomes bleaching. Therefore, the increase of the recovery rate below 1.9 eV results from induced absorption that cancels the bleaching. From the injected density of about 10^{20} cm^{-3} and the magnitude of the induced absorption (about 300 cm^{-1}), we deduce a transition cross section of $\sim 3 \times 10^{-18}$ cm^2. Due to the partial cancellation of the induced absorption by the bleaching, the real transition cross section for free-carrier absorption could be larger than this. Nevertheless, the value of $\sim 3 \times 10^{-18}$ cm^2 is consistent with free-carrier absorption involving extended states and is much smaller than dipole-allowed absorption by carriers trapped in localized states. Therefore, the most likely bleaching cancellation process is free-carrier absorption inside the O-$2p$ band.

Free-carrier absorption inside the O-$2p$ band must depend strongly on the probe energy. At probe energies larger than the bandwidth of the O-$2p$ band, no intraband transition is possible and only bleaching exists. Below that threshold energy, however, induced absorption and bleaching coexist and compensate each other. The net result is an increase in the recovery rate of bleaching and eventually induced absorption. Consequently, the fact that the fastest absorption recovery occurs near 1.9 eV corresponds to the threshold for free-carrier absorption and should be related to the bandwidth of the O-$2p$ band. For smaller probe energies, the induced absorption becomes progressively stronger than bleaching because more occupied states are available for intraband transitions. As a result, the recovery rate of the differential signal increases drastically toward the lower energies (band edge) and starts to dominate at 1.65 eV (see Fig. 64.41).

Figure 64.42 shows the dependence of the time-resolved differential transmission $\Delta T/T$ on temperature. We note that the recovery of $\Delta T/T$ is faster at lower temperatures. As in Fig. 64.40, the relaxation process can be accurately fitted by a stretched exponential law (the smooth solid lines in Fig. 64.42). Figure 64.43 plots the time constant τ and the dispersion factor β used for the stretched exponential fitting in Fig. 64.42. Unlike in the case of trapping where $\beta = T/T_0$,[22,23] our value of β is independent of temperature. Simultaneously, τ shows a decrease with the temperature decrease, rather than an exponential increase. Therefore, our signals cannot be explained by a distribution of trapping states. The increased decay rate at low temperatures may be related to the emission of acoustic phonons.
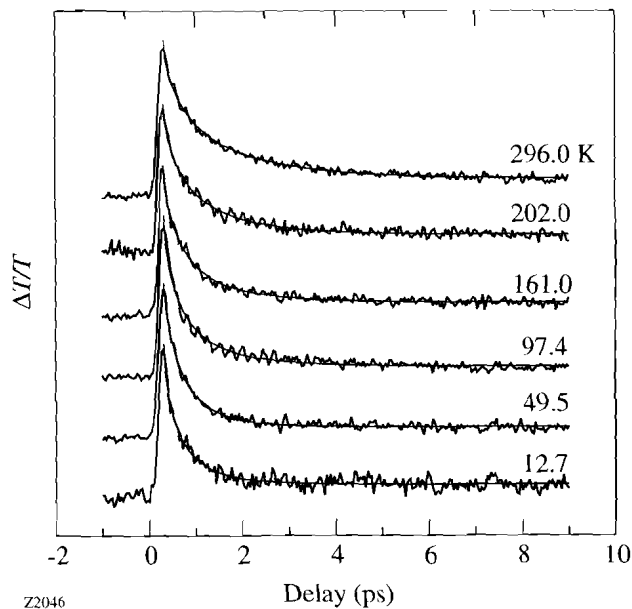
Z2046

Figure 64.42
Time-resolved differential transmission $(\Delta T/T)$ of semiconducting YBCO at different temperatures. As in Fig. 64.40, the fitting by a stretched exponential is shown as smooth lines.

Z2024

Figure 64.43
Stretched exponential parameters for transient transmission in Fig. 64.42 as a function of temperature. The solid lines are a guide to the eye.

Conclusions

We have measured the transient optical response of semiconducting YBCO by femtosecond spectroscopy. Using probe pulses of different wavelengths, we have measured the free-carrier absorption within the O-2p band and bleaching across the CT gap. The hot carrier dynamics is described precisely by a stretched-exponential law. The temperature-independent dispersion factor (β) excludes transitions involving the trapping states within the CT gap. For probe energies above 1.9 eV, only bleaching contributes to the transient signals. Below 1.9 eV, photoinduced absorption due to free-carrier absorption inside the O-2p band coexists with the bleaching and results in a drastic decrease in the recovery time. Hence, the peak position of the bleaching at 1.9 eV is considered to be a measure of the bandwidth for the O-2p band.

ACKNOWLEDGMENT

REFERENCES

1. S. G. Han et al., Phys. Rev. Lett. **65**, 2708 (1990).

2. S. G. Han et al., Phys. Rev. Lett. **67**, 1053 (1991).

3. G. L. Eesley et al., Phys. Rev. Lett. **65**, 3445 (1990).

4. J. M. Chwalek et al., Appl. Phys. Lett. **57**, 1696 (1990).

5. W. Albrecht, T. Kruse, and H. Kurz, Phys. Rev. Lett. **69**, 1451 (1992).

6. S. V. Chekalin et al., Phys. Rev. Lett. **67**, 3860 (1991).

7. S. D. Brorson et al., Phys. Rev. Lett. **64**, 2172 (1990).

8. A. L. Dobryakov et al., Opt. Spectrosc. **76**, 871 (1994).

9. A. S. Kazeroonian et al., Solid State Commun. **7**, 95 (1991).

10. D. H. Reitze et al., Phys. Rev. B **46**, 14,309 (1992).

11. T. Gong, L. X. Zheng, W. Xiong, W. Kula, Y. Kostoulas, R. Sobolewski, and P. M. Fauchet, Phys. Rev. B **47**, 14,495 (1993).

12. W. Albrecht et al., Appl. Phys. A, Solids Surf. **A56**, 463 (1993).

13. L. Shi, T. Gong, W. Xiong, X. Weng, Y. Kostoulas, R. Sobolewski, and P. M. Fauchet, Appl. Phys. Lett. **64**, 1150 (1994).

14. K. Matsuda *et al.*, Phys. Rev. B **50**, 4097 (1994).

15. E. T. Heyen, J. Kircher, and M. Cardona, Phys. Rev. B **45**, 3037 (1992).

16. G. Yu *et al.*, Phys. Rev. B **48**, 7545 (1993).

17. V. N. Denisov *et al.*, Phys. Rev. B **48**, 16,714 (1993).

18. G. Yu *et al.*, Solid State Commun. **72**, 345 (1989).

19. R. Sobolewski, W. Xiong, W. Kula, and J. R. Gavaler, Appl. Phys. Lett. **64**, 643 (1994).

20. M. Born and E. Wolf, ed. *Principles of Optics*, 6th ed. (Pergamon Press, Oxford, 1980), p. 630.

21. T. Gong, P. M. Fauchet, J. F. Young, and P. J. Kelly, Phys. Rev. B **44**, 6542 (1991).

22. H. Scher, M. F. Shlesinger, and J. T. Bendler, Phys. Today, 26 (1991).

23. R. A. Street, in *Hydrogenated Amorphous Silicon* (Cambridge University Press, Cambridge. 1991), p. 203.

Laser Facility Report

This report summarizes activities on the OMEGA laser system from the commissioning shot series of the Key Decision 4 (KD4) campaign to the end of FY95. The KD4 series ended with the final system acceptance tests on 2 May 1995, which demonstrated that the system met and exceeded its performance goals. These results were reported in the previous issue of the LLE Review.[1] Following this campaign, the facility priorities during the third quarter of FY95 shifted to characterization and optimization of the laser and to diagnostic deployment on the target chamber, tasks that supported the experimental campaigns planned for the fourth quarter. Laser characterization included campaigns to collect detailed energy transport data in the OMEGA beamlines, while, in the target bay, many diagnostic systems were activated and the first 10-in.-manipulator (TIM) re-entrant diagnostic shuttle was installed. In addition, a facility improvement program was executed to address many issues that came up during the KD4 campaign.

The fourth quarter of FY95 was the first full quarter of operations on the upgraded OMEGA laser. The first implosion campaign (PP2) and flat-target campaign (S1) were successfully carried out. Results from the implosion campaign are reported in the first article of this issue. The laser system underwent significant improvements, with progress made in particular on the beam-timing, on-target pointing, and focusing systems. Beam-to-beam arrival time differences were measured with photodiodes and an oscilloscope, and all beams were adjusted to match a reference beam to <30 ps. The next-generation beam-timing instrument was tested and will be deployed during the next quarter to reduce beam-timing variations to less than 5 ps. Each target-shot day, pointing targets

were shot with 60 beams to measure beam locations by comparing x-ray pinhole-camera images with calculated beam positions.[1] These shots were used to determine which beams needed to be realigned with the UV alignment system. A total of 35 of these pointing shots were taken. In addition, a number of pointing shots were taken for flat targets irradiated during the S1 campaign and also for spherical targets not located at the center of the chamber. Typical pointing results indicated that the rms deviation from the best calculated position was under 20 μm. Two focus scans were executed this quarter to characterize the UV focus performance. The final focus parameters for each beam were determined to an accuracy of ±100 μm, with the results of this study to be published next quarter.

Experimental campaigns this quarter resulted in a total of 150 target shots. This is consistent with plans to deliver 1000 target shots each year. In addition to the active shot campaigns, much work has been completed to prepare for the propagation of SSD laser pulses, separate backlighter sources, and timing-fiducial lasers. The SSD system and the backlighter source are scheduled for activation in the first quarter of FY96.

The shot summary for OMEGA this quarter is as follows:

Driver	187
Beamline	234
Target	150
Total	571

REFERENCES

1. Laboratory for Laser Energetics LLE Review **63**, NTIS document No. DOE/SF/19460-91, 1995 (unpublished), p. 99.

NLUF News

Proposals for FY95

Eight proposals were submitted for consideration for FY95, as summarized in Table 64.IV. Two of them (186 and 188) are from principal investigators who submitted proposals for the first time. The proposals listed in Table 64.IV include three for x-ray spectroscopy measurements and one each for calibration of nuclear detectors, x-ray microscopy of ICF targets, high-resolution imaging, polymer shell characterization, and characterization of the critical surface.

These proposals were considered on 7 March 1995 by the voting members of the NLUF Steering Committee, listed in Table 64.V. The committee members include three from national laboratories, two from universities, and one from industry.

The approved FY95 proposals are listed in Table 64.VI, in order of technical merit as determined by the voting members of the Steering Committee. It is expected that the approved experiments will have OMEGA system time scheduled during calendar year 1996.

Table 64.IV: Proposals submitted for FY95.

Proposal Number	Principal Investigator	Institution	Title
186	Stephen Padalino	State University of New York at Geneseo	Neutron Calibration Studies for MEDUSA
187	Hans R. Griem	University of Maryland	Spectroscopic Diagnostics on High-Density, Strongly Coupled ICF Plasmas
188	Qichang Su	Illinois State University	Krypton Spectroscopy Diagnostics of High-Temperature Implosions
189	Ping-chin Cheng	State University of New York at Buffalo	Development of High-Resolution X-Ray Microtomographic System for Characterizing ICF Targets for the OMEGA Upgrade Experiments
190	John F. Seely	Naval Research Laboratory	Monochromatic Two-Dimensional Imaging of Laser Targets
191	Arnold Honig	Syracuse University	New Techniques Applied to Cryogenic Polymer Shells: Emissivity and Accommodation Coefficients, Electron Spin Resonance for Temperature Determination and Levitation, and Nuclear Magnetic Resonance for Composition and Other Diagnostics of Deuterated Plasma Coatings
192	Katsuhiro Mizuno	University of California, Davis	The Ion Acoustic Decay Instability in the OMEGA Upgrade Laser Plasma—Applications to a Critical Surface Diagnostic, and Instability at Quarter Critical Density
193	Charles F. Hooper, Jr.	University of Florida	Time-Resolved Plasma Spectroscopy of Imploded Gas-Filled Microballoons: The Next Generation

The first user experiment on the upgraded OMEGA laser system is the University of Maryland proposal (Number 187), which is expected to begin in January 1996. H. Griem and R. Elton from the University of Maryland have visited LLE to discuss this experiment. They will be mounting an XUV spectrometer on the OMEGA target chamber and are at present designing the mechanical mounts. LLE personnel are assisting them with preparations for this experiment.

Proposals for FY96

Nine proposals, summarized in Table 64.VII, have been submitted for consideration for FY96. The proposals include four for x-ray spectroscopy experiments and one each for cryogenic target characterization, nuclear calibration, hohlraum diagnostic development, high-resolution low-energy x-ray imaging of laser irradiation imprinting, and optical imaging of the critical surface. These proposals are presently being reviewed by the Steering Committee.

Table 64.V: Voting members of the NLUF Steering Committee.

Dr. John Apruzese	Naval Research Laboratory
Dr. Michael J. Boyle	Bondtronix, Inc.
Prof. Chandrashekhar J. Joshi	University of California at Los Angeles
Dr. Joseph D. Kilkenny	Lawrence Livermore National Laboratory
Dr. Richard D. Petrasso	Massachusetts Institute of Technology
Dr. Jeffrey P. Quintenz	Sandia National Laboratory

Table 64.VI: Approved FY95 NLUF proposals.

Proposal Number	Principal Investigator	Institution
192	Katsuhiro Mizuno	University of California, Davis
193	Charles F. Hooper, Jr.	University of Florida
188	Qichang Su	Illinois State University
191	Arnold Honig	Syracuse University
187	Hans R. Griem	University of Maryland

Table 64.VII: Proposals submitted for FY96.

Proposal Number	Principal Investigator	Institution	Title
194	Hans R. Griem	University of Maryland	Electric Field Measurements from Satellites to Forbidden Line Ratios in an OMEGA Upgrade Laser-Produced Plasma
195	Arnold Honig	Syracuse University	Optical Imaging, Electron Spin Resonance, and Nuclear Magnetic Resonance Applied to Cryogenic Polymer ICF Targets for Low-Temperature Emissivity and Accommodation Coefficient, Levitation, and Quantitative Analysis of Fuel and Target Shell Material
196	Stephen Padalino	State University of New York at Geneseo	Calibration of Neutron Diagnostics for OMEGA
197	Joseph J. MacFarlane	University of Wisconsin, Madison	Development of Soft X-Ray Tracer Diagnostics for Hohlraum Experiments
198	Eugene Clothgiaux	Auburn University	Implementation of Novel X-Ray Polarization Diagnostics for OMEGA Upgrade at the National Laser Users Facility (NLUF)
199	John F. Seely	Naval Research Laboratory	High-Resolution Imaging of Early-Time Imprinting Using Normal-Incidence Multilayer Mirrors
200	Qichang Su	Illinois State University	Diagnosis of Core-Shell Mixing with Absorption and Emission Spectra of a Doped Layer
201	Katsuhiro Mizuno	University of California, Davis	The Ion Acoustic Decay Instability in the OMEGA Upgrade Laser Plasma—Applications to Optical Micrograph Image Diagnostic, and Instability at the Quarter Critical Density
202	Charles F. Hooper, Jr.	University of Florida	Time-Resolved Plasma Spectroscopy of Imploded Gas-Filled Microballoons: Continuum Lowering and Pusher Dynamics

Publications and Conference Presentations

Publications

M. S. Adams, M. V. Fedorov, V. P. Krainov, and D. D. Meyerhofer, "Comparison of Quasiclassical and Exact Dipole Moments for Bound-Free Transitions in Hydrogen," Phys. Rev. A **52**, 125 (1995).

T. R. Boehly, R. S. Craxton, T. H. Hinterman, P. A. Jaanimagi, J. H. Kelly, T. J. Kessler, R. L. Kremens, S. A. Kumpan, S. A. Letzring, R. L. McCrory, S. F. B. Morse, W. Seka, S. Skupsky, J. M. Soures, and C. P. Verdon, "The Upgrade to the OMEGA Laser System," Fusion Technol. **26**, 722 (1994); also in the *Proceedings of the IAEA Technical Committee Meeting on Drivers for Inertial Confinement Fusion*, Paris, France 14–18 November 1994, edited by J. Coutant (IAEA, 1995), pp. 79–86.

M. J. Cumbo, D. Fairhurst, S. D. Jacobs, and B. E. Puchebner, "Slurry Particle Size Evolution during the Polishing of Optical Glass," Appl. Opt. **34**, 3743 (1995).

D. Gupta, W. R. Donaldson, and A. M. Kadin, "Rapid Flux Motion and Critical State Dynamics in a Superconducting Disk," J. Appl. Phys. **78**, 372 (1995).

F. A. Hegmann, D. Jacobs-Perkins, S. H. Moffat, C.-C. Wang, R. A. Hughes, M. Currie, P. M. Fauchet, T. Y. Hsiang, J. S. Preston, and R. Sobolewski, "Electro-Optic Sampling of 1.5-ps Photoresponse Signal from $YBa_2Cu_3O_{7-\delta}$ Thin Films," Appl. Phys. Lett. **67**, 285 (1995).

S. D. Jacobs, D. Golini, Y. Hsu, B. E. Puchebner, D. Strafford, W. I. Kordonsky, I. V. Prokhorov, E. Fess, D. Pietrowski, and V. W. Kordonsky, "Magnetorheological Finishing: A Deterministic Process for Optics Manufacturing," in the *International Conference on Optical Fabrication and Testing*, edited by Toshio Kasai (SPIE, Bellingham, WA, 1995), Vol. 2576, pp. 372–382 (invited).

J. C. Mastrangelo, H. Shi, S.-H. Chen, and T. N. Blanton, "Design, Synthesis, and Stability of Organic Glasses for Advanced Optical Applications," in *Polymer Preprints* (American Chemical Society, August 1995), Vol. 36(2), pp. 43–44.

R. L. McCrory, "Progress Toward Ignition with Direct-Drive," in *Great Systems in Science and Technology*, edited by J. Horowitz and J. L. Lions (Mason Publishing, Paris, France, 1993), pp. 555–569.

C. J. McKinstrie and E. A. Startsev, "Wave Propagation in a Drifting Plasma," Phys. Plasmas **5**, 3234 (1995).

D. Shvarts, U. Alon, D. Ofer, R. L. McCrory, and C. P. Verdon, "Nonlinear Evolution of Multimode Rayleigh-Taylor Instability in Two and Three Dimensions," Phys. Plasmas **2**, 2465 (1995).

C.-C. Wang, M. Currie, R. Sobolewski, and T. Y. Hsiang, "Subpicosecond Electrical Pulse Generation by Edge Illumination of Silicon and Indium Phosphide Photoconductive Switches," Appl. Phys. Lett. **67**, 79 (1995).

M. Yu, C. J. McKinstrie, and G. P. Agrawal, "Modulational Instabilities in Dispersion-Flattened Fibers," Phys. Rev. E **52**, 1072 (1995).

M. Yu, G. P. Agrawal, and C. J. McKinstrie, "Effect of Residual Dispersion in the Phase-Conjugation Fiber on Dispersion Compensation in Optical Communication Systems," IEEE Photonics Technol. Lett. **7**, 932 (1995).

Forthcoming Publications

R. Adam, W. Kula, R. Sobolewski, J. M. Murduck, and C. Pettiette-Hall, "Laser-Induced Modification of Transport Properties of Y-Ba-Cu-O Step-Edge Weak Links," to be published in Applied Physics Letters.

R. Betti, V. N. Goncharov, R. L. McCrory, and C. P. Verdon, "Self-Consistent Cutoff Wave Number of the Ablative Rayleigh-Taylor Instability," to be published in Physics of Plasmas.

X. D. Cao, J. Peatross, and D. D. Meyerhofer, "Self-Defocusing of Intense Laser Pulses in a Low-Pressure Gas Target," to be published in Physical Review A.

X. D. Cao and D. D. Meyerhofer, "Optimization of Pulse Shaping Using Nonlinear Polarization Rotation," to be published in Optics Communication.

S.-H. Chen, J. C. Mastrangelo, and H. Shi, "Novel Low Molar Mass, Glass-Forming Liquid Crystals: Molecular Design, Synthesis, and Morphological Stability," to be published in the Proceedings of Polymers for Advanced Optical Applications.

S.-H. Chen, J. C. Mastrangelo, H. Shi, A. Bashir-Hashemi, J. Li, and N. Gelber, "Novel Glass-Forming Materials Based on Adamantane with Pendant Cholesteryl, Disperse Red 1, and Nematogenic Groups," to be published in Macromolecules.

C. T. Cotton, "Design Considerations for the OMEGA Upgrade Final Focus Lens," to be published in the Proceedings of SPIE's 1995 International Symposium on Optical Science, Engineering, and Instrumentation, San Diego, CA.

C. T. Cotton, "The Design of an All-Spherical, Three-Mirror, Off-Axis Telescope Objective," to be published in the OSA Proceedings of the International Optical Design Conference '94, Rochester, NY.

P. M. Fauchet, L. Tsybeskov, C. Peng, S. P. Duttagupta, J. von Behren, Y. Kostoulas, J. V. Vandyshev, and K. D. Hirshman, "Light-Emitting Porous Silicon: Materials Science, Properties, and Device Applications," to be published in the IEEE Journal of Selected Topics in Quantum Electronics.

D. Fried, R. E. Glena, J. D. B. Featherstone, and W. Seka, "Permanent and Transient Changes in the Reflectance of CO_2 Laser-Irradiated Dental Hard Tissues at $\lambda = 9.3$, 9.6, 10.3, and 10.6 μm and at Fluences between 1–20 J/cm^2," to be published in Lasers in Surgery and Medicine.

R. E. Giacone, C. J. McKinstrie, and R. Betti, "Angular Dependence of Stimulated Brillouin Scattering in Homogeneous Plasma," to be published in Physics of Plasmas.

V. N. Goncharov, R. Betti, R. L. McCrory, P. Sorotokin, and C. P. Verdon, "Self-Consistent Stability Analysis of Ablation Front for Inertial Confinement Fusion," to be published in Physics of Plasmas.

V. N. Goncharov and R. Betti, "Growth Rate of the Ablative Rayleigh-Taylor Instability for Indirect-Drive ICF," to be published in Physics of Plasmas.

K. Green, W. R. Donaldson, R. Sobolewski, M. D. Skeldon, W. Seka, A. Okishev, and S. A. Letzring, "Transient Microwave Bandwidth Measurements of Illuminated Silicon Switches for Optical Pulse-Shape Control of Laser-Fusion Drivers," to be published in the SPIE Proceedings of the 1st Annual International Conference on Solid-State Lasers for Application to Inertial Confinement Fusion (ICF), Monterey, CA, 30 May–2 June 1995.

J. Hecht, D. Ofer, U. Alon, D. Shvarts, S. A. Orszag, and R. L. McCrory, "Three-Dimensional Simulations and Analysis of the Nonlinear Stage of the Rayleigh-Taylor Instability," to be published in Laser and Particle Beams.

J. H. Kelly, T. R. Boehly, J. M. Soures, D. L. Brown, R. Boni, R. S. Craxton, R. L. Keck, T. J. Kessler, R. Kremens, S. A. Kumpan, S. A. Letzring, S. J. Loucks, R. L. McCrory, S. F. B. Morse, W. Seka, S. Skupsky, and C. P. Verdon, "The Activation of the Upgraded OMEGA Laser at the University of Rochester," to be published in the SPIE Proceedings of the 15th International Conference on Coherent and Nonlinear Optics, St. Petersburg, Russia, June 1995 and the SPIE Proceedings of the 1st Annual International Conference on Solid-State Lasers for Application to Inertial Confinement Fusion (ICF), Monterey, CA, 30 May–2 June 1995.

O. A. Konoplev and D. D. Meyerhofer, "Dynamic Range Limitations in High-Contrast, Noncollinear Autocorrelators,"

to be published in Generation, Amplification, and Measurement of Ultrashort Laser Pulses III.

E. M. Korenic, S. D. Jacobs, S. M. Faris, and L. Li, "Colorimetry of Fractured Cholesteric Liquid Crystal Polymers" to be published in the Third Color Imaging Conference Proceedings.

Y. Kostoulas, K. B. Ucer, L. Waxer, G. W. Wicks, I. A. Walmsley, and P. M. Fauchet, "Ultrafast Carrier Lifetime in Low-Temperature-Grown GaAs, InP, and InGaP," to be published in the Proceedings of LEOS '94 7th Annual Meeting, Boston, MA, 31 October–3 November 1994.

T. Kotseroglou, C. Bamber, S. Boege, U. Haug, A. C. Melissinos, D. D. Meyerhofer, W. Ragg, C. Bula, K. T. McDonald, E. Prebys, D. L. Burke, P. Chen, R. C. Field, G. Horton-Smith, A. C. Odian, J. C. Spencer, D. Walz, S. Berridge, W. Bugg, K. Shmakov, and A. Weidemann, "Studies of Nonlinear QED with an Ultra-Intense Laser," to be published in Generation, Amplification, and Measurement of Ultrashort Laser Pulses III.

W. Kula, R. Adam, and R. Sobolewski, "Y-Ba-Cu-O Thin-Film Structures with a Nonuniform In-Depth Oxygen Concentration Profile," to be published in the Institute of Physics Conference Series.

W. Lang, W. Göb, W. Kula, and R. Sobolewski, "Anisotropic Magnetoresistance in the Normal State of Oxygen-Deficient $YBa_2Cu_3O_{7-\delta}$ Thin Films Induced by Superconducting Fluctuations," to be published in Zeitschrift Für Physik B.

Y. Lin, T. J. Kessler, and G. N. Lawrence, "Design of Continuous Surface-Relief Phase Plates by Simulated Annealing to Achieve Control of Focal Plane Irradiance," to be published in Optics Letters.

R. S. Marjoribanks, F. W. Budnik, H. Chen, and D. D. Meyerhofer, "Plasma Electron Temperature in Picosecond Laser Plasmas from Quasi-Steady Ratio of Isoelectronic Lines," to be published in the Journal of the Optical Society of America B.

K. L. Marshall, S. D. Jacobs, and J. E. Miller, "Midinfrared Modulation through the Use of Field-Induced Scattering in Ferroelectric Liquid Crystals," to be published in Applied Optics.

J. C. Mastrangelo, T. N. Blanton, and S.-H. Chen, "Morphology and Its Stability of Cyclohexane and Biocyclooctene

Rings Containing Pendant Disperse Red 1," to be published in Chemistry of Materials.

R. L. McCrory, J. M. Soures, C. P. Verdon, T. R. Boehly, D. K. Bradley, R. S. Craxton, J. A. Delettrez, R. Epstein, P. A. Jaanimagi, S. D. Jacobs, R. L. Keck, J. H. Kelly, T. J. Kessler, H. Kim, J. P. Knauer, R. L. Kremens, S. A. Kumpan, S. A. Letzring, F. J. Marshall, P. J. McKenty, S. F. B. Morse, A. Okishev, W. Seka, R. W. Short, M. D. Skeldon, S. Skupsky, M. Tracy, and B. Yaakobi, "Direct-Drive Laser Fusion Experimental Program at the University of Rochester Laboratory for Laser Energetics," to be published in the Proceedings of the Conference on Plasma Physics and Controlled Nuclear Fusion Research, Madrid, Spain, September 1994.

R. L. McCrory, J. M. Soures, C. P. Verdon, T. R. Boehly, D. K. Bradley, R. S. Craxton, J. A. Delettrez, R. Epstein, P. A. Jaanimagi, S. D. Jacobs, R. L. Keck, J. H. Kelly, T. J. Kessler, H. Kim, J. P. Knauer, R. L. Kremens, S. A. Kumpan, S. A. Letzring, F. J. Marshall, P. W. McKenty, S. F. B. Morse, A. Okishev, W. Seka, R. W. Short, M. D. Skeldon, S. Skupsky, M. Tracy, and B. Yaakobi, "Experiments on OMEGA to Validate High-Gain, Direct-Drive Performance on the National Ignition Facility," to be published in the Proceedings of the 12th International Conference on Laser Interaction and Related Plasma Phenomena, Osaka, Japan, April 1995.

R. L. McCrory, J. M. Soures, C. P. Verdon, A. Babushkin, T. R. Boehly, D. K. Bradley, R. S. Craxton, J. A. Delettrez, R. Epstein, P. A. Jaanimagi, S. D. Jacobs, R. L. Keck, J. H. Kelly, T. J. Kessler, H. Kim, J. P. Knauer, R. L. Kremens, S. A. Letzring, S. J. Loucks, F. J. Marshall, P. W. McKenty, S. F. B. Morse, A. Okishev, W. Seka, R. W. Short, M. D. Skeldon, S. Skupsky, and B. Yaakobi, "OMEGA Upgrade Laser System," to be published in the SPIE Proceedings of the 1st Annual International Conference on Solid-State Lasers for Application to Inertial Confinement Fusion (ICF), Monterey, CA, 30 May–1 June 1995.

D. D. Meyerhofer, J. P. Knauer, S. J. McNaught, and C. I. Moore, "Observation of Relativistic Mass Shift Effects during High-Intensity Laser-Electron Interactions," to be published in the Journal of the Optical Society of America B.

A. Okishev, M. D. Skeldon, S. A. Letzring, W. R. Donaldson, A. Babushkin, and W. Seka, "The Pulse-Shaping System for the 60-Beam, 30-kJ (UV) OMEGA Laser," to be published in the Proceedings of Laser Optics '95 Conference, St. Petersburg, Russia, 27 June–1 July 1995.

S. Papernov and A. W. Schmid, "A Comparison of Laser-Induced Damage Morphology in Three Model Thin-Film Systems: HfO_2, Y_2O_3, and Ta_2O_5," to be published in the Proceedings of the XXVI Annual Symposium on Optical Materials for High Power Lasers, Boulder, CO, 24–26 October 1994.

J. Peatross and D. D. Meyerhofer, "Intensity-Dependent Atomic-Phase Effects in High-Order Harmonic Generation," to be published in Physical Review A.

J. Z. Roach, A. Ninkov, S. W. Swales, and T. Morris, "Design and Evaluation of a Screen CCD Imaging System," to be published in Optical Engineering.

H. Shi and S.-H. Chen, "Dynamic Mechanical Properties of Cyclohexane-Based Glass-Forming Liquid Crystals and a Linear Side-Chain Polymer Analogue," to be published in Liquid Crystals.

H. Shi and S.-H. Chen, "Effects of Stereochemistry, Mesogenic Core, and Space Length on Crystallization from Nematic and Isotropic Melts of Cyclohexane-Based, Glass-Forming Liquid Crystals," to be published in Liquid Crystals.

H. Shi and S.-H. Chen, "Novel Glass-Forming Liquid Crystals. III. Helical Sense and Twisting Power in Chiral Nematic Systems," to be published in Liquid Crystals.

A. Simon, "Parametric Excitation of Bernstein Modes in Laser-Produced Plasma," to be published in Physics of Plasmas.

A. Simon, "Comparison Between SBS Theories and Experiment," to be published in Plasma Physics and Technology.

M. D. Skeldon, A. Okishev, A. Babushkin, and W. Seka, "Transient Stimulated Brillouin Scattering Pulse Compression for Photoconductive Switch Activation," to be published in the Proceedings of Solid-State Lasers for Application to Inertial Confinement Fusion (ICF), Monterey, CA, 30 May–2 June 1995.

C. J. Twomey, T. N. Blanton, K. L. Marshall, S.-H. Chen, and S. D. Jacobs, "Some Dynamic Features of the Preparation of Liquid Crystalline Elastomers," to be published in Liquid Crystals.

C. P. Verdon and R. L. McCrory, "Direct-Drive Capsule Physics," to be published in the Proceedings of ECLIM '94, Oxford, England, September 1994.

C.-C. Wang, M. Currie, D. Jacobs-Perkins, R. Sobolewski, T. Y. Hsiang, and M. J. Feldman, "Electro-Optic Measurements of Single-Flux Quantum Pulses," to be published in the Institute of Physics Conference Series.

M. D. Wittman, R. Q. Gram, H. Kim, C. K. Immesoete, S. G. Noyes, and S. Scarantino, "Increased Retention Time for Hydrogen and Other Gases by Polymer Shells Using Optically Transparent Aluminum Layers," to be published in the Journal of Vacuum Science and Technology.

W. Xiong, Y. Kostoulas, X. Weng, P. M. Fauchet, and R. Sobolewski, "Femtosecond Study of the Electronic Structure in Semiconducting Y-Ba-Cu-O," to be published in Physical Review B.

B. Yaakobi, D. Shvarts, R. Epstein, and Q. Qu, "X-Ray Backlighting Imaging of Mixed Imploded Targets," to be published in the Journal of Applied Physics.

B. Yaakobi, R. Epstein, C. F. Hooper, Jr., D. A. Haynes, Jr., and Q. Su, "Diagnosis of High-Temperature Implosions Using Low- and High-Opacity Krypton Lines" to be published in the Journal of X-Ray Science and Technology.

M. Yu and C. J. McKinstrie, "Impulse Response of a Nonlinear Dispersive Wave," to be published in Physical Review E.

X. Zhou, S. Alexandrou, and T. Y. Hsiang, "Monte Carlo Investigation of the Intrinsic Mechanism of Subpicosecond Pulse Generation by Nonuniform Illumination," to be published in Applied Physics Letters.

J. D. Zuegel and W. Seka, "Direct Measurements of Lower-Level Lifetime in Nd:YLF," to be published in the Bulletin of the American Physical Society.

J. D. Zuegel and W. Seka, "Direct Measurement of $^4I_{11/2}$ Terminal-Level Lifetime in Nd:YLF," to be published in the IEEE Journal of Quantum Electronics.

Conference Presentations

The following presentations were made at the European Conference on Applied Superconductivity, Edinburgh, Scotland, 3–6 July 1995:

W. Kula, R. Adam, and R. Sobolewski, "Y-Ba-Cu-O Thin-Film Structures with a Nonuniform In-Depth Oxygen Concentration Profile."

C.-C. Wang, M. Currie, D. Jacobs-Perkins, R. Sobolewski, T. Y. Hsiang, and M. J Feldman, "Electro-Optic Measurements of Single-Flux Quantum Pulses."

The following presentations were made at SPIE's International Symposium on Optical Science, Engineering, and Instrumentation, San Diego, CA, 9–14 July 1995:

C. T. Cotton, "Design Considerations for the OMEGA Upgrade Final Focus Lens."

P. A. Jaanimagi and A. Mens, "Photoelectron Throughput in Streak Tubes."

B. E. Puchebner and S. D. Jacobs, "Development of New Bound Abrasive Polishers for Final Finishing of Optical Glasses."

T. Y. Hsiang, S. Alexandrou, R. Sobolewski, and C.-C. Wang, "Terahertz Dispersion of Coplanar Waveguides and Waveguide Bends," Progress in Electromagnetics Research Symposium, Seattle, WA, 24–28 July 1995 (invited).

J. C. Mastrangelo, H. Shi, S.-H. Chen, and T. N. Blanton, "Design, Synthesis, and Stability of Organic Glasses for Advanced Optical Applications," American Chemical Society National Meeting, Chicago, IL, 20–24 August 1995.

The following presentations were made at the OSA Annual Meeting, Portland, Oregon, 10–15 September 1995:

S. D. Jacobs, "Deterministic Magnetorheological Finishing of Spheres and Aspheres" (invited).

A. Schmid, T. Kessler, K. Marshall, and J. Armstrong, "Organic Thin Films on the 30-kJ OMEGA Glass Laser System Organic Thin Films."

D. J. Smith, "Optical Coating Technology for the Upgraded OMEGA Laser" (invited).

H. Kim, S. J. Pan, and P. C. Cheng, "X-Ray Microtomography for Characterizing Inertial Confinement Fusion Spherical Capsules," 13th International Vacuum Congress, 9th International Conference on Solid Surfaces, Yokohama, Japan, 25–29 September 1995.